

UCLA

UCLA Electronic Theses and Dissertations

Title

Design and Synthesis of a Photoswitchable Gated Hemicarcerand and Computational Investigations of Stereoselective Organic Reactions

Permalink

<https://escholarship.org/uc/item/9wc0479n>

Author

Wang, Hao

Publication Date

2013

Peer reviewed|Thesis/dissertation

UNIVERSITY OF CALIFORNIA

Los Angeles

Design and Synthesis of a Photoswitchable Gated Hemiacarcerand and
Computational Investigations of Stereoselective Organic Reactions

A dissertation submitted in partial satisfaction of the
requirements for the degree Doctor of Philosophy
in Chemistry

by

Hao Wang

2013

ABSTRACT OF THE DISSERTATION

Design and Synthesis of a Photoswitchable Gated Hemicarcerand and
Computational Investigations of Stereoselective Organic Reactions

by

Hao Wang

Doctor of Philosophy in Chemistry

University of California, Los Angeles, 2013

Professor Kendall N. Houk, Chair

The general concept of developing gateable host-guest systems is a powerful one with many potential applications such as drug delivery and sensing. In this work, we designed and synthesized a reversible photoswitchable hemicarcerand. This hemicarcerand has an anthracene unit as the photoactive gating element and the reversible opening and closing of the “gate” of the host is well controlled photochemically. Various spectroscopic methods such as ^1H NMR and fluorescence demonstrate that, hemicarcerand host-guest complexes are stable to decomplexation at ambient temperatures in the photodimer structure, while release of guests such as 1,4-dimethoxybenzene is achieved by opening the gate by photochemically generating the anthracene monomers.

The second part of this dissertation involves the use of computational chemistry to understand the origins of stereoselectivity in synthetically useful reactions. In collaboration with Prof Wicha's group in Poland, alkylation reactions of azulene precursors in the guanacastepene **A** synthesis were studied and steric effects were determined as the origins of different stereoselectivities observed experimentally. Next, in collaboration with Prof Jung's group in UCLA, an unusual conformational effect on reactivities in a cyclic non-aldol aldol rearrangement was explained using theoretical models. In collaboration with Prof Overman, the stereoselectivities of the dihydroxylations of *cis*-bicyclo[3.3.0]octene intermediates for total synthesis of chromodorolide **A** were investigated and torsional effects were identified as the control elements here. Other related examples from the literatures were also studied and it was found that the stereoselectivity was greatly affected by the rigidity or flexibility of conformations of reactants. Finally, in collaboration with Prof Antilla, a theoretical study of chiral Brønsted acid-catalyzed allylboration and propargylation reactions was performed. The general reaction mechanisms involving two different models were investigated, and the steric repulsions between the bulky 3,3'-substituents in the catalyst and the substrates were determined to be responsible for the enantioselectivities.

The dissertation of Hao Wang is approved.

Neil Kamal Garg

Jing Huang

Kendall N. Houk, Committee Chair

University of California, Los Angeles

2013

DEDICATION

This thesis is dedicated to my wife and my parents.

TABLE OF CONTENTS

LIST OF FIGURES	ix
LIST OF TABLES	xii
ACKNOWLEDGEMENTS	xiii
VITA.....	xv
Chapter 1. Reversible Photochemically-Gated Transformation of A Hemicarcerand to a Carcerand.....	1
1.1 Abstract	1
1.2 Introduction.....	1
1.3 Results and Discussion	2
1.4 Experimental Section.....	14
1.5 Conclusion	16
1.6 References.....	17
Chapter 2: Steric Control of α- and β-Alkylation of Azulenone Intermediates in a Guanacastepene A Synthesis.....	19
2.1 Abstract	19
2.2 Introduction.....	19
2.3 Results and Discussion	21
2.4 Conclusion	28
2.5 References.....	29
Chapter 3. Computational Elucidation of the Origins of Reactivity and Selectivity in Non-Aldol Aldol Rearrangements of Cyclic Epoxides	31
3.1 Abstract	31

3.2 Introduction.....	31
3.3 Results and Discussion	32
3.4 Conclusion	41
3.5 References.....	42
Chapter 4. Origins of Stereoselectivities of Dihydroxylations of <i>cis</i>-Bicyclo[3.3.0]octenes	43
4.1 Abstract.....	43
4.2 Introduction.....	43
4.3 Results and Discussion	45
4.3.1 Experimental Studies.....	45
4.3.2 Computational Studies	46
4.3.3 Literature Examples of Dihydroxylation of Other <i>cis</i> -Bicyclo[3.3.0]octenes	50
4.4 Conclusion	64
4.5 References.....	65
Chapter 5. Origins of Stereoselectivities in Chiral Phosphoric Acid-Catalyzed Allylboration and Propargylations of Aldehydes	68
5.1 Abstract.....	68
5.2 Introduction.....	69
5.3 Results and Discussion	72
5.3.1 Investigation of the reaction mechanism.....	72
5.3.2 Model of the phosphoric acid-catalyzed allylboration reaction	74
5.3.3 Activation barrier for uncatalyzed and catalyzed reactions	79
5.3.4 Origins of Enantioselectivity.....	83
5.4 Conclusion	92

5.5 References.....	93
---------------------	----

LIST OF FIGURES

Figure 1.1. Gating in container molecules converts a hemicarcerand (left) into a carcerand (right).....	2
Figure 1.2. Synthesis of di-anthracene hemicarcerand 3.....	3
Figure 1.3. ¹ H NMR spectrum of 3.....	3
Figure 1.4. ¹³ C NMR spectrum of 3.....	4
Figure 1.5. Photochemical reversible transformations between the open hemicarcerand 3 and closed carcerand 4.....	5
Figure 1.6. Partial ¹ H NMR spectra (400 MHz, CDCl ₃) of (a) host 3 (b) irradiation of host 3 with light at 350 nm for 1 h, (c) irradiation of b with light at 254 nm for 1 h or heating at 60 °C for 20 min, (d) irradiation of c with light at 350 nm for 1 h.....	6
Figure 1.7. Fluorescence spectra of (a) 3 upon irradiation at 350 nm for 1 h (CHCl ₃ , 10 ⁻⁴ M, rt). (b) 4 upon irradiation at 254 nm for 1 h (CHCl ₃ , 10 ⁻⁴ M, rt). (c) Changes in the fluorescence intensity at 420 nm upon alternating irradiation of 350 and 254 nm light.....	8
Figure 1.8. Energy minimized structures of (a) open state host 3 (b) closed state host 4 (c) carceplex 4@1,4-(MeO) ₂ C ₆ H ₄ using Schrödinger Macromodel.....	9
Figure 1.9. Partial ¹ H NMR spectra (400 MHz, CDCl ₃) of (a) host 3 (b) addition of 1 equiv of 1,4-(MeO) ₂ C ₆ H ₄ into host 3 solution without irradiation, (c) 4@1,4-(MeO) ₂ C ₆ H ₄ , (d) c after 4 weeks in dark and rt, (e) irradiation of c with light at 254 nm for 1 h or heating at 60 °C for 20 min, (f) guest 1,4-(MeO) ₂ C ₆ H ₄	11
Figure 1.10. Molecular modelling of complexation of 4 with propofol (2,6-diisopropylphenol) using Schrödinger Macromodel.....	14
Figure 2.1. Routes for the alkylation of two different azulene intermediates.....	21
Figure 2.2. The lowest energy chair-like conformation of enolate A.....	22
Figure 2.3. Transition structures for the α- and β-attack of methyl bromide on enolate A.....	24
Figure 2.4. The lowest energy conformation of enolate B.....	25
Figure 2.5. Transition structures for the α- and β-attack of methyl bromide on enolate B.....	27
Figure 2.6. Optimized model reactants A and B from the side view.....	28

Figure 3.1. Non-aldol aldol rearrangement	32
Figure 3.2. Non-aldol aldol rearrangement of 4a and 4b	33
Figure 3.3. Experimental results of non-aldol aldol rearrangement of 4a and 4b	33
Figure 3.4. B3LYP optimized geometries of 4a (A and B) and transition structures (C and D) for the non-aldol aldol rearrangement	35
Figure 3.5. B3LYP optimized geometries of 4b (A' and B') and transition structures (C' and D') for the non-aldol aldol rearrangement	36
Figure 3.6. Energy profile for the non-aldol aldol pathways of 4a and 4b	37
Figure 3.7. Transition structures for the elimination pathways of 4a (M) and 4b (M')	38
Figure 3.8. Energy profile for the non-aldol aldol rearrangement and elimination pathway of 4a	39
Figure 3.9. Energy profile for the non-aldol aldol rearrangement and elimination pathway of 4b	39
Figure 3.10. Experimental results of non-aldol aldol rearrangement of 7a and 7b	40
Figure 3.11. Half-chair transition state models for the non-aldol aldol rearrangement of 7a and 7b	41
Figure 4.1. Structure of chromodorolide A (1) and experimental results of dihydroxylation of <i>cis</i> -oxabicyclo[3.3.0]octenone 3	44
Figure 4.2. Synthesis of <i>cis</i> -oxabicyclo[3.3.0]octenone 3 and its dihydroxylation with OsO ₄ in aqueous <i>tert</i> -butanol	45
Figure 4.3. Optimized β and α -dihydroxylation transition structures of <i>cis</i> -oxabicyclo[3.3.0]octanone 3	48
Figure 4.4. (a) Optimized structure of <i>cis</i> -oxabicyclo[3.3.0]octenone 3. (b) The torsional of interest viewed along the green bond	50
Figure 4.5. Selected literature examples of dihydroxylation of <i>cis</i> -bicyclo[3.3.0]octenes using osmium reagents	58
Figure 4.6. Three fused cyclopentene compounds and their optimized geometries	59
Figure 4.7. Optimized β and α -dihydroxylation transition structures of <i>cis</i> -bicyclo[3.3.0]octenes 9, 11 and 13	61
Figure 4.8. Optimized structures of (a) R3a and R3a' (b) R9 and R9'	63

Figure 4.9. Optimized structures of (a) R11 and R11' (b) R13 and R13'	64
Figure 5.1. Chiral phosphoric acid-catalyzed allylboration and propargylations of benzaldehyde	70
Figure 5.2. Two models for the chiral phosphoric acid-catalyzed allylboration and propargylations of benzaldehyde	71
Figure 5.3. Three possible sites of coordination in the phosphoric acid-catalyzed allylboration reaction	72
Figure 5.4. Optimized transition state of the uncatalyzed allylboration of benzaldehyde at the B3LYP/6-31G* level of theory	73
Figure 5.5. Optimized transition states of different mechanisms at the B3LYP/6-31G* level of theory	73
Figure 5.6. Optimized transition state structures of (a) TS4, TS4' in pathway i (eq) and (b) TS5, TS5' in pathway ii (ax) at the B3LYP/6-31G* level of theory	76
Figure 5.7. Top and bottom view of electrostatic potential of TS from Figure 5.4	77
Figure 5.8. Models for the phosphoric acid-catalyzed allylboration reaction	78
Figure 5.9. Reaction profile for the uncatalyzed allylboration reaction of 1 with 2 by B3LYP	79
Figure 5.10. Reaction profiles for the allylboration reaction of 1 with 2 catalyzed by chiral phosphoric acid using E by B3LYP	81
Figure 5.11. Reaction profiles for the allylboration reaction of 1 with 2 catalyzed by chiral phosphoric acid using A by B3LYP	82
Figure 5.12. Optimized structures of TSr1-E and TSs1-E for E, TSr1-A and TSs1-A for A	84
Figure 5.13. (a) Side view of TSr1-E and TSs1-E. (b) Structures of 1A and 1B. (c) 3D structures of 1A in TSr1-E. (d) 3D structures of 1A in TSs1-E	88
Figure 5.14. Optimized structures of TSr1'-E and TSs1'-E for E, TSr1'-A and TSs1'-A for A	90
Figure 5.15. (a) 3D structure of TSr1'-E without the benzaldehyde. (b) 3D structure of TSs1'-E without the benzaldehyde	91

LIST OF TABLES

Table 1.1. Complexation of 4 with various guest molecules and the chemical shift changes of corresponding Hs (before and after complexations) on the guests.....	13
Table 2.1. Summary of the free energies of 1α , 1β , 2α , 2β	24
Table 4.1. SciFinder substructure searches	51
Table 4.2. SciFinder reaction (substructure) searches	52
Table 4.3. SciFinder control substructure searches	52
Table 4.4. Relevant literature examples from the SciFinder literature searches (Tables 4.1–4.3).....	53

ACKNOWLEDGEMENTS

Chapter 1

This chapter is a version of:

Wang, H.; Liu, F.; Helgeson, R. C.; Houk, K. N. “Reversible Photochemically-Gated Transformation of A Hemicarcerand to a Carcerand” *Angew. Chem., Int. Ed.* **2013**, *52*, 655-659.

Permission was given for use of this work in this thesis.

Kendall N. Houk was the PI for this work.

Chapter 2

This chapter is a version of:

Wang, H.; Michalak, K.; Michalak, M.; Jimenez-Oses, G.; Wicha, J.; Houk, K. N. “Steric Control of α - and β -Alkylation of Azulenone Intermediates in a Guanacastepene A Synthesis” *J. Org. Chem.* **2010**, *75*, 762–766.

Permission was given for use of this work in this thesis.

Kendall N. Houk was the PI for this work.

Chapter 3

This chapter is a version of:

Wang, H.; Allen, D. A.; Jung, M. E.; Houk, K. N. “Computational Elucidation of the Origins of Reactivity and Selectivity in Non-Aldol Aldol Rearrangements of Cyclic Epoxides” *Org. Lett.* **2011**, *13*, 3238-3241.

Permission was given for use of this work in this thesis.

Kendall N. Houk was the PI for this work.

Chapter 4

This chapter is a version of:

Wang, H.; Kohler, P.; Overman, L. E.; Houk, K. N. “Origins of Stereoselectivities of Dihydroxylations of cis-Bicyclo[3.3.0]octenes” *J. Am. Chem. Soc.* **2012**, *134*, 16054–16058.

Permission was given for use of this work in this thesis.

Kendall N. Houk was the PI for this work.

Chapter 5

This chapter is a version of:

Wang, H.; Jain, P.; Antilla, J. C.; Houk, K. N. “Origins of Stereoselectivities in Chiral Phosphoric Acid Catalyzed Allylboration and Propargylations of Aldehydes” *J. Org. Chem.* **2013**, *78*, 1208–1215.

Permission was given for use of this work in this thesis.

Kendall N. Houk was the PI for this work.

Funding

This work was supported by the National Institute of General Medical Sciences, National Institutes of Health (GM 36770), National Science Foundation (CHE 0614591). Computations were performed on the Extreme Science and Engineering Discovery Environment (XSEDE), and on the UCLA IDRE Hoffman2 cluster.

VITA

HAO WANG

EDUCATION:

Hong Kong Baptist University, Hong Kong SAR, China December 2007
Master of Science in Organic Chemistry

Wuhan University, Hubei, China June 2005
Bachelor of Science in Applied Chemistry

WORK EXPERIENCE:

Amgen Inc, Thousand Oaks, CA Summer 2012
Developed Cu-catalyzed C-H arylation methodologies for multicomponent synthesis of quinolinones, optimized reaction conditions and maximized yields up to 84%

RESEARCH EXPERIENCE:

University of California, Los Angeles 09/2008 – Present
Designed and synthesized photoswitchable hemicarcerand, investigated its complexation abilities with different guest molecules. Explored mechanisms and stereoselectivities of organic reactions using computational chemistry.

Hong Kong Baptist University, Hong Kong SAR, China 01/2006 – 12/2007
Designed and synthesized cholic-acid based fluorescent probes for metals and biological active molecules such as ATP

HONORS & AWARDS:

Thomas L. and Ruth F. Jacobs Dissertation Award, UCLA June 2013
Christopher S. Foote Graduate Fellowship in Organic Chemistry, UCLA April 2011

PRESENTATIONS & POSTERS:

“One-pot, Three-Component Synthesis of Multisubstituted Quinolinones via Click-Amidation-Knoevenagel-(C-H Arylation) Cascade Reaction”. Amgen Summer Intern Presentation, Thousand Oaks, CA 09/2012

“Study of Activation Effects of Triazolyl Related Heteroaryl Groups on S_NAr Reactions”. Amgen Summer Intern/Co-op Poster Session, Thousand Oaks, CA 07/2012

PUBLICATIONS:

Wang, H.; Liu, F.; Helgeson, R. C.; Houk, K. N. “Reversible Photochemically-Gated Transformation of A Hemicarcerand to a Carcerand” *Angew. Chem., Int. Ed.* **2013**, *52*, 655-659.

Liu, F.; Wang, H.; Houk, K. N. “Gating in Host-guest Chemistry” *Curr. Org. Chem.* **2013**, *17*, 1470-1480.

Mejuch, T.; Gilboa, N.; Gayon, E.; Wang, H.; Houk, K. N.; Marek, I. “Axial Preferences in Allylation Reactions via the Zimmerman-Traxler Transition State” *Acc. Chem. Res.* **2013**, *46*, 1659-1669.

Lin, H.-K.; Pei, W.-B.; Wang, H.; Houk, K. N.; Krauss, I. J. “Enantioselective Homocrotylboration of Aliphatic Aldehydes” *J. Am. Chem. Soc.* **2013**, *135*, 82–85.

Wang, H.; Jain, P.; Antilla, J. C.; Houk, K. N. “Origins of Stereoselectivities in Chiral Phosphoric Acid Catalyzed Allylboration and Propargylations of Aldehydes” *J. Org. Chem.* **2013**, *78*, 1208–1215.

Wang, H.; Kohler, P.; Overman, L. E.; Houk, K. N. “Origins of Stereoselectivities of Dihydroxylations of cis-Bicyclo[3.3.0]octenes” *J. Am. Chem. Soc.* **2012**, *134*, 16054–16058.

Jain, P.; Wang, H.; Houk, K. N.; Antilla, J. C. “Brønsted Acid-Catalyzed Asymmetric Propargylation of Aldehydes” *Angew. Chem., Int. Ed.* **2012**, *51*, 1391-1394.

Liu, F.; Wang, H.; Houk, K. N. “Gated Container Molecules” *Sci. China. Chem.* **2011**, *54*, 2038-2044.

Wang, H.; Allen, D. A.; Jung, M. E.; Houk, K. N. "Computational Elucidation of the Origins of Reactivity and Selectivity in Non-Aldol Aldol Rearrangements of Cyclic Epoxides" *Org. Lett.* **2011**, *13*, 3238-3241.

Gilboa, N.; Wang, H.; Houk, K. N.; Marek, I. "Axial Preferences in Allylations via the Zimmerman-Traxler Transition State" *Chem. Eur. J.* **2011**, *17*, 8000–8004.

Wang, H.; Michalak, K.; Michalak, M.; Jimenez-Oses, G.; Wicha, J.; Houk, K. N. "Steric Control of α - and β -Alkylation of Azulenone Intermediates in a Guanacastepene A Synthesis" *J. Org. Chem.* **2010**, *75*, 762–766.

Wang, H.; Chan, W.-H. "Cholic acid-based fluorescent probe for enantioselective recognition of trifunctional aminoacids" *Org. Biomol. Chem.* **2008**, *6*, 929-934.

Wang, H.; Chan, W.-H. "A cholic acid-based fluorescent chemosensor for the detection of ATP" *Org. Biomol. Chem.* **2008**, *6*, 162-168.

Wang, H.; Chan, W.-H. "Cholic acid-based fluorescent sensor for mercuric and methyl mercuric ion in aqueous solutions" *Tetrahedron.* **2007**, *63*, 8825-8830.

Chapter 1. Reversible Photochemically-Gated Transformation of A Hemicarcerand to a Carcerand

1.1 Abstract

Introduction of two anthracene groups into a linker of a hemicarcerand creates a new type of photochemically controlled gated hemicarcerand. The reversible opening and closing of the “gate” of the host is well controlled photochemically. Host-guest complexations and decomplexations are studied by a variety of spectroscopic methods as well as molecular modelling. Irradiation with light of different wavelengths was demonstrated to control encapsulation and release of the guest molecules such as 1,4-dimethoxybenzene.

1.2 Introduction

In the 1980s, Cram pioneered the synthesis of container molecules, hemicarcerands and carcerands, the latter able to imprison guest molecules.¹ Hemicarcerands are selective host molecules whose binding affinities mainly depends on the size of the guest molecule. Hemicarcerands are important host molecules in research fields such as drug delivery, phase-transfer catalysis, and molecular recognition.² Calculations led to an understanding of how guests enter and escape from the container molecules via a thermal gating mechanism.³ Gating converts hemicarcerands (open gate) into carcerands (closed gate) (Figure 1.1). Gating has been achieved previously with stimuli such as heat,⁴ redox⁵ or acid/base chemistry.⁶ Photochemical processes can be built into container molecules as switching mechanisms;⁷ Rebek used the cis-trans photoisomerization of azobenzene,⁸ and

Mattay used the photoreactivities of anthracene.⁹ However, the use of photoswitchable gates to interconvert hemicarcerands and carcerands has not been demonstrated.¹⁰ We report herein the synthesis of a reversible photoswitchable gated hemicarcerand based on the photochemical properties of anthracene. The reversible photochemical gating is demonstrated to control host-guest complex stability, which could be important for delivery systems, engineered to encapsulate and release guest molecules upon radiation.

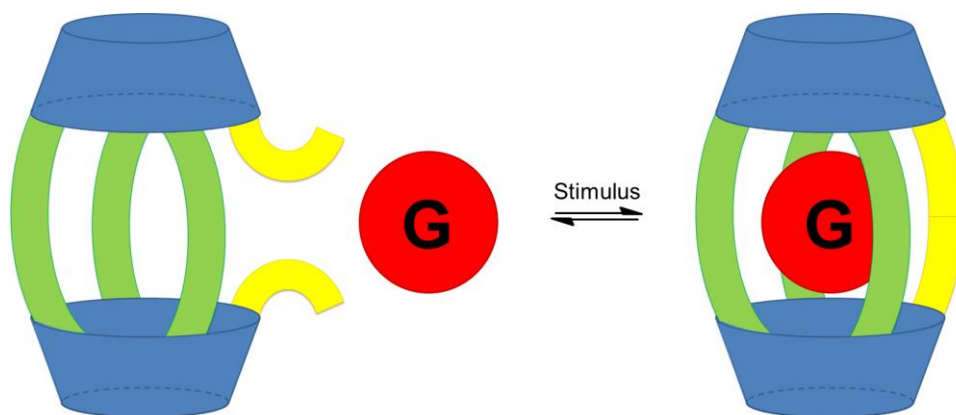


Figure 1.1. Gating in container molecules converts a hemicarcerand (left) into a carcerand (right).

1.3 Results and Discussion

The synthesis of the new hemicarcerand is outlined in Figure 1.2. Diol **2** can be prepared from precursor **1** in about 30% yield according to the procedure described by Cram.¹¹ Treating the diol **2** with 9-chloromethylantracene using cesium carbonate as the base produces the hemicarcerand **3** as a yellow solid. The structure of **3** was characterized by ¹H NMR (Figure 1.3) and ¹³C NMR (Figure 1.4) which both showed the typical signals for the anthracene moieties.

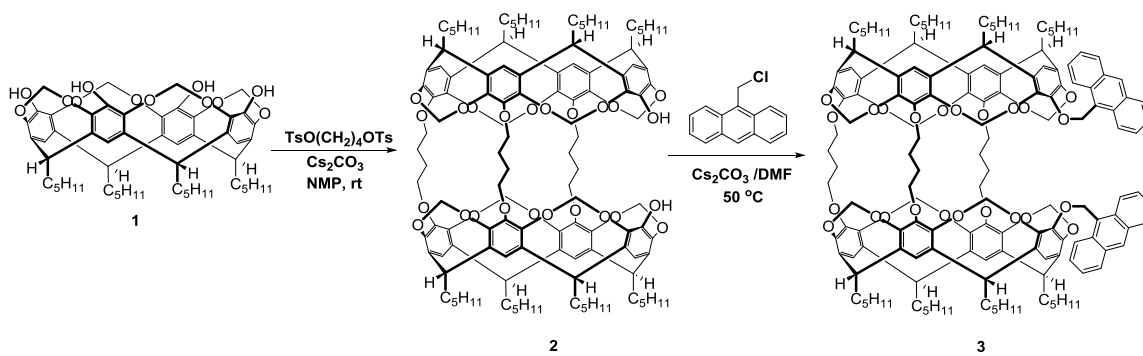


Figure 1.2. Synthesis of di-anthracene hemicarcerand **3**.

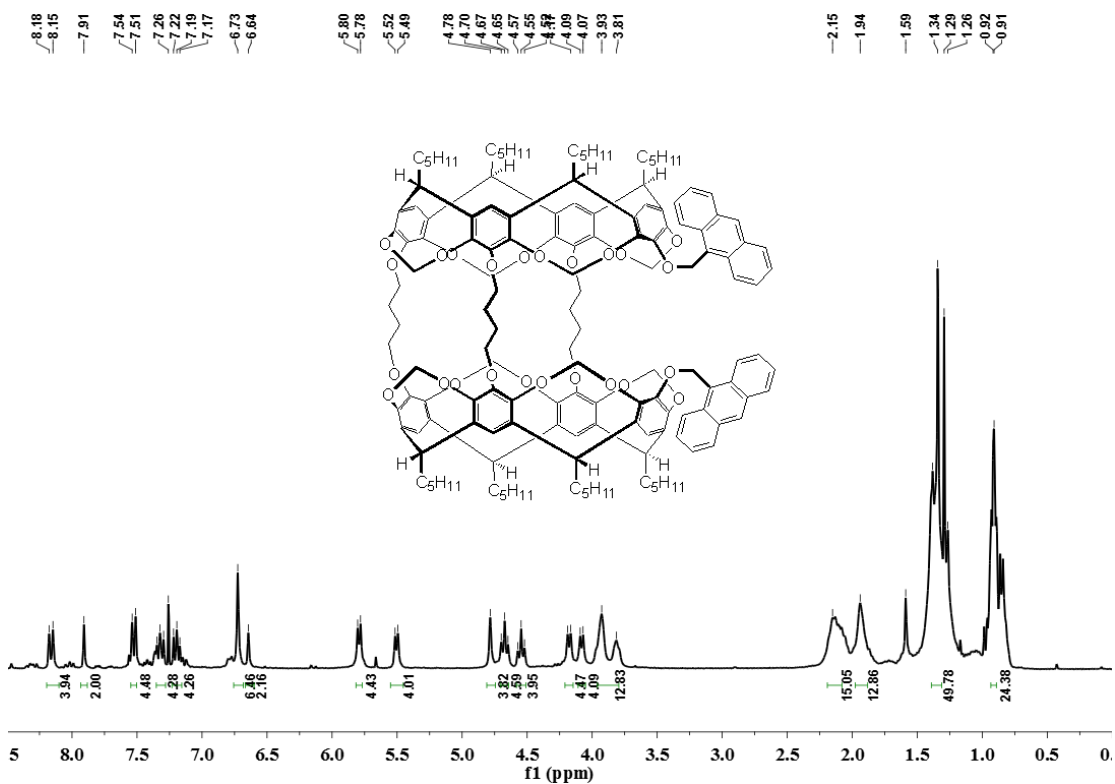


Figure 1.3. ¹H NMR spectrum of **3**.

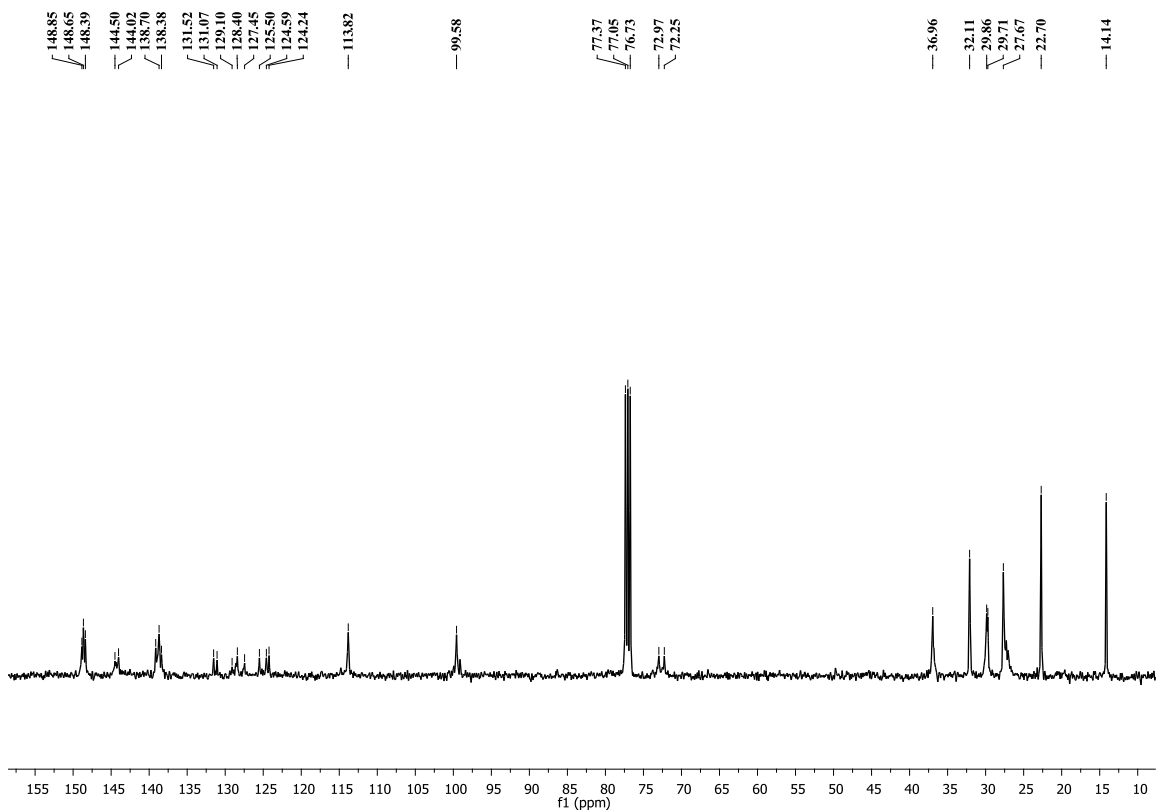


Figure 1.4. ^{13}C NMR spectrum of **3**.

The photochemical properties of this system were explored to determine if the hemicarcerand could be converted to a carcerand that traps guest molecules. We investigated the photochemical cycle between the open state host **3** and closed state host **4** (Figure 1.5) using ^1H NMR spectroscopy.

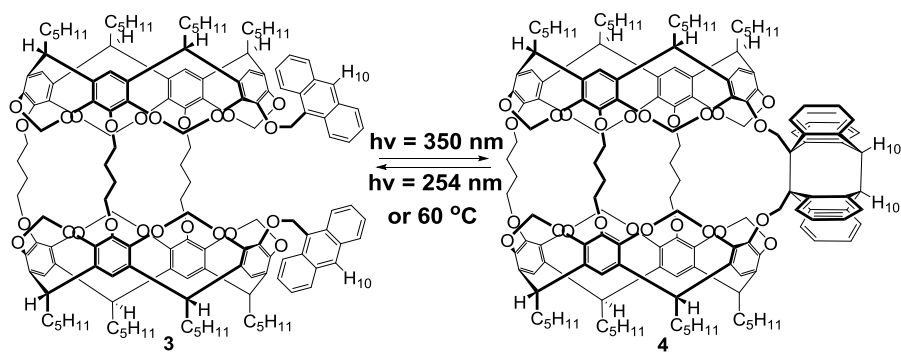


Figure 1.5. Photochemical reversible transformations between the open hemicarcerand **3** and closed carcerand **4**.

To investigate the intramolecular anthracene photodimerization process of **3**, a dilute solution of **3** (10^{-4} M) in degassed CDCl_3 was irradiated with 350 nm UV light.^{12, 13} Upon irradiation at 350 nm for 1 h, the ^1H NMR spectrum of **3** in CDCl_3 showed the disappearance of the anthracene peaks from 7.20-8.20 ppm and the appearance of a new peak (singlet) around 4.40 ppm (Figure 1.6b). The aromatic protons of anthracene dimer in **4** overlap with other aromatic protons of the host molecules, appearing as a large multiplet at 6.85 ppm (Figure 1.6b). Another indication of the formation of the intramolecular cyclodimer **4** is the characteristic chemical shift of the tertiary bridgehead protons H_{10} (Figure 1.5). In the open state **3**, H_{10} is an aromatic proton that is shown as a singlet at 7.91 ppm (Figure 1.6a). However, when the photodimerization process takes place, H_{10} is converted to an aliphatic proton in the closed state **4**, changing its hybridization from sp^2 to sp^3 . In the new ^1H NMR spectrum, this tertiary bridgehead proton H_{10} was identified as the new singlet at 4.40 ppm (marked as asterisk in Figure 1.6b) due to 2 hydrogens. The chemical shift changes for the anthracene moieties and tertiary bridgehead protons H_{10} after the photodimerization in this system are consistent with literature examples.¹³ The cycloreversion of the photodimer **4** back to open state **3** could be achieved by short wavelength UV irradiation. Upon irradiation of the same

solution at 254 nm for 1 h, the starting state is restored, as seen from the reappearance of the anthracene peaks from 7.20-8.20 ppm in the ^1H NMR spectrum (Figure 1.6c). The reversible switching process could be repeated several times without noticeable degradation; two iterations are shown in Figure 1.6. The photodimer **4** could also be converted back to open state **3** thermally. To open the cycloadduct **4**, the CDCl_3 solution of **4** (Figure 1.6b) was heated to 60 °C for about 20 min. The resulting solution gave a spectrum identical to Figure 1.6c.

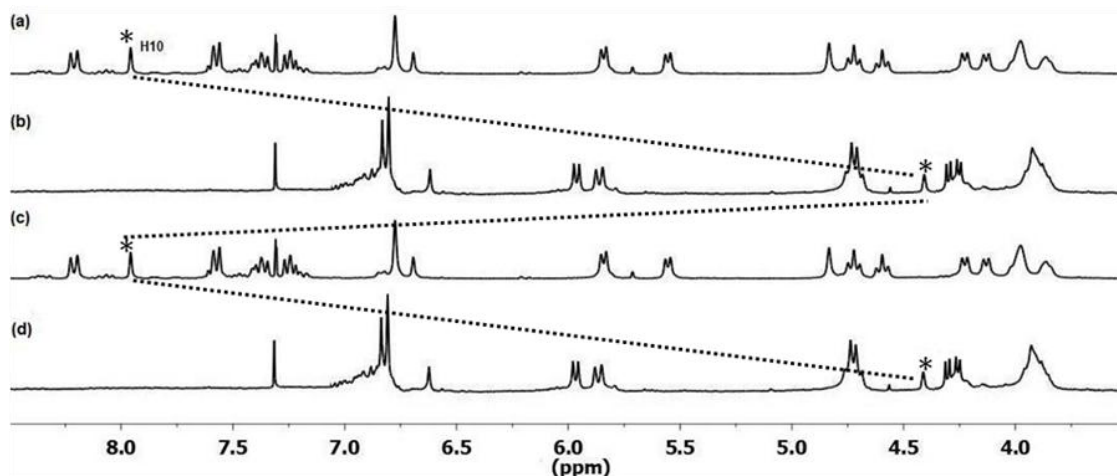


Figure 1.6. Partial ^1H NMR spectra (400 MHz, CDCl_3) of (a) host **3** (b) irradiation of host **3** with light at 350 nm for 1 h, (c) irradiation of b with light at 254 nm for 1 h or heating at 60 °C for 20 min, (d) irradiation of c with light at 350 nm for 1 h.

The photoresponsive properties of host **3** can also be followed by fluorescence spectroscopy. Photodimerization eliminates the characteristic fluorescence of anthracene in the closed state **4**. Experiments showed that when the solution of **3** was irradiated at 350 nm for 1 h, the typical emission band of anthracene with relative maxima at 420 nm decreases gradually in intensity (Figure 1.7a), implying that **3** was gradually converted into photodimer **4**, as reflected by the quenching of the fluorescence intensity. The

photoreaction resulted in a stable photodimer **4**, as the fluorescence did not change after weeks. The fluorescence intensity of the system, however, recovered after irradiation of the same solution at 254 nm for 1 h. As shown in Figure 1.7b, irradiation of the solution of **4** with 254 nm for 30 min leads to an increase of the fluorescence of the system to more than 50% of the original intensity (line 2), and after 1 h, the intensity recovered to 99% of the original level (line 5). This indicates that the reverse reaction takes place, transforming **4** to **3** with photoinduced cleavage of the anthracene dimer, and recovering the anthracene emission. The fluorescence of the system could also be recovered thermally, as indicated by line 6 in Figure 1.7b, which is the fluorescence of the system after 20 min heating at 60 °C. Several cycles of alternate irradiation at 350 and 254 nm indicated good reversibility without detectable degradation of the system (Figure 1.7c).

The progress of the photodimerization was also monitored by TLC (hexane/EtOAc = 8/1), which showed only one band with $R_f = 0.64$ after the completion of the photodimerization. Photodimer **4** was purified after photolysis at 350 nm. The HRMS indicated the molecular ion of photoproduct **4** has the same mass as the parent open state host **3**. This confirms the [4+4] photodimerization of anthracene as the major process taking place photochemically, and excludes the possibility of photoreaction between **3** and other impurities in solutions. All these spectroscopic results strongly suggest that **3** is able to form a stable intramolecular photodimer **4** through an intramolecular [4+4] cycloaddition of the two anthracene units.

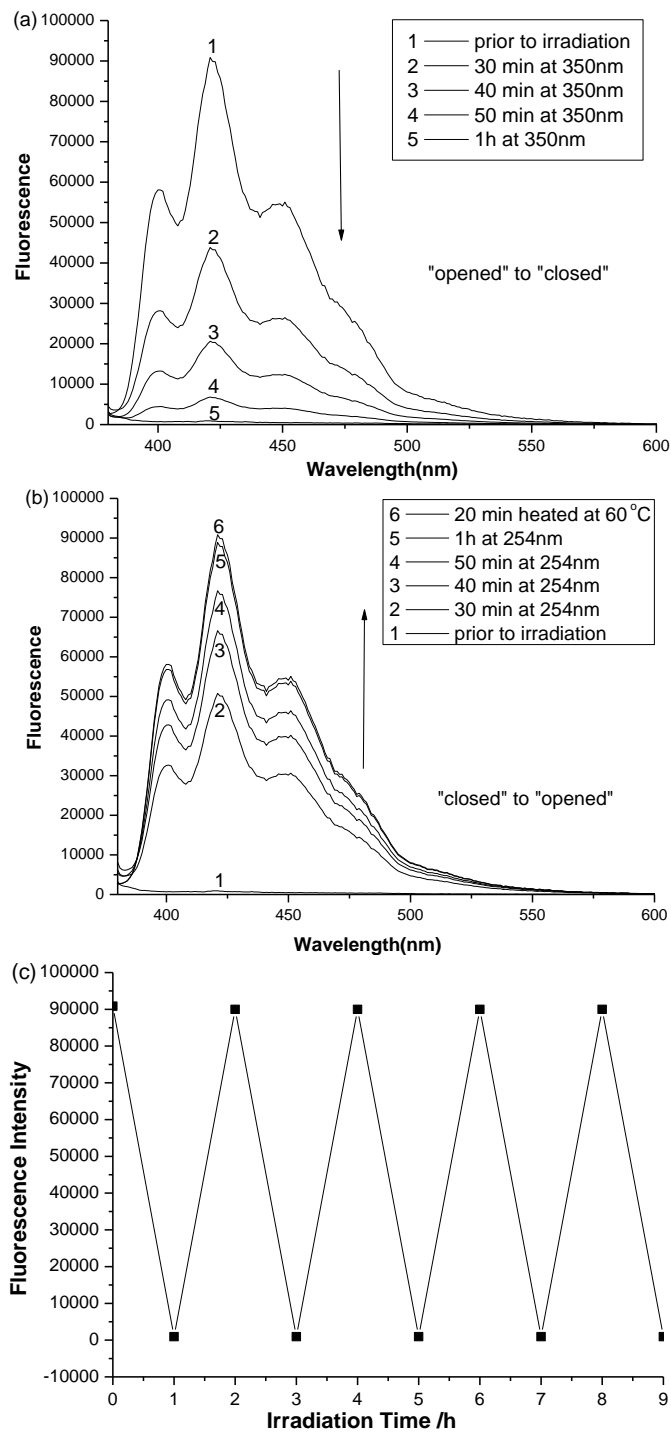


Figure 1.7. Fluorescence spectra of (a) **3** upon irradiation at 350 nm for 1 h (CHCl_3 , 10^{-4} M, rt). (b) **4** upon irradiation at 254 nm for 1 h (CHCl_3 , 10^{-4} M, rt). (c) Changes in the fluorescence intensity at 420 nm upon alternating irradiation of 350 and 254 nm light.

The structures of different states of the host modeled with OPLS in MacroModel are shown in Figure 1.8. In Figure 1.8a, the two anthracene moieties are nearly parallel to each other due to intramolecular π - π stacking interactions. The two anthracenes are separated by proper distances; they are able to form an intramolecular photodimer without introducing much strain to the host system as shown in Figure 1.8b.

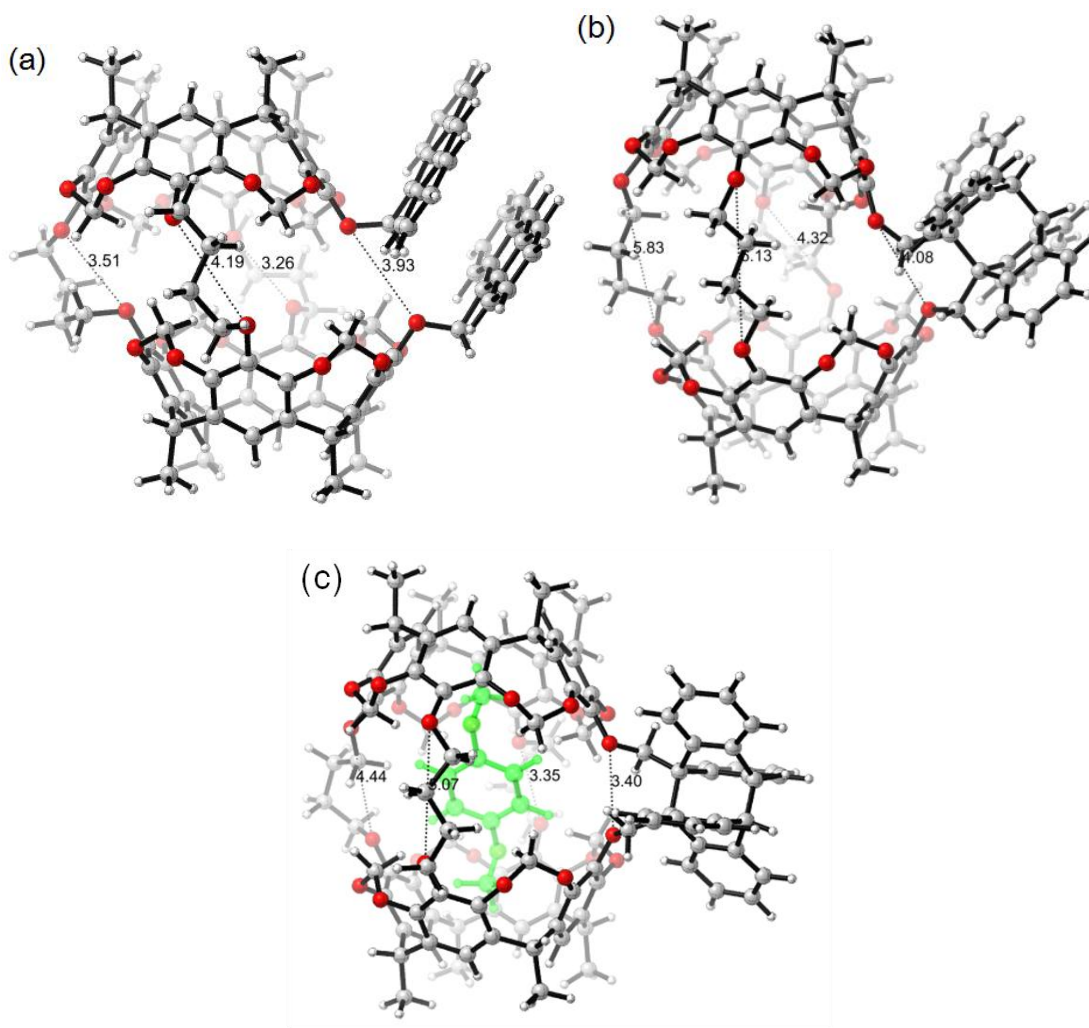


Figure 1.8. Energy minimized structures of (a) open state host **3** (b) closed state host **4** (c) carceplex **4O**1,4-(MeO)₂C₆H₄ using Schrödinger MacroModel (OPLS_2005, GB/SA CHCl₃).

The hemicarcerand was then used to complex various guest molecules such as para-dimethoxybenzene, 1,4-(MeO)₂C₆H₄. At first, the complexation of **3** with 1,4-(MeO)₂C₆H₄ was studied by ¹H NMR spectroscopy. As shown in Figure 1.9b, when 1.0 equivalent of 1,4-(MeO)₂C₆H₄ was added to a CDCl₃ solution of **3**, the proton signals on the guest showed no chemical shift change. Solvent deuteriochloroform is the predominant guest here. So even if a hemicarceplex was formed between **3** and 1,4-(MeO)₂C₆H₄, its concentration is so low to be observed. When diphenyl ether¹⁴ was used as the solvent, NMR spectra indicate that a hemicarceplex is formed: to a 10⁻⁴ M solution of **3** in 5 ml degassed Ph₂O was added 1.4 g 1,4-(MeO)₂C₆H₄, and the ¹H NMR spectrum of the mixture was measured. Due to the large peaks of the solvent Ph₂O, the resolution of the spectrum was low, but a singlet at -0.32 ppm was observed. This indicates that **3** forms a hemicarceplex with 1,4-(MeO)₂C₆H₄: the upfield signal is due to the methyl protons of the guest in the hemicarceplex **3**⊙1,4-(MeO)₂C₆H₄.

The Ph₂O mixture was irradiated at 350 nm for 1 h and then poured into 10 ml of methanol. The precipitate was dissolved in CDCl₃ and the ¹H NMR was shown as Figure 1.9c. The methyl protons of the guest showed a dramatic upfield shift from 3.78 to -0.37 ppm ($\Delta\delta = 4.15$ ppm), and the anthracene peaks of the host **3** disappeared (Figure 1.9c). This indicates that after closing the gate of **3**, a carceplex is formed between the carcerand **4** and the guest. MALDI mass spectra indicate formation of this carceplex. The carceplex **4**⊙1,4-(MeO)₂C₆H₄ can stay in the dark at ambient temperature more than 4 weeks without detectable release of the guest molecule (Figure 1.9d).¹⁵ This indicates that after closing the “gate” and transformation from **3** to **4** upon irradiation at 350 nm, the

portal size of the host was reduced, which increased the activation energy for the decomplexation. As a result, a carceplex was formed and was stable at room temperature. The release of the guest molecules, however, could be accomplished readily photochemically or thermally, due to opening of the gate. Upon irradiation at 254 nm or heating at 60 °C of the previously generated carceplex **4**⊙1,4-(MeO)₂C₆H₄ in solution, the methyl signals of 1,4-(MeO)₂C₆H₄ exhibited a downfield shift along with the reappearance of the anthracence peaks in the ¹H NMR spectroscopy (Figure 1.9e). This indicates that the reopening of the di-anthracence gate converted **4**⊙1,4-(MeO)₂C₆H₄ carceplex to hemicarceplex **3**⊙1,4-(MeO)₂C₆H₄ and created a larger portal of the host. As a result, the activation energy for decomplexation in the open state **3**⊙1,4-(MeO)₂C₆H₄ is decreased and the incarcerated guest 1,4-(MeO)₂C₆H₄ can egress easily. The gate-opened hemicarcerand is then almost exclusively filled with the solvent CDCl₃.

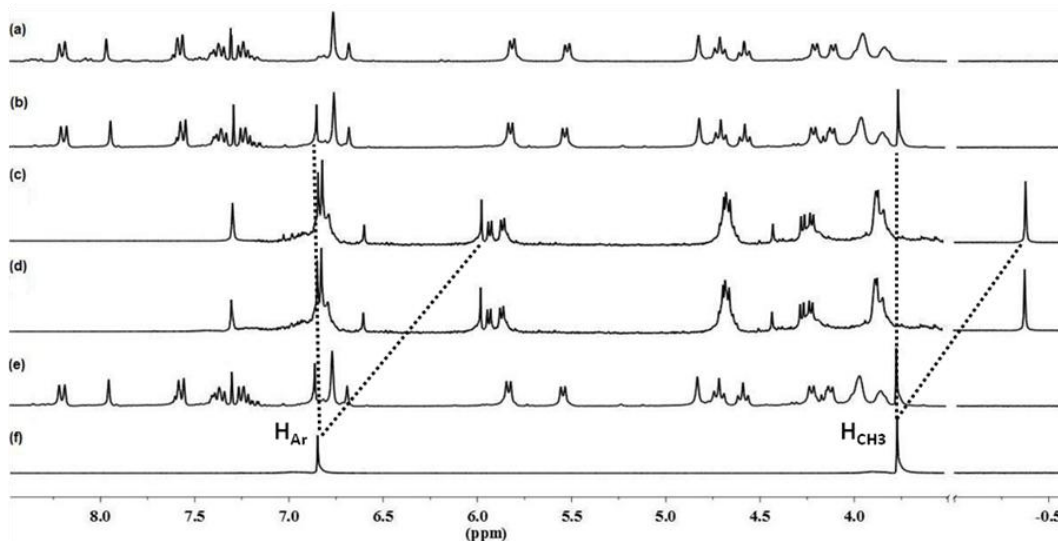


Figure 1.9. Partial ¹H NMR spectra (400 MHz, CDCl₃) of (a) host **3** (b) addition of 1 equiv of 1,4-(MeO)₂C₆H₄ into host **3** solution without irradiation, (c) **4**⊙1,4-(MeO)₂C₆H₄, (d) c after 4 weeks in dark and rt, (e) irradiation of c with light at 254 nm for 1 h or heating at 60 °C for 20 min, (f) guest 1,4-(MeO)₂C₆H₄.

In Cram's studies, the decomplexation of hemicarceplex with tetramethylene bridge can also be achieved thermally, but it often requires high temperature and long time.¹¹ We have identified this thermal decomplexation occurs through a conformational change in host molecules.³ By contrast, the thermal gating mechanism for our system is the transformation of anthracene dimer to monomer, which created a large portal of the host through which the guest was able to exit.

Molecular modelling was used to study the carceplex further. The energy-minimized structure of **4**⊖1,4-(MeO)₂C₆H₄ showed a compact host-guest system. The cavity of **4** is spacious enough and complementary for the inclusion of 1,4-(MeO)₂C₆H₄ (Figure 1.8c). The two OMe groups of the guest nicely fit into the two hemispheres of the host, achieving stabilizing van der Waals interactions with the aromatic rings of the host. This is also consistent with the ¹H NMR observations that the methyl protons undergo dramatic upshifts due to the shielding effects of the aromatic rings.

A variety of small aromatic and aliphatic molecules were able to form carceplexes analogues to **4**⊖1,4-(MeO)₂C₆H₄. These include toluene, o-xylene, m-xylene, p-xylene, anisole, 4-methylanisole, 1,1,2,2-tetrachloroethane, 1,1,2,2-tetrabromoethane (Table 1.1). Larger compounds were also explored as guests, including t-butylbenzene, 4-methyl-5-(2-hydroxyethyl)thiazole¹⁶ and 2,6-diisopropylphenol (Propofol) that is an intravenously administered hypnotic agent. However, no complexes were formed when the host is subjected to similar conditions for host-guest complexation. For

2,6-diisopropylphenol, molecular models show that the two isopropyl groups are so large that propofol does not fit into the cavity of **4** (Figure 1.10).

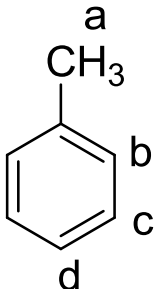
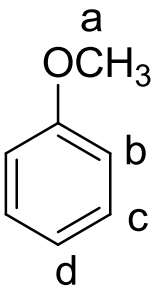
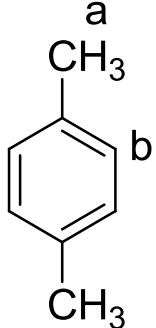
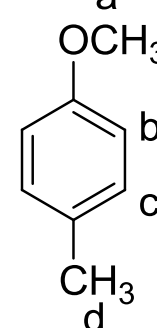
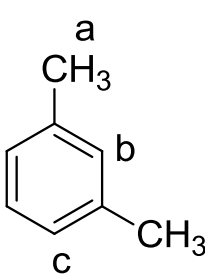
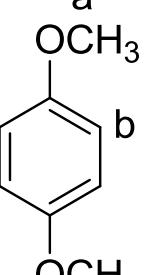
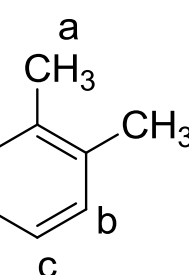
Guest	H	$\Delta\delta$ (ppm)	Guest	H	$\Delta\delta$ (ppm)
	H _a H _b H _c H _d	3.96 1.53 1.85 3.35		H _a H _b H _c H _d	3.87 1.60 1.95 3.30
	H _a H _b	4.17 1.06		H _a H _b H _c H _d	4.01 0.84 0.98 4.21
	H _a H _b H _c H _d	3.17 hidden 1.86 hidden		H _a H _b	4.15 0.85
	H _a H _b H _c	2.34 1.54 1.95	CH _a Cl ₂ —CHCl ₂	H _a	0.95
			CH _a Br ₂ —CHBr ₂	H _a	1.02

Table 1.1. Complexation of **4** with various guest molecules and the chemical shift changes of corresponding Hs (before and after complexations) on the guests.

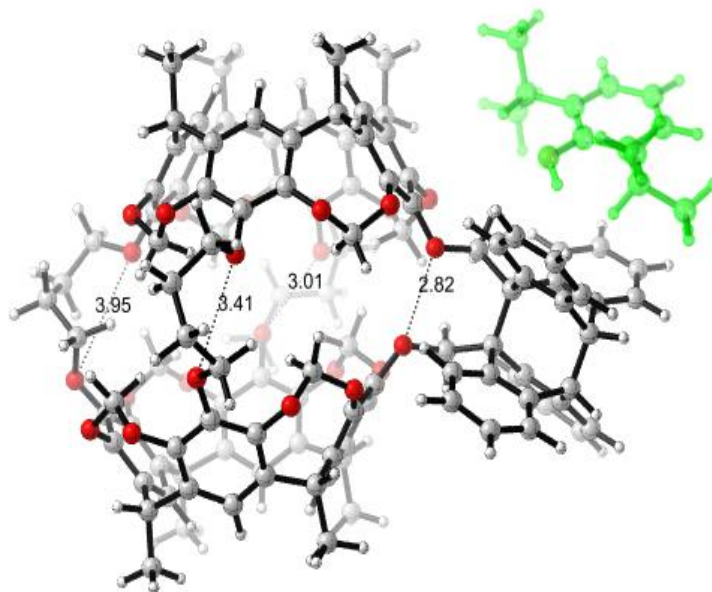


Figure 1.10. Molecular modelling of complexation of **4** with propofol (2,6-diisopropylphenol) using Schrödinger Macromodel (OPLS_2005, GB/SA CHCl_3). (The geometry began with the guest inside the host; the guest came out of the host after the minimization)

1.4 Experimental Section

Host **3**. Diol **2** (192 mg, 0.10 mmol) was dissolved in dry DMF (10 ml), anhydrous Cs_2CO_3 (326 mg, 1 mmol) was added and stirred under Ar for 15 min. 9-chloromethylantracene (68 mg, 0.30 mmol) was then added and the mixture was stirred at 50 °C overnight. The mixture was washed with 1N HCl and extracted with CHCl_3 . The organic solvent was concentrated and the crude product was purified by column chromatography using hexane/EtOAc = 10/1 as the eluent to afford **3** (182 mg, 79%) as a yellow powder. ^1H NMR (CDCl_3 , 400 MHz) δ 0.92 (t, J = 5.4 Hz, CH_3 , 24H), 1.30-1.53 (m, $\text{CH}_2\text{CH}_2\text{CH}_2$, 48H), 1.90-2.21 (m, CHCH_2 , OCH_2CH_2 , 28H), 3.82-3.93 (m, OCH_2CH_2 , 12H), 4.08-4.20 (m, OCH_2O (inner H), 8H), 4.55 (t, J = 7.8 Hz, CHCH_2 , 4H), 4.68 (t, J = 7.8 Hz, CHCH_2 , 4H), 4.79 (s, OCH_2Ar , 4H), 5.50-5.79 (m, OCH_2O (outer H),

8H), 6.65 (s, ArH, 2H), 6.73 (s, ArH, 6H), 7.20-7.33 (m, ArH, 8H), 7.52 (d, $J = 8.1$ Hz, ArH, 4H), 7.91 (s, ArH, 2H), 8.16 (d, $J = 8.1$ Hz, ArH, 4H). ^{13}C NMR (CDCl_3 , 100 MHz) δ 148.9, 148.7, 148.4, 144.5, 144.0, 139.1, 138.7, 138.4, 131.5, 131.1, 129.1, 128.4, 127.5, 125.5, 124.6, 124.2, 113.8, 99.6, 73.0, 72.3, 36.9, 32.1, 29.9, 29.7, 27.7, 22.7, 14.1. MALDI HRMS calcd for $\text{C}_{146}\text{H}_{166}\text{O}_{24}\text{Na}$ 2327.12, found 2326.94 $[\text{M}+\text{Na}]^+$.

Complexation and decomplexation studies:

4⊖1,4-(MeO)₂C₆H₄. To a 10^{-4} M solution of **3** in 5 ml degassed Ph₂O was added 1.4 g 1,4-(MeO)₂C₆H₄. The mixture was irradiated at 350 nm for 1 h and then poured into 10 ml of methanol. The precipitate was collected on a fine-mesh sintered glass funnel and dried under vacuum (25 °C) overnight to give the carceplex as a light yellow solid. ^1H NMR (CDCl_3 , 400 MHz) δ -0.37 (s, OCH₃, 6H), 0.92 (t, $J = 5.4$ Hz, CH₃, 24H), 1.28-1.55 (m, CH₂CH₂CH₂, 48H), 1.90-2.25 (m, CHCH₂, OCH₂CH₂, 28H), 3.78-3.96 (m, OCH₂CH₂, 12H), 4.25-4.35 (m, OCH₂O (inner H), 8H), 4.45 (s, 2H, CH), 4.70-4.80 (m, CHCH₂, OCH₂Ar, 12H), 5.80-5.92 (m, OCH₂O (outer H), 8H), 5.95 (s, ArH, 4H), 6.60 (s, ArH, 2H), 6.75-6.92 (m, ArH, 22H). MALDI HRMS calcd for $\text{C}_{154}\text{H}_{176}\text{O}_{26}\text{Na}$ 2465.28, found 2465.40 $[\text{M}+\text{Na}]^+$.

Stability of **4**⊖1,4-(MeO)₂C₆H₄. A solution of 3 mg carceplex **4**⊖1,4-(MeO)₂C₆H₄ in 1 ml of CDCl_3 at 25 °C was monitored by ^1H NMR for 4 weeks, and no change was observed in the spectrum.

Decomplexation of $4\text{O}1,4\text{-(MeO)}_2\text{C}_6\text{H}_4$. A solution of 3 mg carceplex $4\text{O}1,4\text{-(MeO)}_2\text{C}_6\text{H}_4$ in 1 ml of CDCl_3 at 25 °C was irradiated at 254 nm for 1 h. The decomplexation was monitored by following the decrease of the intensity of the singlet at -0.37 ppm and the reappearance of the anthracene peaks from 7.20-8.20 ppm in the ^1H NMR spectrum.

1.5 Conclusion

In summary, a new reversible photoswitchable gated hemicarcerand containing two anthracene groups was designed and synthesized. Photochemical properties of this system were studied by ^1H NMR and fluorescence spectroscopy. The photoswitchable cycle between the open (hemicarcerand) and closed (carcerand) states of the host is well controlled by radiation of different wavelengths, and controlled encapsulation and release of the guest molecules such as 1,4-dimethoxybenzene was observed. We are currently working on enlarging the cavity size of the host as well as increasing the water solubility of the host.

1.6 References

1. (a) Cram, D. J.; Karbach, S.; Kim, Y. H.; Baczynskyj, L.; Kalleymeyn, G. W. *J. Am. Chem. Soc.* **1985**, *107*, 2575-2576. (b) Cram, D. J.; Cram, J. M. In *Container Molecules and Their Guests*; Stoddard, J. F. The Royal Society of Chemistry: Cambridge, **1994**, 131-216.
2. Singh, H.; Warmuth, R. *Tetrahedron*. **2002**, *58*, 1257-1264.
3. (a) Nakamura, K.; Houk, K. N. *J. Am. Chem. Soc.* **1995**, *117*, 1853- 1854. (b) Houk, K. N.; Nakamura, K.; Sheu, C.; Keating, A. E. *Science* **1996**, *273*, 627-629.
4. Moran, J. R.; Karbach, S.; Cram, D. J. *J. Am. Chem. Soc.* **1982**, *104*, 5826-5828.
5. Helgeson, R. C.; Hayden, A. E.; Houk, K. N. *J. Org. Chem.* **2010**, *75*, 570-575.
6. Gottschalk, T.; Jaun, B.; Diederich, F. *Angew. Chem. Int. Ed.* **2007**, *46*, 254-264.
7. Berryman, O. B.; Dube, H.; Rebek, J. Jr. *Isr. J. Chem.* **2011**, *51*, 700-709.
8. (a) Heinz, T.; Rudkevich, D.; Rebek, J. Jr. *Nature* **1998**, *394*, 764-766. (b) Dube, H.; Ajami, D.; Rebek, J. Jr. *Angew. Chem. Int. Ed.* **2010**, *49*, 3192-3195. (c) Dube, H.; Ams, M. R.; Rebek, J. Jr. *J. Am. Chem. Soc.* **2010**, *132*, 9984-9985. (d) Berryman, O. B.; Sather, A. C.; Rebek, J. Jr. *Chem. Commun.* **2011**, *47*, 656-658.
9. (a) Schäfer, C.; Rozhenko, A.; Mattay, J. *Photochem. Photobiol. Sci.* **2009**, *8*, 1187-1194. (b) Schäfer, C.; Mattay, J. *Photochem. Photobiol. Sci.* **2004**, *3*, 331-333. (c) Bringmann, S.; Brodbeck, R.; Hartmann, R.; Schafer, C.; Mattay, J. *Org. Biomol. Chem.* **2011**, *9*, 7491-7499.
10. Piatnitski, E. L.; Deshayes, K. O. *Angew. Chem., Int. Ed.* **1998**, *37*, 970-972.
11. Yoon, J.; Sheu, C.; Houk, K. N.; Knobler, C. B.; Cram, D. J. *J. Org. Chem.* **1996**, *61*, 9323-9339.
12. The reversible intramolecular photodimerization of naphthalene units has been studied extensively by Chandross et al. See, for example, Chandross, E. A.; Dempster, C. J. *J. Am. Chem. Soc.* **1970**, *92*, 703-704.
13. For photodimerization of anthracene units, see, for example, Laurent, H. B.; Castellan, A.; Desvergne, J.-P.; Lapouyade, R. *Chem. Soc. Rev.* **2000**, *29*, 43-55.
14. Our calculations indicate that two chloroforms readily occupy the open hemicarcerand, but that the diphenyl ether can only partially enter the cavity. Also mentioned in ref 11, Ph₂O was used as solvent because its molecular

volume is too large to occupy the interiors of hosts with tetramethylene bridges.

15. Previous similar examples by Cram in ref 11 show that the tetramethylene bridge hemicarceplex has a half life larger than 336 h.
16. This guest was able to form a hemicarceplex with a host with larger cavity. See, Yoon, J.; Cram, D. J. *Chem. Commun.* **1997**, 497-498.

Chapter 2: Steric Control of α - and β -Alkylation of Azulenone Intermediates in a Guanacastepene A Synthesis

2.1 Abstract

The origins of different stereoselectivities observed experimentally in the alkylations of azulenone precursors in the guanacastepene **A** synthesis have been determined through density functional theory investigations. The optimized transition structures of methylation of two different guanacastepene **A** precursors show that steric effects, rather than torsional factors that often determine such stereoselectivities, dictate the preferred products observed.

2.2 Introduction

The synthesis of stereochemically complex molecules requires control of introduction of new stereogenic centers. The use of asymmetric catalysts to control the stereoselectivity of alkylations has been of much contemporary interest in this regard.¹ Although catalyst control can give high stereoselectivity, the modification of substrates to control stereoselective alkylations is also a venerable and useful strategy in synthesis. Understanding and predicting substrate controlled stereoselective synthesis remains a challenging problem.² Stereoselective alkylations have been investigated by computational methods in a few cases,³ and the role of torsional effects has been emphasized. Torsional effects control the trajectories of attack of electrophiles on

electron-rich alkenes,⁴ just as manifested for nucleophilic attack on carbonyls in the Felkin-Anh-Dunitz-Bürgi model.⁵ Here we report a computational study that reveals that steric effects can sometimes override torsional effects, leading to different stereoselectivities in α - or β -alkylations of azulenone precursors in the guanacastepene **A** synthesis.

In recent attempts to complete the Guanacastepene **A** total synthesis, opposite stereoselectivities were observed in the methylations of two rather similar azulenone intermediates (Figure 2.1).⁶ Enolate **A** gives the β -methylation product in 72% yield with 9:1 diastereomeric ratio. Enolate **B**, which has an additional double bond at the ring junction, affords the α -methylation product in 98% yield, exclusively. The methylation stereoselectivity observed for enolate **B** is consistent with the experimental results reported by Danishefsky and Mehta for a related intermediate.⁷ In order to determine the origins of these different stereoselectivities, we explored these reactions computationally.

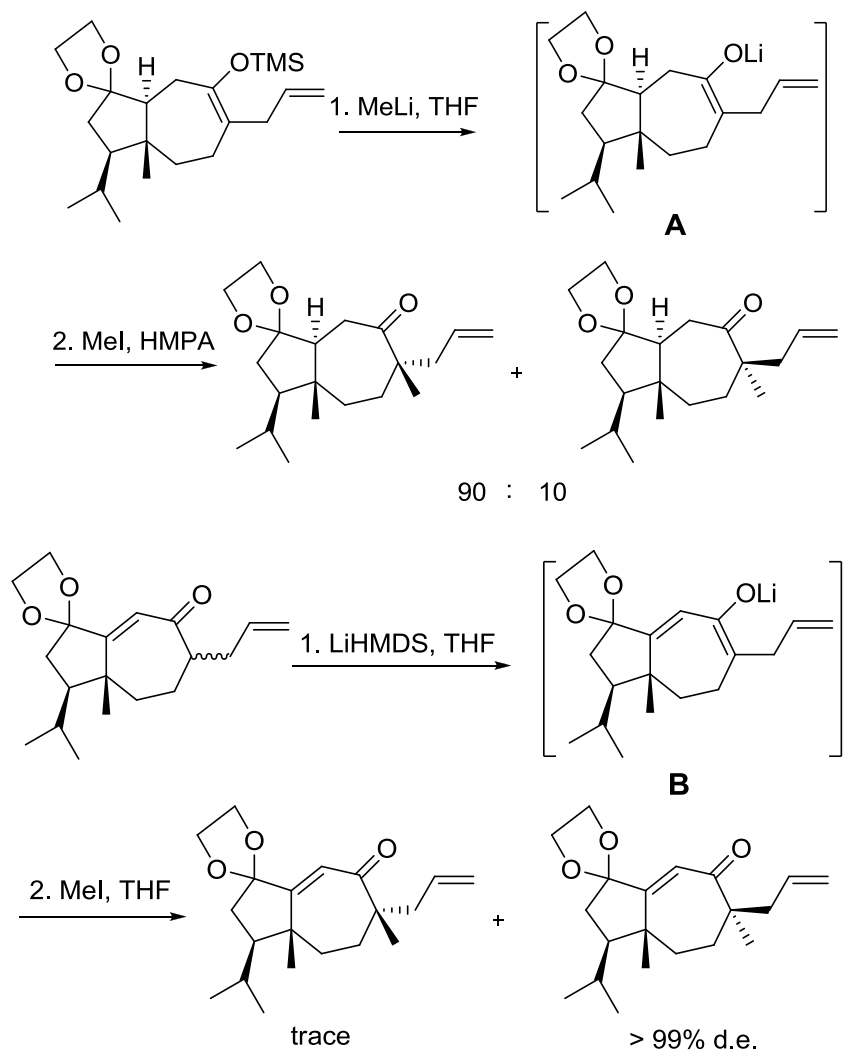


Figure 2.1. Routes for the alkylation of two different azulene intermediates.

2.3 Results and Discussion

The energy minimized geometry of enolate **A** shown in Figure 2.2, was obtained with the B3LYP/6-31G* method^{8, 9}. The cycloheptenolate ring adopts a chair conformation in the substrate and the allyl group is rotated down with respect to the ring. The allyl group can adopt a variety of other conformations, and the other three minimized

conformers are 0.5, 2.4, 2.5 kcal/mol higher in energy, respectively. The cycloheptenolate ring can also adopt a boat conformation in enolate **A**, however, the most stable boat-like conformation is less stable than the chair-like one by 1.6 kcal/mol. As shown in the Newman projection of enolate **A**, there is no difference between torsional effects for attack on the α or β face.

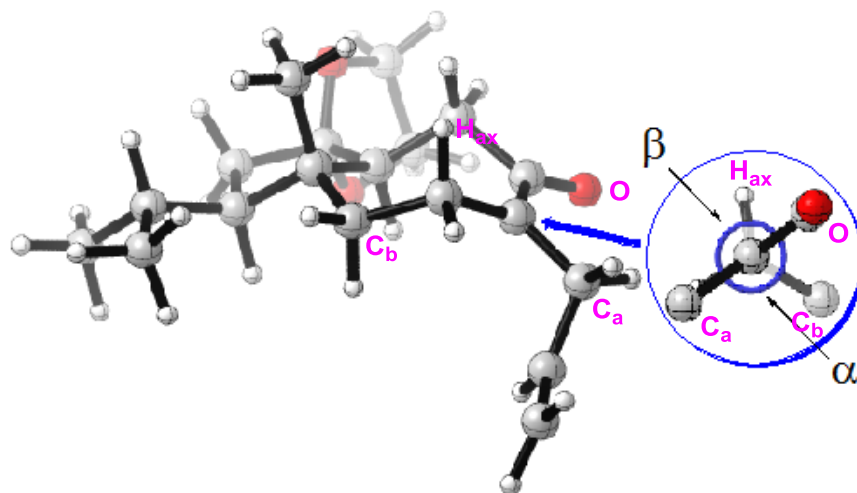


Figure 2.2. The lowest energy chair-like conformation of enolate **A**. A Newman projection viewed from the direction indicated by the blue arrow is also shown.

The alkylation transition states for the reaction of methyl bromide with enolate **A** were investigated next. Both chair-like conformation and boat-like conformation of enolate **A** were considered in the transition states, and all different conformers with respect to the rotation of allyl and vinyl groups were explored. For the alkylation on chair-like enolate **A**, six different β -attack transition state conformers were located with relative $\Delta\Delta G^\ddagger$ values of 0.0, 2.6, 2.7, 3.9, 4.4, 5.6 kcal/mol, respectively. Six TS structures with $\Delta\Delta G^\ddagger$ values of 1.8, 4.2, 4.3, 5.8, 6.1, 7.5 kcal/mol, were found for the α -attack. The boat-like enolate **A** was also considered for the methylation transition states.

The α -attack alkylation gave six transition state conformers with relative $\Delta\Delta G^\ddagger$ values of 2.4, 3.8, 4.3, 5.6, 5.7, 5.8 kcal/mol, respectively. The β -attack transition state structures also gave six different conformers whose $\Delta\Delta G^\ddagger$ are 4.1, 5.7, 6.9, 8.1, 8.3, 8.6 kcal/mol, respectively.

From the energetics of the different transition state conformers, the most stable conformers of the transition states were located to be α/β -alkylation on chair-like enolate **A**. They are shown in Figure 2.3. The best α -methylation transition structure of enolate **A** (**1 α**) is 1.8 kcal/mol higher energy than β -methylation transition state (**1 β**). This value was lowered to 1.1 kcal/mol by including solvation energies with the CPCM model¹⁰ for methanol (The solvent used experimentally was HMPA. No solvent model is available for HMPA, but methanol has a very similar dielectric constant to HMPA) (Table 2.1). This value is consistent with the 1:9 α : β product ratios observed experimentally. Careful inspection of the two transition states suggests that the α -methylation transition state has no eclipsing (**1 α'**), but there are significant repulsions between a methyl bromide H and two homoallylic Hs. They are separated by only 2.28 Å and 2.31 Å, less than the sum of their van der Waals radii (2.4 Å). However, there is only one H-H steric interaction (separated by 2.37 Å) in the β -attack transition structure, although there is some eclipsing between the forming bond and the axial CH bond (**1 β'**).

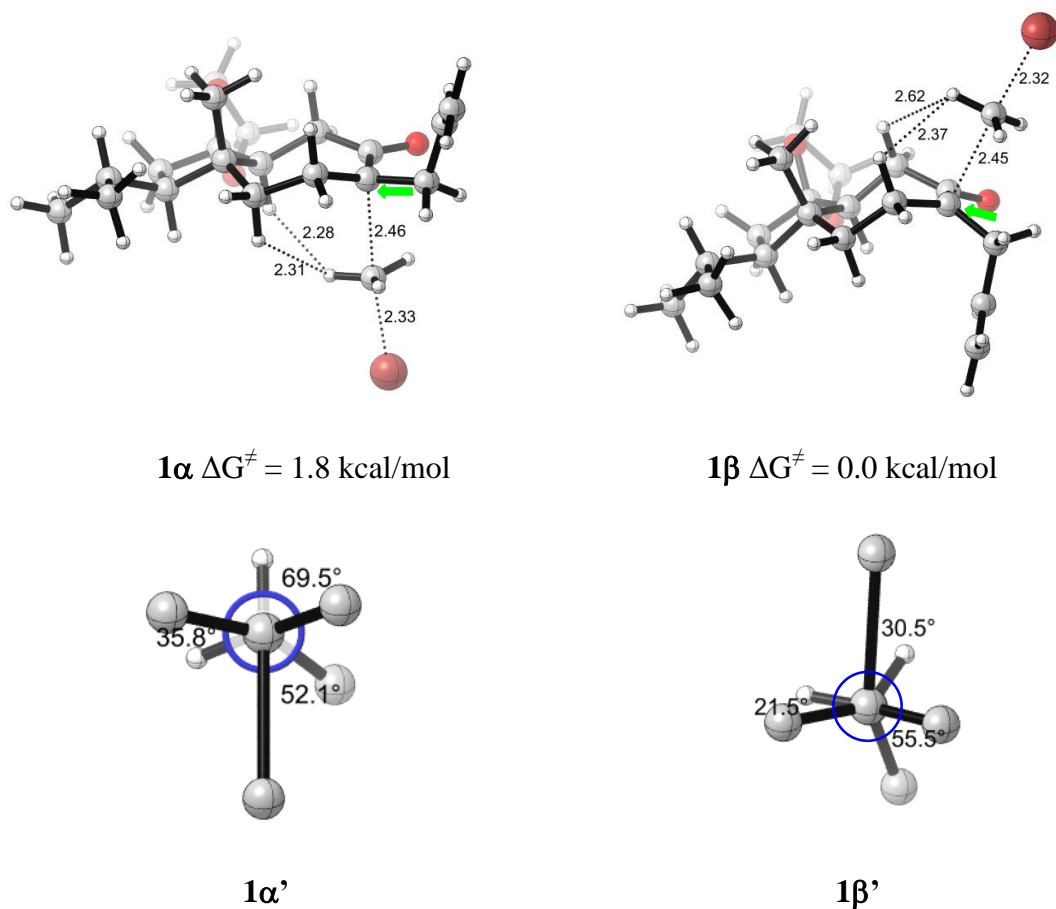


Figure 2.3. Transition structures for the α - and β -attack of methyl bromide on enolate **A**. Newman projections, **1α'** or **1β'**, are viewed from the directions indicated by the green arrows.

Table 2.1. Summary of the free energies of **1α**, **1β**, **2α**, **2β**.

	G_{298} (gas)	G_{298} (solvent) ^a
ΔG^\ddagger (1α-1β)	1.8 kcal/mol	1.1 kcal/mol
ΔG^\ddagger (2β-2α)	5.2 kcal/mol	4.6 kcal/mol

^a Solvent correction used the CPCM polarizable conductor calculation model as implemented in Gaussian 03. For **1α**, **1β**, methanol was specified as the solvent ($\epsilon_{\text{MeOH}} = 32.6$, while the experimental solvent is $\epsilon_{\text{HMPA}} = 30$). For **2α**, **2β**, THF was specified as the solvent.

Although torsional control of electrophilic or nucleophilic attack has been observed in a wide variety of situations,⁴ it seems that the steric factors override the torsional effects in the stereoselective alkylations studied here. The two transition states are both staggered to a similar extent, but steric effects differentiate α and β -attack.

The geometry of enolate **B** was also optimized and is shown in Figure 2.4. In contrast with enolate **A**, the cycloheptadienolate ring adopts the twist-boat conformation in substrate **B**, and the allyl group is rotated up with respect to the ring. This conformer has literature precedent.¹¹ The energetic favorable twist-boat conformation of enolate **B** is more stable than the chair conformation, due to the constraints of the additional double bond at the ring junction.^{11b} The other three minimized conformers with respect to the rotation of allyl groups are 0.7, 1.8, 2.3 kcal/mol higher in energy, respectively. As shown in the Newman projection of enolate **B**, there is no torsional difference for α or β attack.

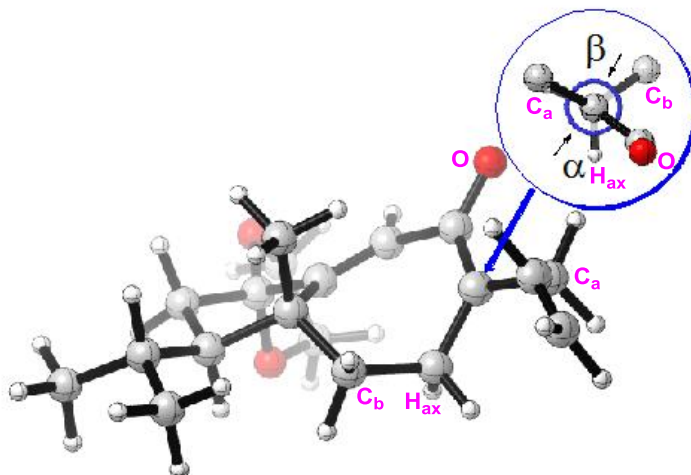


Figure 2.4. The lowest energy conformation of enolate **B**. The Newman projection is viewed from the direction indicated by the blue arrow.

Transition states of both α - and β -alkylation with methyl bromide on enolate **B** were then located, and all different rotamers with respect to the rotation of allyl and vinyl groups were considered. Six different α -alkylation transition state conformers were obtained with relative $\Delta\Delta G^\ddagger$ values of 0.0, 1.3, 1.5, 2.5, 2.7, 4.1 kcal/mol, respectively. For the β -alkylation transition states, another six different conformers were obtained whose $\Delta\Delta G^\ddagger$ are 5.2, 6.8, 7.6, 8.8, 9.1, 9.9 kcal/mol with respect to the lowest energy α -alkylation transition state. The most stable transition state conformers are shown in Figure 2.5. The α -methylation transition state (**2 α**) is 5.2 kcal/mol more stable than the corresponding β -methylation transition state (**2 β**). This value is 4.6 kcal/mol when including solvation energies (Table 2.1, THF, CPCM model). This is in an excellent agreement with the experiment observation that methylation of enolate **B** takes place exclusively from the α -face. The large energy difference between the two transition structures is also due to steric factors rather than torsional effects. Both transition states have some torsional strain, shown in **2 α '**, **2 β '**. However, in contrast to the α -alkylation transition structure where only one H-H steric interaction exists (separated by 2.31 Å), β -alkylation process suffers significant steric repulsions between H on methyl bromide and two Hs on the substrate separated by 2.08 Å and 2.26 Å, respectively.

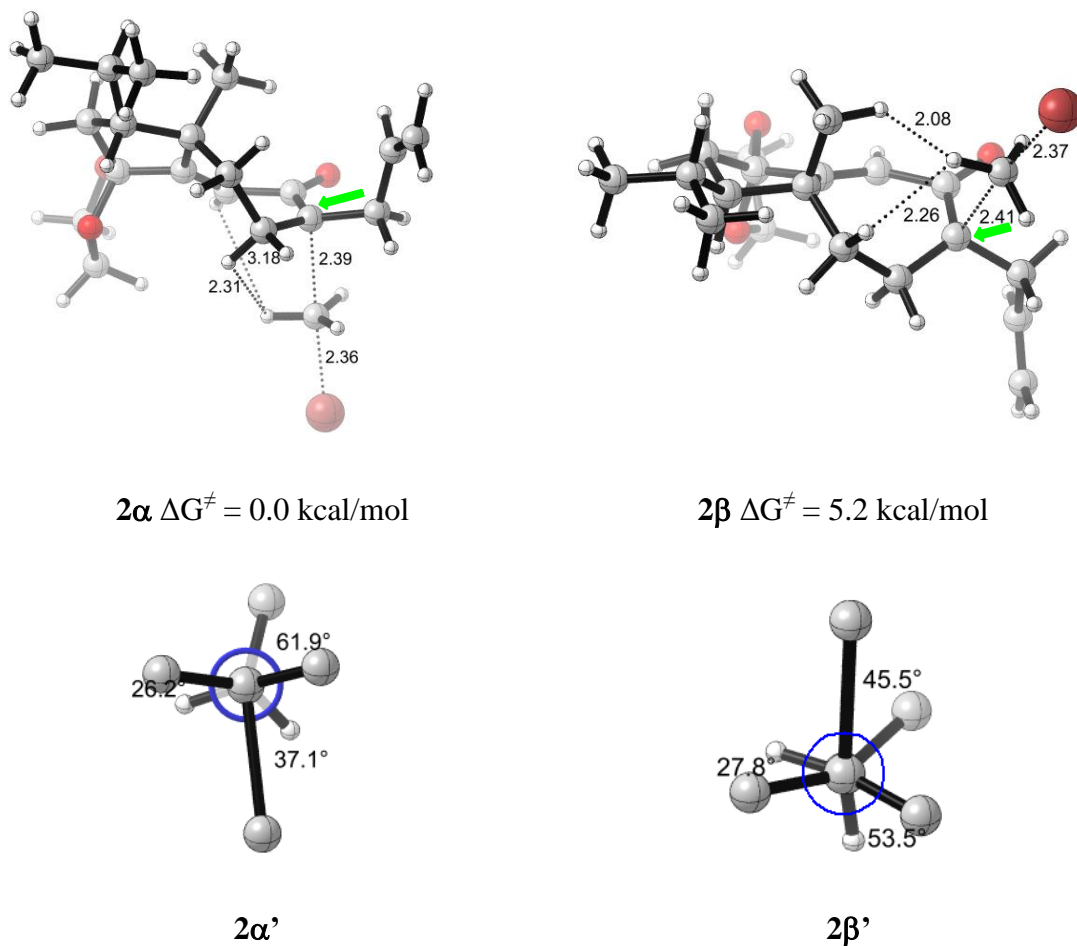


Figure 2.5. Transition structures for the α - and β -attack of methyl bromide on enolate **B**. Newman projections, $2\alpha'$ or $2\beta'$, are viewed from the directions indicated by the green arrows.

In fact, the qualitative origins of alkylation stereoselectivities can be identified from the geometry of the starting substrate (Figure 2.6).

As can be seen by inspection of the energetically favorable chair conformation of enolate **A** (**3A**), the α -face of the cycloheptene ring is seriously blocked. Approach of the electrophile (CH_3I) is clearly preferred at the β -face for enolate **A** which is consistent with the result obtained by TS exploration. With respect to enolate **B**, however, by

adopting the twist-boat conformation, the left part of the cycloheptadienolate ring flips up (**3B**), which results in blocking the β -face toward attack, and favoring the α -attack of the electrophile. The analysis of the geometries of the substrates again confirms that the stereoselectivities of alkylation result from steric effects. The allyl groups in **3A** and **3B** can adopt less hindered conformations, but the more rigid bicyclic groups dictate β and α attack, respectively.

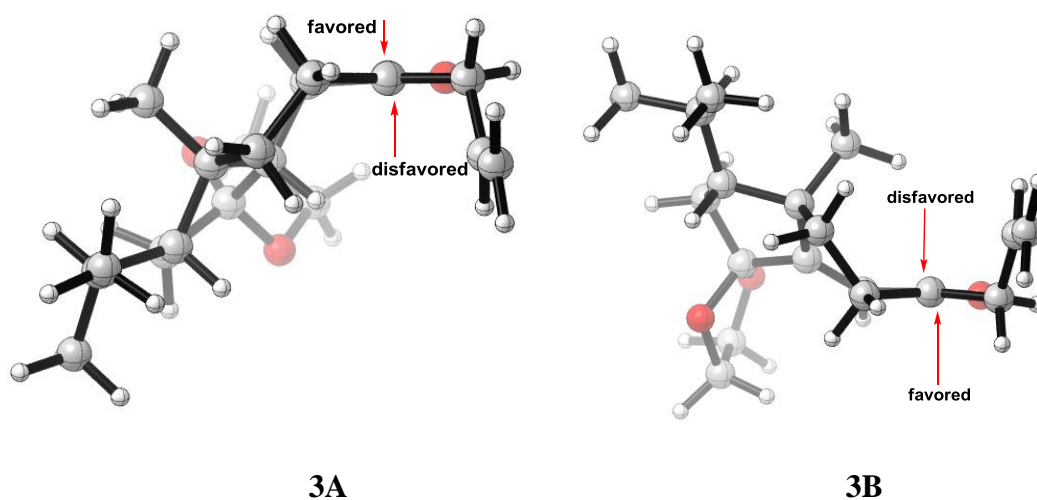


Figure 2.6. Optimized model reactants **A** and **B** from the side view.

2.4 Conclusion

In summary, the diastereoselectivities observed experimentally in azulene enolates alkylation originate from the steric interactions between the alkylation reagent and the substrate. This investigation provides examples of steric effects controlling stereoselectivities with no torsional differentiation, and provides guidance for the control of stereoselectivities by conformation manipulation of the substrates.

2.5 References

- (a) Nicola M. H.; Jeffrey A. A.; Amir H. H. *J. Am. Chem. Soc.* **1997**, *119*, 6205-6206. (b) He X. X.; Lian S. Z.; Wei W. *J. Am. Chem. Soc.* **2007**, *129*, 10886-10894. (c) Denise A.; Jonathan A. *J. Am. Chem. Soc.* **2006**, *128*, 5604-5605. (d) Cristina C.; Gianni P.; Emanuela V. *J. Org. Chem.* **2003**, *68*, 1200-1206. (e) Ivan L. L.; Keunho K.; Jin K. C. *J. Am. Chem. Soc.* **2008**, *130*, 15997-16002.
- (a) Morris, W. J.; Shair, D. S. *Org. Lett.*, **2009**, *11*, 9-12. (b) Takashi E.; Toru E.; Kazutaka T.; Makoto S. *J. Org. Chem.* **2006**, *71*, 8559-8564.
- (a) Soteras, I.; Lozano, O.; Escolano, C.; Orozco, M.; Amat, M.; Bosch, J.; Luque F. J. *J. Org. Chem.* **2008**, *73*, 7756-7763. (b) Ando, K.; Green N.; Li, Y.; Houk, K. N. *J. Am. Chem. Soc.* **1999**, *121*, 5334-5335. (c) Ikuta Y.; Tomoda, S. *Org. Lett.* **2004**, *6*, 189-192. (d) Wu, Y.-D.; Houk, K. N.; Trost, B. M. *J. Am. Chem. Soc.* **1987**, *109*, 5560-5561. (e) Mukherjee, D.; Wu, Y.-D.; Fronczek, F. R.; Houk, K. N. *J. Am. Chem. Soc.* **1988**, *110*, 3328-3330. (f) Iafe, R. G.; Houk, K. N. *Org. Lett.* **2006**, *8*, 3469-3472. (g) Jimenez-Oses, G.; Aydillo, C.; Busto, J. H.; Zurbano, M. M.; Peregrina, J. M.; Avenoza, A. *J. Org. Chem.* **2007**, *72*, 5399-5402. (h) Ando, K. *J. Am. Chem. Soc.* **2005**, *127*, 3964-3972. (i) Soteras, I.; Lozano, O.; Gomez-Esque, A.; Escolano, C.; Orozco, M.; Amat, M.; Bosch, J.; Luque, F. J. *J. Am. Chem. Soc.* **2006**, *128*, 6581-6588. (j) Aydillo, C.; Jimenez-Oses, G.; Busto, J. H.; Zurbano, M. M.; Peregrina, J. M.; Avenoza, A. *Chem. Eur. J.* **2007**, *13*, 4840-4848. (k) Kozłowski, M. C.; Dixon, S. L.; Panda, M.; Lauri, G. *J. Am. Chem. Soc.*, **2003**, *125*, 6614-6615.
- (a) Caramella, P.; Rondan, N. G.; Paddon, M. N.; Houk, K. N. *J. Am. Chem. Soc.* **1981**, *103*, 2438-2440. (b) Rondan N. G.; Paddon, M. N.; Caramella, P.; Mareda, J.; Mueller, P. H.; Houk, K. N. *J. Am. Chem. Soc.* **1982**, *104*, 4974-4976. (c) Paddon, M. N.; Rondan, M. N.; Houk, K. N. *J. Am. Chem. Soc.* **1982**, *104*, 7162-7166. (d) Lucero, M. J.; Houk, K. N. *J. Org. Chem.* **1998**, *63*, 6973-6977. (e) Cheong, P. H.; Yun, H.; Danishefsky, S. J.; Houk, K. N. *Org. Lett.* **2006**, *8*, 1513-1516. (f) Martinelli, M. J.; Peterson, B. C.; Khau, V. V.; Hutchinson, D. R.; Leanna, M. R.; Audia, J. E.; Droste, J. J.; Wu, Y.-D.; Houk, K. N. *J. Org. Chem.* **1994**, *59*, 2204-2210. (g) Lucero, M. J.; Houk, K. N. *J. Org. Chem.* **1998**, *63*, 6973-6977. (h) Houk, K. N.; Paddon-Row, M. N.; Rondan, N. G.; Wu, Y.-D.; Brown, F. K.; Spellmeyer, D. C.; Metz, J. T.; Li, Y.; Loncharich, R. J. *Science* **1986**, *231*, 1108-1117.
- Anh, N. T. *Top. Curr. Chem.* **1980**, *88*, 146-162.
- Michalak, K.; Michalak, M.; Wicha, J. Manuscript in preparation.

7. (a) Mandal, M.; Yun, H. D.; Dudley, G. B.; Lin, S. N.; Tan, D. S.; Danishefsky, S. J. *J. Org. Chem.* **2005**, *70*, 10619-10637. (b) Mehta, G.; Umarye, J. D.; Srinivas, K. *Tetrahedron Lett.* **2003**, *44*, 4233-4237.
8. Becke, A. D. *J. Chem. Phys.* **1993**, *98*, 5648-5652.
9. Calculations were performed in Gaussian 03, M. J. Frisch, *et al.* Gaussian Inc., Pittsburgh, PA, 2004.
10. (a) Barone, V.; Cossi, M. *J. Phys. Chem. A* **1998**, *102*, 1995-2001. (b) Cossi, M.; Rega, N.; Scalmani, G.; Barone, V. *J. Comp. Chem.* **2003**, *24*, 669-681.
11. (a) Crews, P. *Chem Commun.* **1971**, *11*, 583-584. (b) Anthony, J. P.; Harjinder, S. B. *Tetrahedron Lett.* **1986**, *27*, 287-290.

Chapter 3. Computational Elucidation of the Origins of Reactivity and Selectivity in Non-Aldol Aldol Rearrangements of Cyclic Epoxides

3.1 Abstract

The non-aldol aldol reaction of the isomeric epoxy silyl ethers is controlled by the conformation of the transition states leading to an internal hydride shift. One isomer rearranges to the β -silyloxy ketone whereas the other isomer gives a β -elimination product. Theoretical calculations show that the substrates with substituents that favor the formation of the chair-like transition state rearrange normally while those that do not undergo elimination instead.

3.2 Introduction

Lewis acid induced rearrangements are useful synthetic tools that provide access to unique and highly functionalized systems. The non-aldol aldol rearrangement is a semi-pinacol rearrangement of epoxy alcohols that generates silyl-protected aldol products in high yields.^{1,2} Reactions of optically active epoxy alcohols, **2**, derived from the Sharpless asymmetric epoxidations³ of the allyl alcohols, **1**, with a silyl triflate induce a 1,2- hydride shift followed by formation of the silyl protected aldols, **3**, in excellent yields and enantioselectivities (Figure 3.1). The process has been implemented in the total syntheses of several polyketide natural products, including auriopyrones A and B.⁴

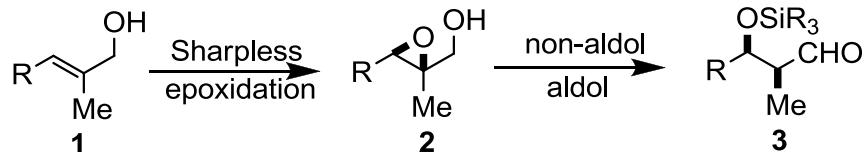


Figure 3.1. Non-aldol aldol rearrangement.

Recently, the non-aldol aldol rearrangement was extended to cyclic systems to prepare silyloxycycloalkanones from the corresponding 2,3-epoxy-cycloalkanols.⁵

This strategy is expected to succeed as long as an antiperiplanar CH is available to migrate upon epoxide opening in such conformationally constrained ring systems. However, in the course of our application of this cyclic non-aldol aldol rearrangement to the total synthesis of *N*-methylwelwitindolinone C isothiocyanate,⁶ we have found that the facility of the reaction is a sensitive function of substitution, and that the conformation of the transition states is different from that of substrates.⁷ We provide computational evidence that stereoelectronic effects and a combination of ground state destabilization and transition state stabilization controls the non-aldol processes in these systems and competition between rearrangement and elimination reactions.

3.3 Results and Discussion

As shown in Figure 3.2, one of the two diastereomers of a 6-methyl-2,3-epoxycyclohexyl silyl ether, **4a**, leads to the non-aldol aldol rearrangement in good yield, while the other diastereomer, **4b**, undergoes mostly elimination and

decomposition. This result is surprising, since, as shown in Figure 3.2, the requisite antiperiplanar arrangement of the migrating hydrogen is apparent in both reactants. The axial methyl in the preferred conformer of **4a** might have been expected to disfavor the reaction. In fact, the opposite is true.

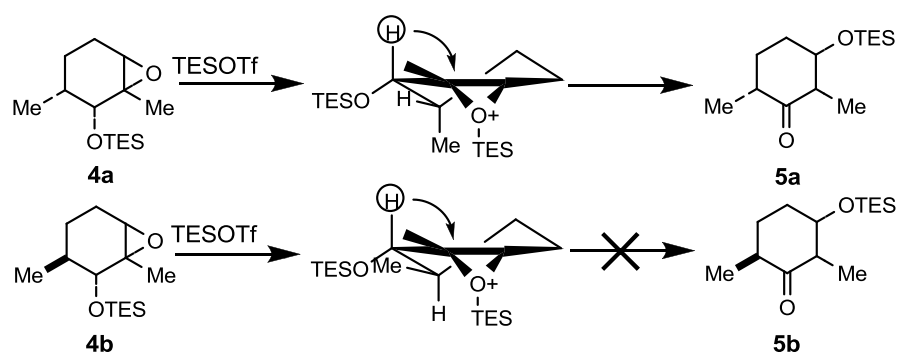


Figure 3.2. Non-aldol aldol rearrangement of **4a** and **4b**.

Reaction of epoxide **4a** with TESOTf and Hunig's base gave the non-aldol aldol product **5a**.⁷ Surprisingly, however, treatment of the 6-methyl diastereomer **4b** did not afford the expected **5b**, despite the hydride positioned antiperiplanar to the epoxide at 161° in the crystal structure of the alcohol **5b**. Rather, the exocyclic olefin **6b**, the product of elimination was isolated (Figure 3.3).⁷

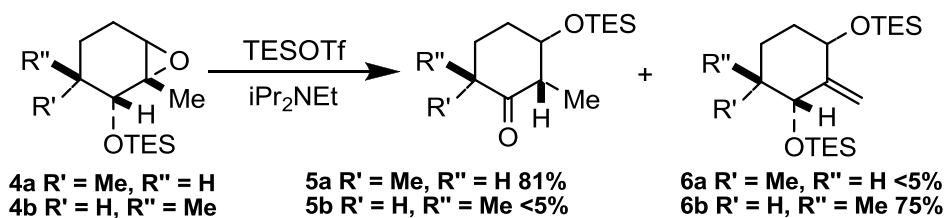


Figure 3.3. Experimental results of non-aldol aldol rearrangement of **4a** and **4b**.

Computational investigations provide the explanation of these perplexing results.⁸ B3LYP/6-31G(d) calculations on the silylated epoxides and transition states for the rearrangements were carried out for each case. The full systems were computed, except that a TMS was substituted for each TES group.

The computed structures of silylated epoxides are shown in Figures 3.4 and 3.5, and the computed relative energies are shown below each structure. The full energetics for these reactions are given in the supporting information. Each stereoisomer involves two possible half-chair conformers, **A** \rightleftharpoons **B** (Figure 3.4) and **A'** \rightleftharpoons **B'** (Figure 3.5) that are in rapid equilibrium. The ring opening of the epoxide is accompanied by a hydride shift. As shown in Figure 3.4, **4a** has two possible half-chair conformers **A** and **B**. **A** leads to the half-boat TS **C** that leads to the boat conformer of the product, while conformer **B** proceeds via the half-chair TS **D** to give the chair conformer of the product. The preferred rearrangement pathway involves conformation flip of **A** to **B** and then to transition state **D** with the overall activation energy of 5.2 kcal/mol, via a Curtin-Hammett process. Transition state **C**, and the boat conformer of the product are both disfavored due to torsional strain; both experience eclipsing interactions. By contrast, the half chair **D** and corresponding products are more nearly staggered.

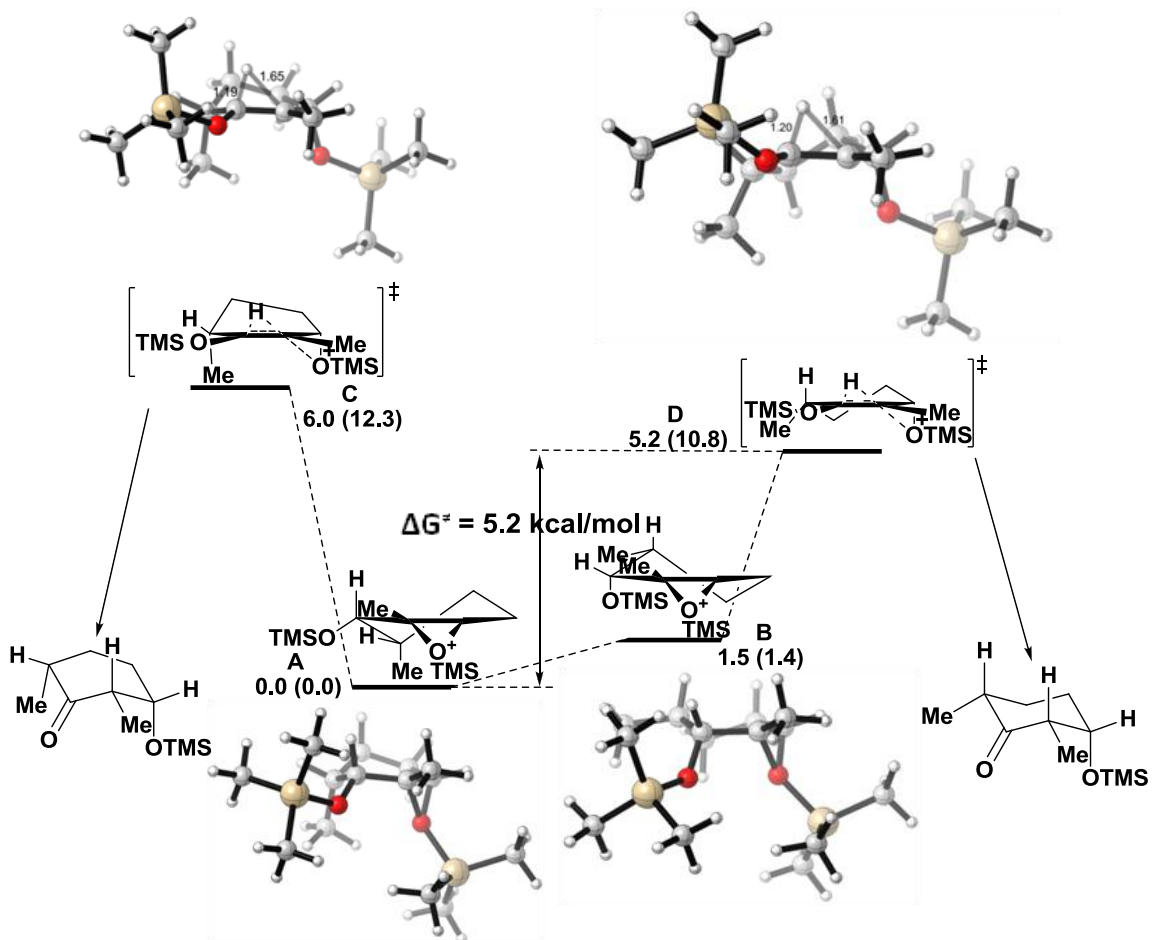


Figure 3.4. B3LYP optimized geometries of **4a** (**A** and **B**) and transition structures (**C** and **D**) for the non-aldol aldol rearrangement. Values below each structure are relative energies in kcal/mol. Values enclosed in parentheses are relative single-point energies calculated by M06-2X method in kcal/mol.

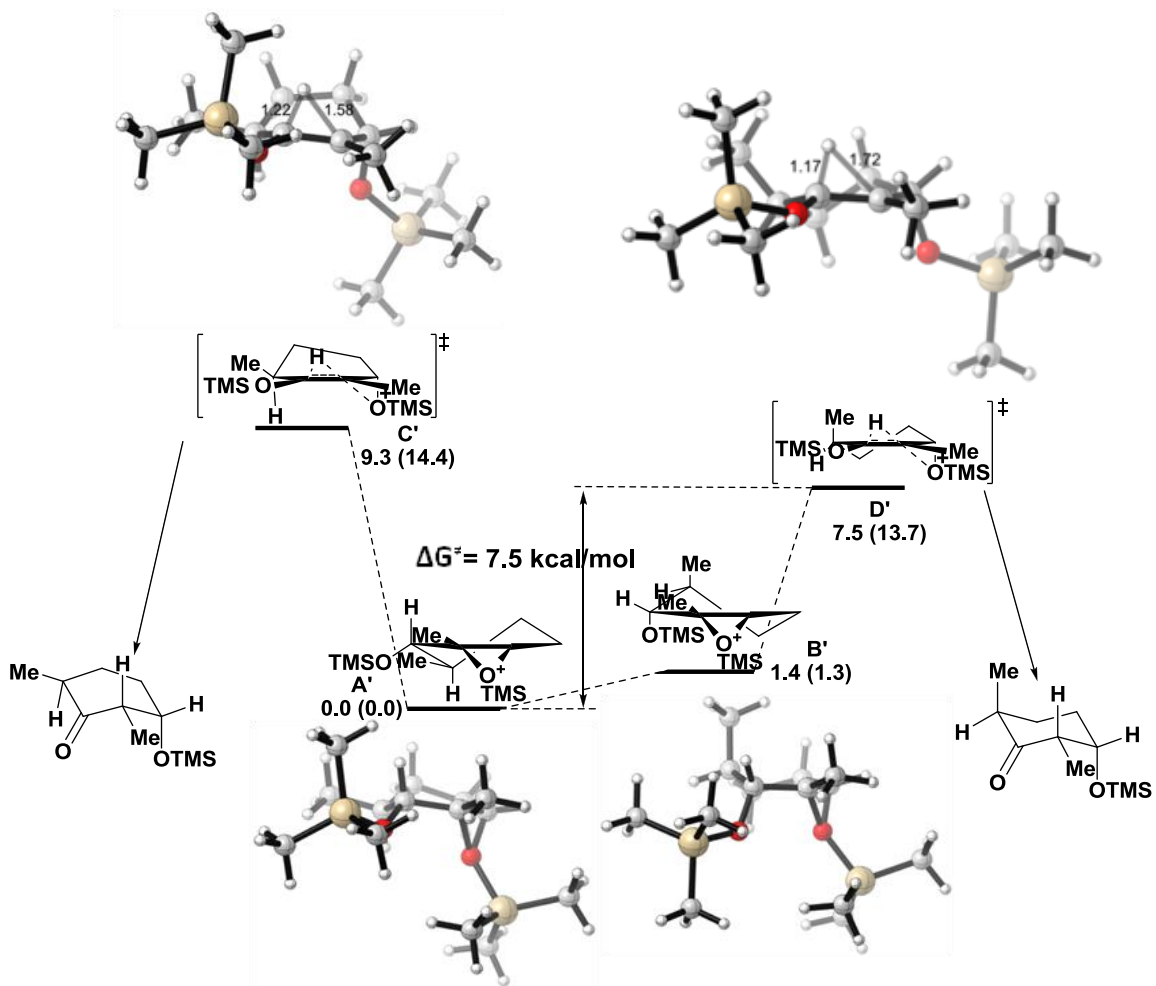


Figure 3.5. B3LYP optimized geometries of **4b** (A' and B') and transition structures (C' and D') for the non-aldol aldol rearrangement. Values below each structure are relative energies in kcal/mol. Values enclosed in parentheses are relative single-point energies calculated by M06-2X method in kcal/mol. A' is 1.4 kcal/mol more stable than A (Figure 3.4) or 0.9 kcal/mol at the M06-2X level.

In Figure 3.5, the structures for the isomeric reactant, **4b**, are shown. The equatorial methyl of **A'** causes the silylated epoxide, **A'**, to be 1.4 kcal/mol lower in energy than **A**. The preferred transition state **D** with an equatorial methyl group (Figure 3.4) is more stable than **D'** formed by **4b** by 0.9 kcal/mol (Figure 3.5). Consequently, the rearrangement of the cis isomer **4a** to give the non-aldol aldol product has an activation energy of only 5.2 kcal/mol, while the trans isomer **4b** has a higher activation energy of 7.5 kcal/mol (Figure 3.6). Compound **4b** will undergo the rearrangement almost 100 times more slowly than **4a**. Experimentally, **4b** gives the alternative intermolecular elimination product **6b**, rather than the non-aldol aldol product **5b**. Single-point calculations with M06-2X using B3LYP-optimized geometries leads to 5-6 kcal/mol higher activation energies, but energy difference calculated for **4a** and **4b** by M06-2X method is 2.9 kcal/mol, similar to the B3LYP result of 2.3 kcal/mol.

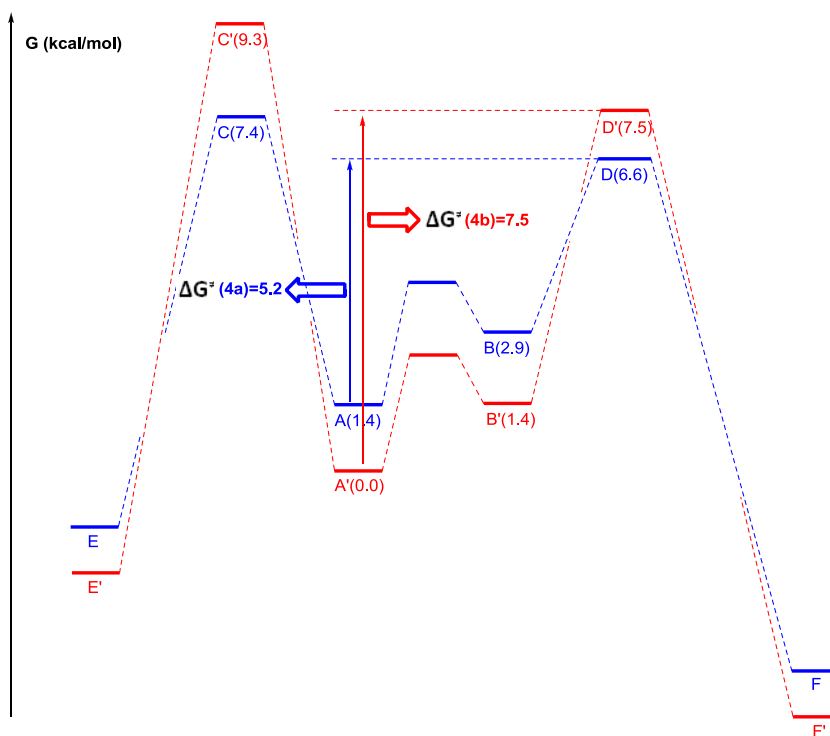


Figure 3.6. Energy profile for the non-aldol aldol pathways of **4a** and **4b**.

The exploration of these results is essentially the same as the Fürst-Plattner rule⁹ for nucleophilic ring-opening of epoxides. Torsional effects favor formation of the trans-diaxial product. In the case of **4a**, transition states **C** and **D** both lead to trans-diaxial epoxide opening, but **D** leads to the preferred chair product, while **C** leads to the twist boat product which is torsionally destabilized. With **4b**, the preference for **D'** over **C'** follows the same pattern.

In order to investigate the competing elimination reaction, trimethylamine was used instead of Hunig's base to model the reaction pathway. The most stable elimination transition states of the two diastereomers **4a** and **4b** are located (Figure 3.7) and the computed energetics for the elimination reactions are compared to the non-aldol aldol transition states (Figure 3.8, 3.9). The elimination barriers of 7.4 kcal/mol and 6.5 kcal/mol (13.6 and 12.5 kcal/mol by M06-2X) are similar and are in-between the non-aldol aldol barriers of **4a** and **4b**.

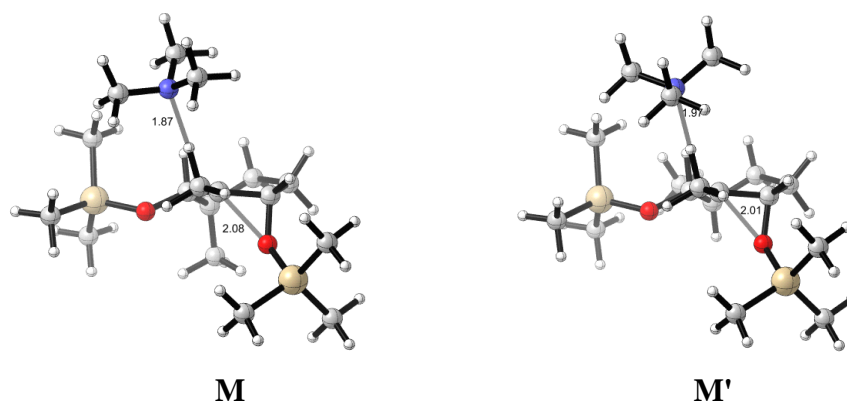


Figure 3.7. Transition structures for the elimination pathways of **4a** (**M**) and **4b** (**M'**).

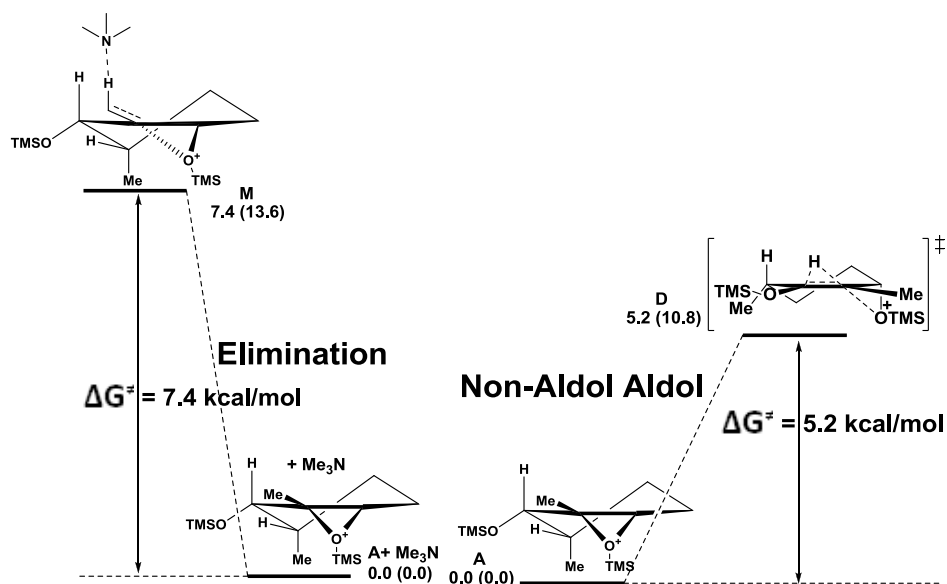


Figure 3.8. Energy profile for the non-aldol aldol rearrangement and elimination pathway of **4a**. Values below each structure are relative energies in kcal/mol. Values enclosed in parentheses are relative single-point energies calculated by M06-2X method in kcal/mol.

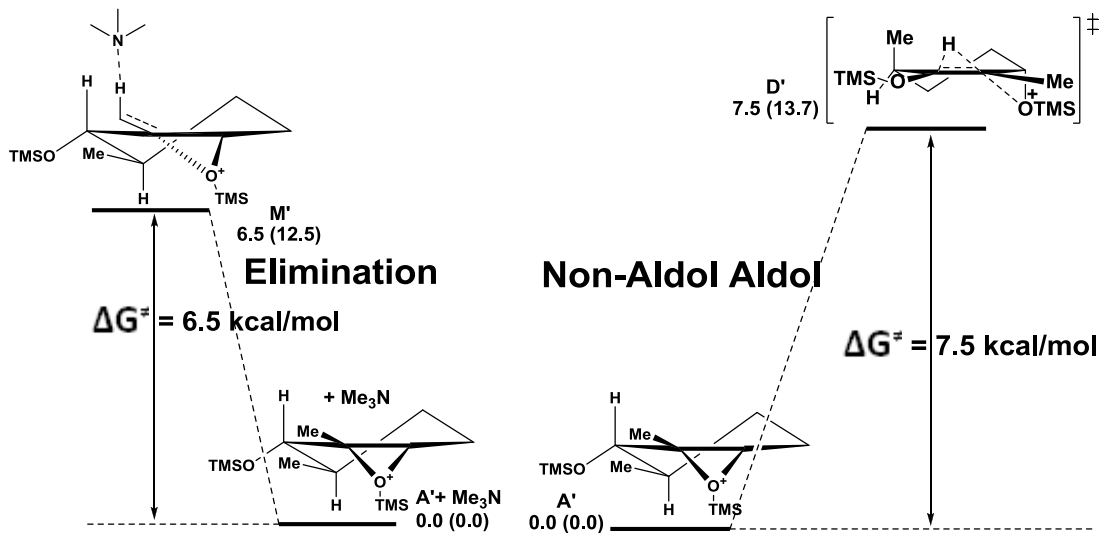


Figure 3.9. Energy profile for the non-aldol aldol rearrangement and elimination pathway of **4b**. Values below each structure are relative energies in kcal/mol. Values enclosed in parentheses are relative single-point energies calculated by M06-2X method in kcal/mol.

The stereoisomer **4a** has a higher activation energy (7.4 kcal/mol) for the elimination reaction than the barrier of the non-aldol aldol pathway (5.2 kcal/mol) (Figure 3.8). This is consistent with the experimental observation that **4a** will undergo the desired non-aldol aldol reaction instead of the elimination reaction. M06-2X results give a similar prediction, with the elimination barrier 2.8 kcal/mol above the non-aldol aldol barrier.

However, the elimination pathway of the isomeric reactant **4b**, which proceeds via TS **M'** to give the elimination product, has an activation energy of 6.5 kcal/mol, lower than for the non-aldol aldol pathway, which has a higher barrier of 7.5 kcal/mol (Figure 3.9). Again, M06-2X also predicts the elimination to be favored, by 1.2 kcal/mol.

The substituent effects on the migration of an alkyl group were also investigated. Treatment of epoxide **7a**¹⁰ with TESOTf afforded the expected rearranged product **8a** (Figure 3.10).⁷ However, exposure of the epoxide with the equatorial methyl group **7b** to TESOTf gave 1:1 mixture of the methyl migration product **8b** and the product of the ring contraction **9b**, via ring-carbon migration.⁷

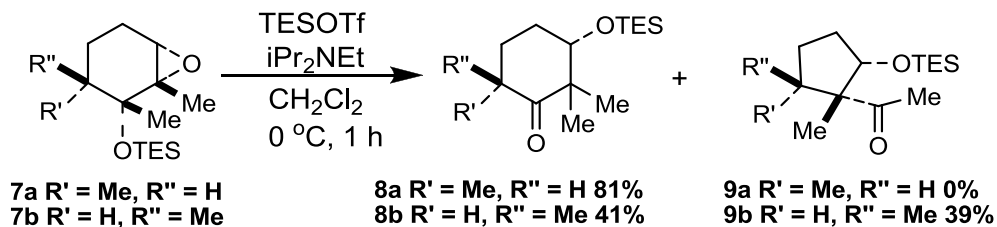


Figure 3.10. Experimental results of non-aldol aldol rearrangement of **7a** and **7b**.

As shown in Figure 3.11, the transition state model for the non-aldol aldol rearrangement of **7a** has an equatorial methyl group which is favored; whereas the TS model of **7b** which is disfavored has an axial methyl group in the half-chair structure.

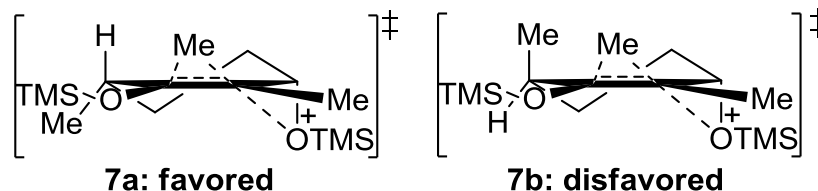


Figure 3.11. Half-chair transition state models for the non-aldol aldol rearrangement of **7a** and **7b**.

3.4 Conclusion

These findings confirm the hypothesis that diastereomeric 5- and 6-substituted 2,3-epoxycyclohexyl silyl ether substrates that can access the favored half-chair TS rearrange normally, while those which have disfavored axial substituents in the TS undergo other reaction processes instead. Further studies of this ‘remote control’ and application of these findings to the total synthesis of *N*-methylwelwitindolinones will be reported in due course.

3.5 References

1. For an excellent review of semi-pinacol rearrangements, see: Snape, T. J. *Chem. Soc. Rev.* **2007**, *36*, 1823-1842.
2. (a) Jung, M. E.; D'Amico, D. C. *J. Am. Chem. Soc.* **1993**, *115*, 12208-12209. (b) Jung, M. E.; D'Amico, D. C. *J. Am. Chem. Soc.* **1995**, *117*, 7379-7388. (c) Jung, M. E.; D'Amico, D. C. *J. Am. Chem. Soc.* **1997**, *119*, 12150-12158. (d) Jung, M. E.; Marquez, R. *Tetrahedron Lett.* **1999**, *40*, 3129-3132. (e) Jung, M. E.; Lee, W. S.; Sun, D. *Org. Lett.* **1999**, *1*, 307-309. (f) Jung, M. E.; Sun, D. *Tetrahedron Lett.* **1999**, *40*, 8343-8346. (g) Jung, M. E.; van den Heuvel, A. *Tetrahedron Lett.* **2002**, *43*, 8169-8172. (h) Jung, M. E.; Hoffmann, B.; Rausch, B.; Contreras, J.-M. *Org. Lett.* **2003**, *5*, 3159-3161. (i) Jung, M. E.; van den Heuvel, A.; Leach, A. G.; Houk, K. N. *Org. Lett.* **2003**, *5*, 3375-3378. (j) Jung, M. E.; van den Heuvel, A. *Org. Lett.* **2003**, *5*, 4705-4707.
3. (a) Katsuki, T.; Sharpless, K. B. *J. Am. Chem. Soc.* **1980**, *102*, 5974-5976. (b) Gao, Y.; Hanson, R. M.; Klunder, J. M.; Ko, S. Y.; Masamune, H.; Sharpless, K. B. *J. Am. Chem. Soc.* **1987**, *109*, 5765-5780.
4. (a) Jung, M. E.; Marquez, R. *Org. Lett.* **2000**, *2*, 1669-1672. (b) Jung, M. E.; Lee, C. P. *Tetrahedron Lett.* **2000**, *41*, 9719-9723. (c) Jung, M. E.; Lee, C. P. *Org. Lett.* **2001**, *3*, 333-336. (d) Jung, M. E.; Yoo, D. *Org. Lett.* **2007**, *9*, 3543-3546. (e) Mitton-Fry, M. J.; Cullen, A. J.; Sammakia, T. *Angew. Chem. Int. Ed.* **2007**, *46*, 1066-1070. (f) Jung, M. E.; Zhang, T. *Org. Lett.* **2008**, *10*, 137-140. (g) Jung, M. E.; Yoo, D. *Tetrahedron Lett.* **2008**, *49*, 816-819. (h) Jung, M. E.; Salehi-Rad, R. *Angew. Chem. Int. Ed.* **2009**, *48*, 8766-8769. (i) Jung, M. E.; Chaumontet, M.; Salehi-Rad, R. *Org. Lett.* **2010**, *12*, 2872-2875.
5. Jung, M. E.; Allen, D. A. *Org. Lett.* **2008**, *10*, 2039-2041. See also: Jung, M. E.; Allen, D. A. *Org. Lett.* **2009**, *11*, 757-760.
6. (a) Stratmann, K.; Moore, R. E.; Bonjouklian, R.; Deeter, J. B.; Patterson, G. M. L.; Shaffer, S.; Smith, C. D.; Smitka, T. A. *J. Am. Chem. Soc.* **1994**, *116*, 9935-9942. (b) Smith, C. D.; Zilfou, J. T.; Stratmann, K.; Patterson, G. M. L.; Moore, R. E. *Mol. Pharm.* **1995**, *47*, 241-247.
7. Allen, D. A. Ph.D. thesis, University of California, Los Angeles, CA, 2010.
8. Frisch, M. J. et al. *Gaussian 03*, revision C.02; Gaussian, Inc.: Wallingford, CT, 2004
9. Fürst, A.; Plattner, P. A. *Helv. Chim. Acta.* **1949**, *32*, 275-283.
10. Safaryn, J. E.; Chiarello, J.; Chen, K. M.; Joullie, M. M. *Tetrahedron.* **1986**, *42*, 2635-2642.

Chapter 4. Origins of Stereoselectivities of Dihydroxylations of *cis*-Bicyclo[3.3.0]octenes

4.1 Abstract

Stereoselectivities of the dihydroxylations of *cis*-bicyclo[3.3.0]octene intermediates for a projected total synthesis of chromodorolide A have been explored experimentally. The reaction occurs unexpectedly on the apparently more hindered (concave) face; this result has been explained through computational studies using B3LYP and B3LYP-D3 methods. Torsional effects are largely responsible for the stereoselectivity encountered in the chromodorolide A synthesis. Many literature examples have been reported on related cases. QM calculations show that the stereoselectivities of dihydroxylations of fused cyclopentenes are influenced by the conformational rigidity or flexibility of the substrate. Torsional, electrostatic, and steric effects can all influence stereoselectivity, and the rigidity or flexibility of conformations of reactants provides a predictive guide to stereoselectivity.

4.2 Introduction

Chromodorolide A (**1**) is a structurally unique diterpene.¹ We envisaged accomplishing its total synthesis by late-stage intramolecular lactonization of a tetracyclic precursor such as **2** (Figure 4.1). In our early exploration in a model series of strategies for assembling such cyclization precursors, we examined dihydroxylation of intermediate

3. To our surprise, the reaction of **3** with OsO₄ occurred with high selectivity from the concave face, which appears to be more sterically hindered (Figure 4.1). As osmium tetroxide-mediated dihydroxylation of double bonds is one of the most useful reactions in organic synthesis,² we felt it worthwhile to explore computationally the origins of the diastereoselectivities of these and related literature reactions. We report the preparation and dihydroxylation of bicyclic alkene **3** and a computational study of the origin of stereoselectivity of the dihydroxylation reaction. We have also reviewed the known cases of osmylations of *cis*-bicyclo[3.3.0]octenes and hetero-substituted cases; we provide a computational study of these systems and explanation of the origins of selectivities. We also show that the conformations of the reactants provide a good guide to the stereoselectivity of reactions.

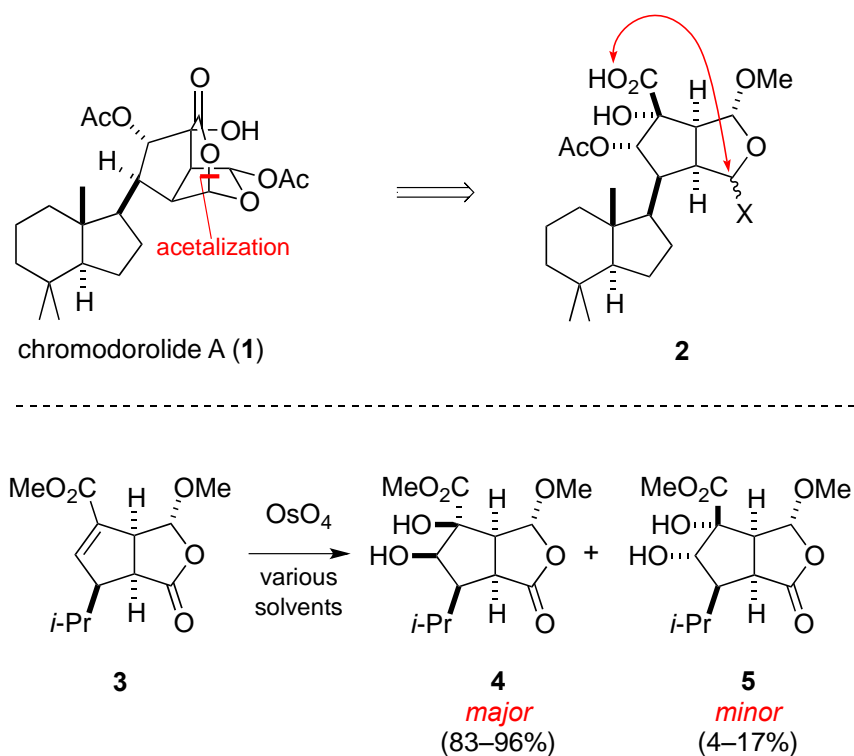


Figure 4.1. Structure of chromodorolide A (**1**) and experimental results of dihydroxylation of *cis*-oxabicyclo[3.3.0]octenone **3**.

4.3 Results and Discussion

4.3.1 Experimental Studies

Cis-oxabicyclo[3.3.0]octenone **3** was prepared by a two-step sequence; the key step was phosphine-promoted (3+2) annulation³ involving allenolate **6**⁴ and butenolide **7**⁵ to furnish **8** (Figure 4.2). Reductive debromination of **8** with zinc and acetic acid delivered oxabicyclooctanone **3** in 20% overall yield. Dihydroxylation of **3** at room temperature with catalytic OsO₄ and NMO in 1:1 *tert*-butanol/H₂O gave a 92:8 mixture of diastereomeric *cis*-diol products **4** and **5** in 87% yield.⁶ Recrystallization of this mixture from CH₂Cl₂ provided the major product, diol **4** (mp 146–147 °C), whose structure was secured by ¹H NMR nOe studies and single-crystal X-ray analysis. Note the oxidation on the concave side of **3**, syn to the lactone, but anti to the two hydrogens at the ring junction.

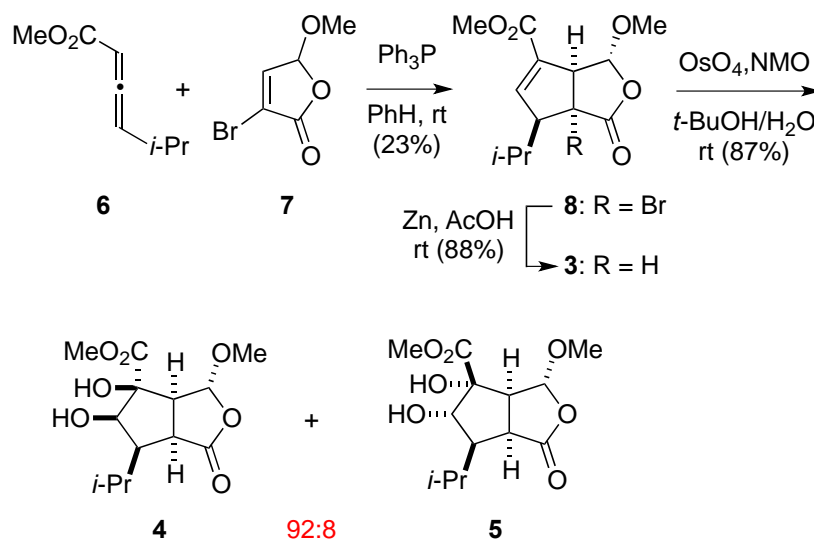


Figure 4.2. Synthesis of *cis*-oxabicyclo[3.3.0]octenone **3** and its dihydroxylation with OsO₄ in aqueous *tert*-butanol.

4.3.2 Computational Studies

All calculations were performed with Gaussian09.⁷ The diastereomeric dihydroxylation transition states of precursor **3** were investigated at the B3LYP⁸ level using the LANL2DZ⁹ basis set for osmium and 6-31G(d) for all other atoms. Energies were calculated with both B3LYP and B3LYP-D3; the conclusions are the same with both methods, and the B3LYP-D3 results are discussed in the text. Conformational searches were performed on compounds **3**, **9**, **11** and **13**. For each compound, the two envelope conformations possible for the cyclopentene ring were created with the flap of the envelope either up or down. Each was then minimized. For **3** and **9**, the minimizations lead to only one envelope conformation for each compound. For **11** and **13**, the minimizations gave two different envelope conformations for each compound.

Only one envelope conformation of the cyclopentene ring of **3** was obtained after transition state optimization, as shown in Figure 4.3. The isopropyl group can adopt a variety of conformations, but only the two lowest energy transition state conformers are shown in Figure 4.3. The α -dihydroxylation transition structure **TS3 α** , with the OsO₄ approaching from the sterically less hindered face of the cyclopentene ring, is 2.2 kcal/mol higher in energy than the β -dihydroxylation transition structure **TS3 β** at the B3LYP level. With B3LYP-D3, which includes dispersion corrections that may be important for such systems, the energy difference between **TS3 α** and **TS3 β** increases to 4.2 kcal/mol. Although the energy difference is overestimated by both methods as compared to experiment, the results are consistent with the experimental observation that the major product is the β -dihydroxylated compound. A variety of other functionals have

been developed, and could be considered for these studies. However, those methods are often computationally much more demanding, and the steric and electronic factors that differ in diastereomeric transition states are known to be adequately differentiated at this level.¹⁰

The energy difference between the transition structures **TS3 α** and **TS3 β** is a result of torsional strain differences. There are two forming C–O bonds in the transition state, one bond is shorter (2.00 Å) and more fully formed than the other (2.17 Å). This asynchronicity is the result of electron-withdrawal and conjugation by the ester group. Inspection of the Newman projections about the bond to the left alkene carbon (shown in red in Figure 4.3) of two transition structures indicates **TS3 β** is slightly more staggered than **TS3 α** (red box insets); torsional differences at the bond to the right alkene carbon, where bond formation is more advanced, are more striking. As seen from the Newman projections for the bond to the right alkene carbon (shown in green), the α -dihydroxylation transition structure **TS3 α** exhibits substantial eclipsing, in contrast to the substantially more staggered β -dihydroxylation transition structure **TS3 β** . For this reaction, the torsional effects override the steric effects, which makes the more crowded **TS3 β** more stable than the less crowded **TS3 α** . Torsional effects direct OsO₄ to attack the cyclopentene ring from the sterically more hindered β -face. Such effects have been reported previously to govern the stereoselectivities in a wide variety of situations.¹¹ The example of epoxidation of an intermediate for a guanacastepene A synthesis^{11e} is especially relevant, and the effect was called “torsional steering”. In this and the other

examples in reference 11, attack on an envelope conformation of a cyclopentene occurs on the concave face because of torsional effects.

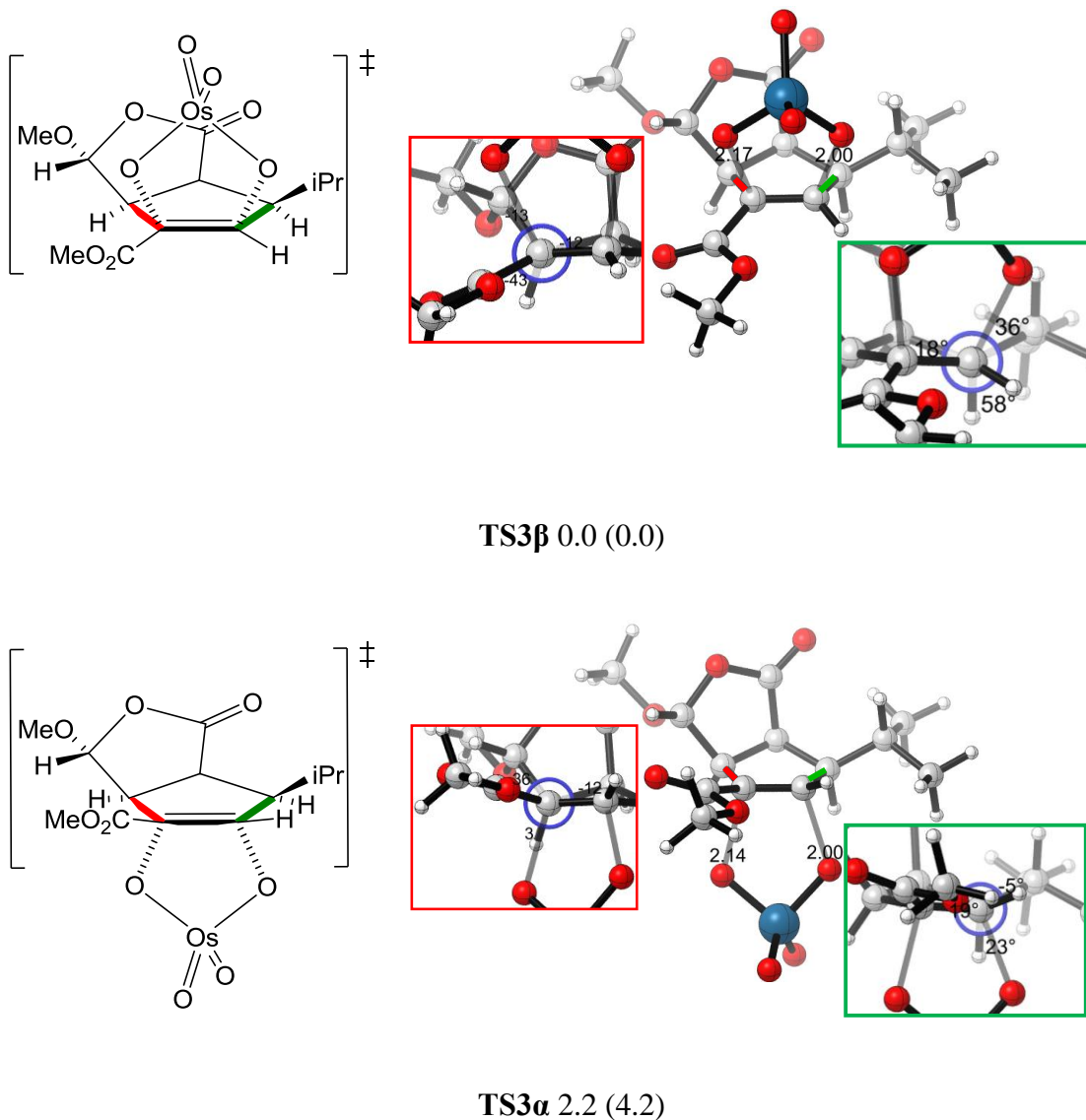
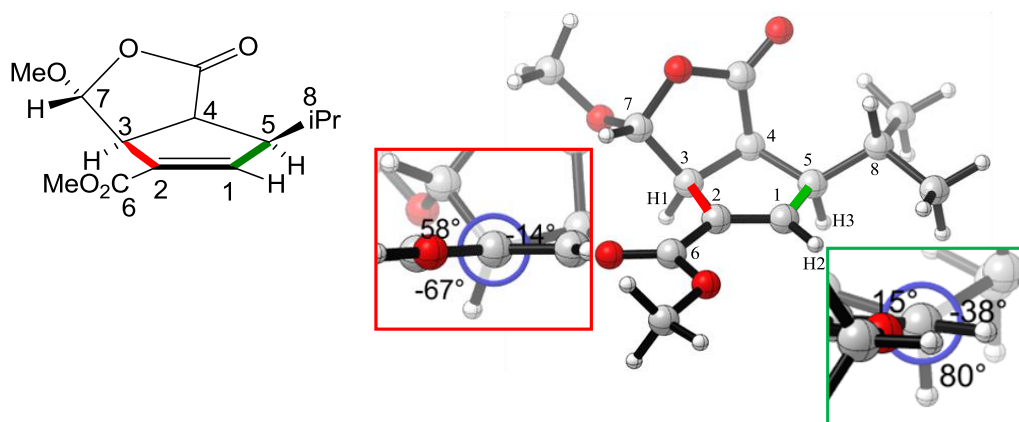


Figure 4.3. Optimized β and α -dihydroxylation transition structures of *cis*-oxabicyclo[3.3.0]octanone **3**. The Newman projections of interest shown in the red and green box insets are viewed along the red and green bonds, respectively. Values below each structure are relative energies in kcal/mol calculated by B3LYP. Values enclosed in parentheses are relative energies in kcal/mol calculated by B3LYP-D3.

The origins of the dihydroxylation stereoselectivities can be identified qualitatively from the geometry of the starting substrate. The energy-minimized geometry of compound **3** is shown in Figure 4.4a.¹² Only one envelope conformation was obtained for the cyclopentene ring after minimization, while the isopropyl group can adopt a variety of different conformations. The other two minimized conformers with isopropyl groups in other orientations are 1.1 and 2.5 kcal/mol higher in energy, respectively. By careful inspection of the substrate structure, in the left C2–C3 bond Newman projections (Figure 4.4a, red box inset), the dihedral angle between the C6 carbonyl carbon and C7 is 58° and 67° for C6 to the allylic hydrogen H1. This analysis indicates that addition from the β face is more favored torsionally than from the α face, which is consistent with the transition state analysis. The more striking torsional difference on the right alkene carbon shown in the TSs is also reflected in the substrate structure itself. In the right C1–C5 bond Newman projections (Figure 4.4a, green box inset), the dihedral angle between the vinyl hydrogen H2 and the central carbon of isopropyl C8 is 38° and 80° to the allylic hydrogen H3. The 42° dihedral angle difference makes the β -face attack more favorable due to the torsional effects, which is consistent with the result obtained by TS exploration (Figure 4.4b). The analysis of the geometries of the substrates again confirms that the stereoselectivities of dihydroxylation result from torsional effects. In this case, the reactant cyclopentene ring is fixed in an envelope conformation, and the analysis of the reactant geometries gives a reliable guide to the direction of attack by osmium tetroxide and, presumably, other electrophiles, radicals and nucleophiles as well. The situation is more complex when two envelope conformers of the cyclopentene are similar in energy. Such examples were found in the literature, as described in the next section.

(a)



(b)

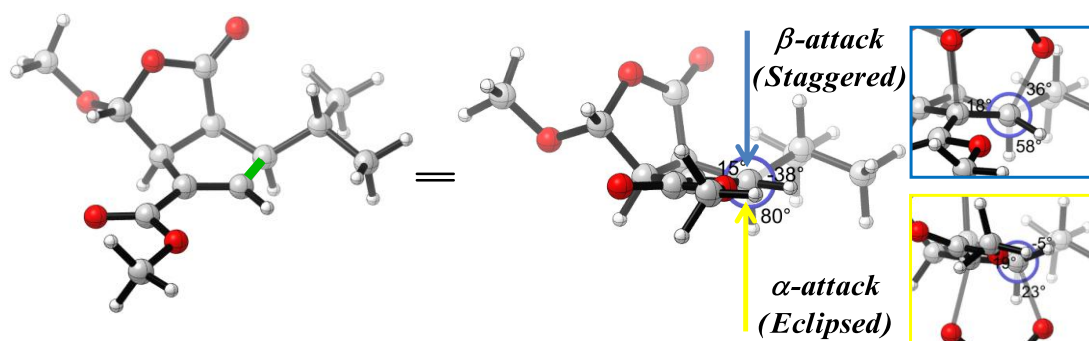


Figure 4.4. (a) Optimized structure of *cis*-oxabicyclo[3.3.0]octenone **3**. (b) The torsional of interest viewed along the green bond. Newman projections shown in the blue and yellow box insets illustrated the resultant torsional effects for the β and α -dihydroxylation transition states.

4.3.3 Literature Examples of Dihydroxylation of Other *cis*-Bicyclo[3.3.0]octenes

A survey of the chemical literature identified a variety of *cis*-bicyclo[3.3.0]octene systems that have been subjected to dihydroxylation. Structure searches are summarized in Table 4.1, reaction searches in Table 4.2. The hits were screened manually to remove

duplicates and extract the 24 relevant examples. A control search (Table 4.3), in which the bridgehead hydrogens were omitted, revealed another 2 relevant examples not found in the previous searches.

Table 4.1. SciFinder substructure searches. Bold bonds indicate the “lock ring fusion tool”, squares around atoms indicate the “lock atoms tool”.

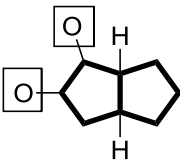
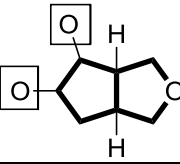
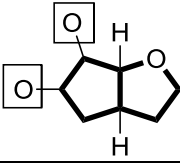
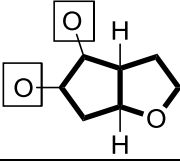
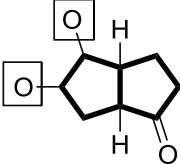
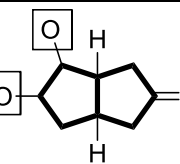
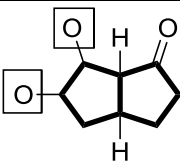
Entry	Search pattern	Hits	Relevant hits
1		44	13
2		16	1
3		34	6
4		23	2
5		2	0
6		6	0
7		0	0

Table 4.2. SciFinder reaction (substructure) searches. Bold bonds indicate the “lock ring fusion tool”.

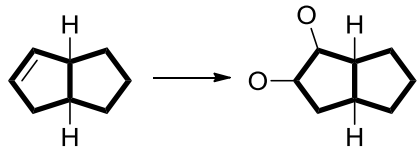
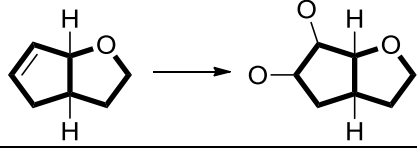
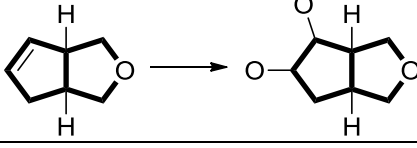
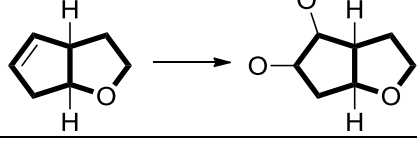
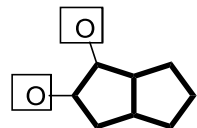
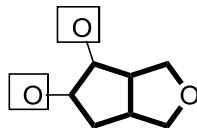
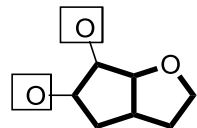
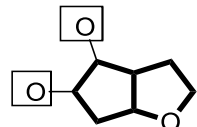
Entry	Search pattern	Hits	Relevant hits not covered in Table 4.1
1		22	2
2		9	0
3		0	0
4		13	0

Table 4.3. SciFinder control substructure searches. Bold bonds indicate the “lock ring fusion tool”, squares around atoms indicate the “lock atoms tool”.

Entry	Search pattern	Hits	Relevant hits not covered in Tables 4.1 or 4.2
1		45	0
2		16	0
3		36	0
4		28	2

The 26 relevant examples are given in Table 4.4. Entries 1–6 signify cases where dihydroxylation occurred from the concave face or both faces, and good evidence for the structural assignment is given. In entries 7–12, diastereomeric mixtures are reported without evidence for the assignment, or the products were not assigned. The dihydroxylation product of Entry 13 is assigned by NOE analysis of a later synthetic intermediate. For Entries 14–26, no evidence is given for the assignment. One of the examples (Entry 24) was refuted by a later publication (Entry 6), where an X-ray crystal structure of the product was obtained.

Table 4.4. Relevant literature examples from the SciFinder literature searches (Tables 4.1–4.3).

Entry	Reaction(s)	Comment	Reference
1		Assignment based on coupling constants.	13
2		"... the carbonyl group may be directing the reaction." Assignment based on NOE.	14
3		"... may be a directing effect from the carbonyl group." Strong solvent effect observed. Assignment based on coupling constants, chemical correlation, and a crystal structure.	15

Entry	Reaction(s)	Comment	Reference										
4		Chemical evidence for assignment.	16										
5		Crystallographic evidence and chemical correlation.	17										
6		Crystal structure.	18										
7		Unassigned 3:1 mixture.	19										
8		Unassigned 1:5:5:1 mixture.	20										
9		Unspecified mixture.	21										
10		Not assigned.	22										
11	<table style="margin-left: auto; margin-right: 0;"> <tr> <td>R</td> <td>exo:endo</td> </tr> <tr> <td>H</td> <td>3:1</td> </tr> <tr> <td>Ac</td> <td>1:3</td> </tr> <tr> <td>Bz</td> <td>1:6</td> </tr> <tr> <td>TBDPS</td> <td>>1:13</td> </tr> </table>	R	exo:endo	H	3:1	Ac	1:3	Bz	1:6	TBDPS	>1:13	No direct evidence for assignment reported.	23
R	exo:endo												
H	3:1												
Ac	1:3												
Bz	1:6												
TBDPS	>1:13												
12		5.5:1 exo:endo reported, no evidence for assignment given.	24										

Entry	Reaction(s)	Comment	Reference
13		NOE assignment of a later intermediate.	25
14		No evidence for assignment reported.	26
15		No evidence for assignment reported.	27
16		No evidence for assignment reported.	28
17		No evidence for assignment reported.	29
18		No evidence for assignment reported.	30
19		No evidence for assignment reported.	31
20		Discussion of the preferred conformation of the product (through coupling constants). No direct evidence for assignment reported.	32
21		No evidence for assignment reported.	33

Entry	Reaction(s)	Comment	Reference
22		No evidence for assignment reported.	34
23		No evidence for assignment reported.	35
24		No evidence for assignment reported. Refuted by Entry 6.	36
25		No evidence for assignment reported.	37
26		No evidence for assignment reported.	38

Out of a total of 26 relevant transformations, there is rigorous experimental evidence for the structural assignment of the diol product(s) in only seven cases. This striking fact is a result of the difficulty of obtaining solid evidence for the configurational assignments of *cis*-bicyclo[3.3.0]octane ring systems, as ^1H coupling constant analysis and nOe data are often ambiguous.

As shown in Table 4.4, for the 26 *cis*-bicyclo[3.3.0]octene systems studied, the rings fused to the cyclopentene ring are mainly lactones and cyclic ketones or derivatives with different substituents. After dihydroxylation, most of those dihydroxylated intermediates were incorporated in a total synthesis of natural products or other important target.

Despite the general importance of such transformations for *cis*-bicyclo[3.3.0]octene systems, none of the 26 examples published included any discussion of the factors controlling the stereoselectivities. In order to better understand these transformations and to provide guidelines for synthetic chemists to predict the preferred products of reactions of this type, we explored in detail the three simple examples shown in Figure 4.5. These are representative of the types of molecules included in the 26 examples in Table 4.4. These do not include substituents, and include one cyclic ketone, **11**, and two lactones, **9** and **13**. In example (i), dihydroxylation of *cis*-oxabicyclo[3.3.0]octenone **9** took place preferentially from the concave face to give the β -diol product **10**. In the first report of this transformation,¹⁵ the major product was assigned-without experimental evidence-as arising from convex-face dihydroxylation, but this structural assignment was later reversed by means of an X-ray crystal structure.¹⁸ In the second example (ii), *cis*-bicyclo[3.3.0]octenone **11** was dihydroxylated also preferentially from the concave face to give diol **12** with relatively low 4:1 selectivity.¹⁴ It was hypothesized in this report that the selectivity may be due to a directing effect of the carbonyl group, as conversion of the ketone into a protected β -alcohol inverts the facial selectivity.

In example (iii), high diastereoselectivity for dihydroxylation from the convex face of **13** to give diol **14** is reported; however, no direct experimental evidence was given to support this structural assignment.³³⁻³⁵ Our computational studies, described below, suggest that the reported assignment is correct.

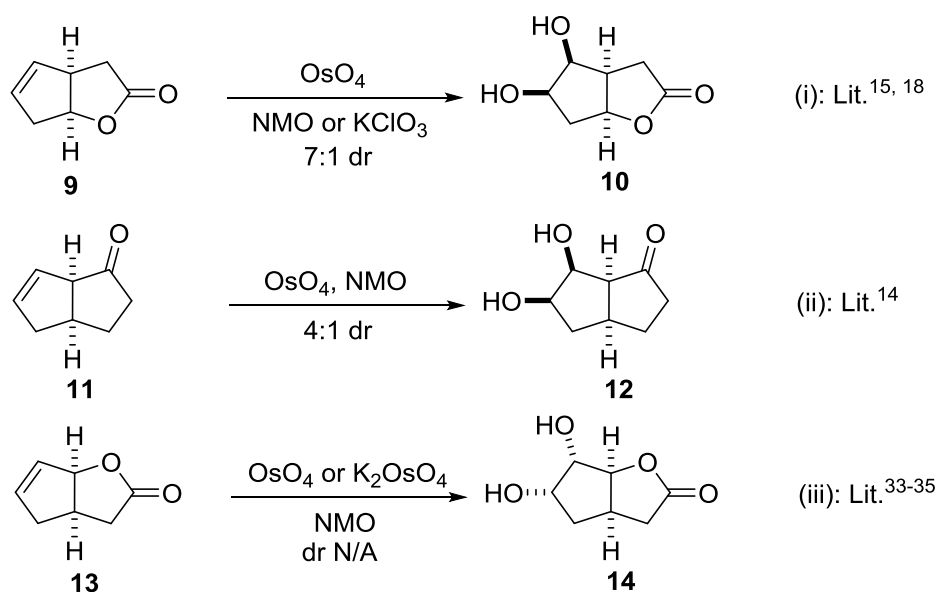


Figure 4.5. Selected literature examples of dihydroxylation of *cis*-bicyclo[3.3.0]octenes using osmium reagents.

We first performed a conformational search on **9**, **11** and **13**. Compounds **11** and **13** have two different energy minima, while **9** has only one low-energy conformation. The cyclopentene ring adopts an envelope conformation in which four of the carbon atoms C1, C2, C3 and C5 are coplanar, while C4 can be above or below the plane. For compounds **11** and **13**, two different minimum energy conformations were located having similar energies (Figure 4.6). However, for compound **9**, there is only one minimum energy conformation for the cyclopentene ring, with C4 above the plane (**R9**, Figure 4.6). This is the same situation as with compound **3** described earlier.

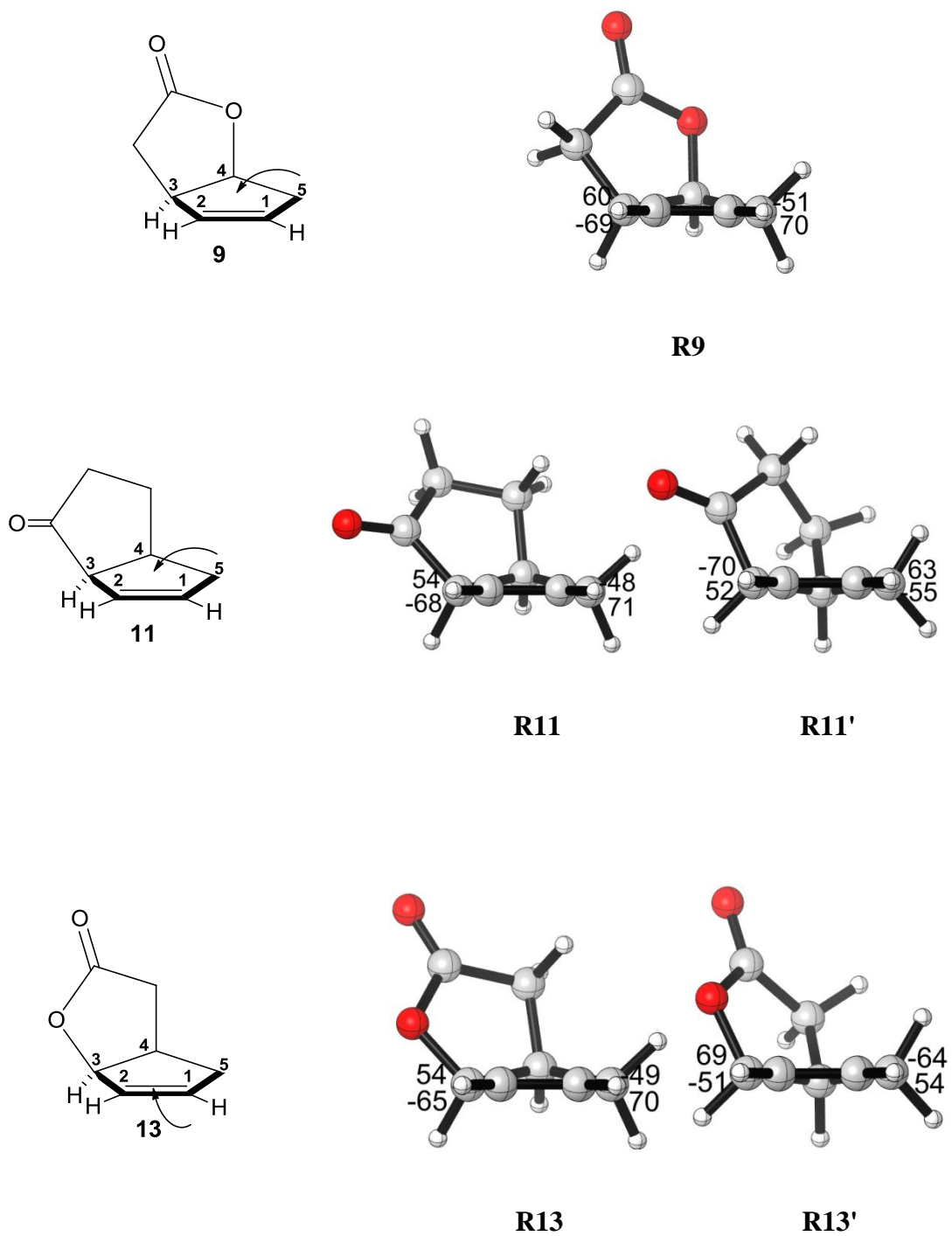


Figure 4.6. Three fused cyclopentene compounds and their optimized geometries. In **R9**, **R11** and **R13**, the flap of the envelope is up; in **R11'** and **R13'**, it is down.

This ground state difference is also reflected in the TSs of the osmylation reactions. Compound **9** has only one conformation, and both α and β -dihydroxylation transition structures are based on this conformation. **TS9 β** is calculated to be 1.6 kcal/mol more stable than **TS9 α** using B3LYP-D3 calculations, consistent with the stereoselectivities observed experimentally. From the structures shown in Figure 4.7, the different stabilities between two transition structures are also most likely due to the torsional strain, as in the TS analysis of dihydroxylation of **3**.

For compounds **11** and **13**, the situations are more complicated, because there are two possible conformations of the substrates. After TS searches, the lowest energy β -dihydroxylation transition structures **TS11 β** and **TS13 β** were located, and they are related to conformations **R11** and **R13**. Transition structures **TS11 α** and **TS13 α** are structurally related to conformations **R11'** and **R13'**. The different conformation preferences of different TSs can be rationalized from the substrate conformation itself. From the substrate geometries shown in Figure 4.7, the β face is more torsionally favored in **R11** and **R13**, whereas the α face is more torsionally favored in **R11'** and **R13'**. The β and α -dihydroxylation transition structures avoid torsional strain and involve the conformations that result in less torsional strain. In both **11** and **13**, both α and β attack can occur from a concave face of an envelope cyclopentene, due to the flexibility of the cyclopentene.

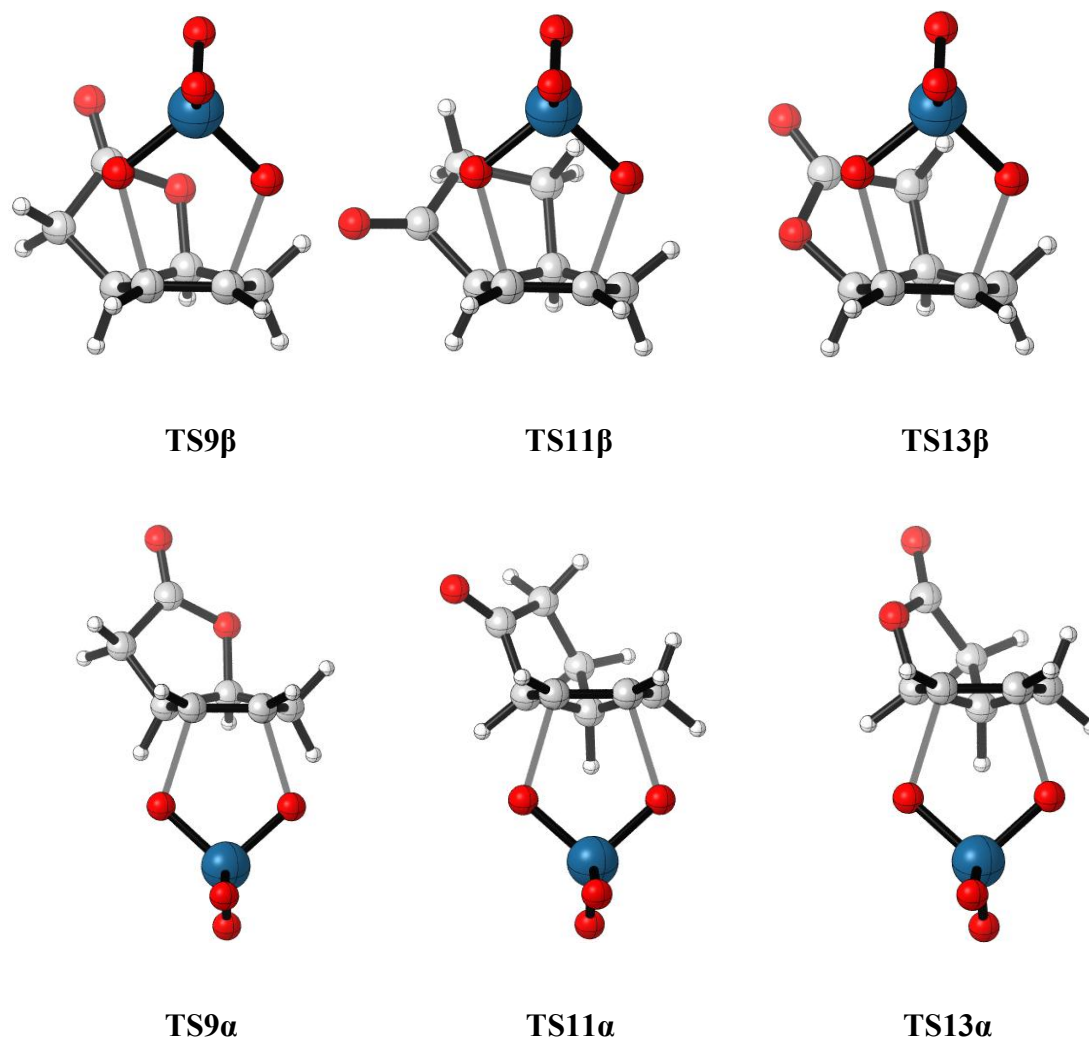


Figure 4.7. Optimized β and α -dihydroxylation transition structures of *cis*-bicyclo[3.3.0]octenes **9**, **11** and **13**.

For compound **11**, **TS11 α** has similar torsional strain as **TS11 β** , but **TS11 β** is still calculated to be 0.8 kcal/mol more stable than **TS11 α** using B3LYP-D3; this result agrees with the 4:1 preference for β attack observed experimentally. The different stabilities of the two TSs are presumably a result of the electrostatic interactions between the carbonyl carbon and OsO₄ oxygen inside the concave-face attack **TS11 β** , which makes it a little

more stable than the convex-face attack **TS11 α** . This attractive interaction is related to the O \cdots C=O interaction identified by Raines in various protein structures.³⁹

For compound **13**, as with **11**, the torsional differences are not large between **TS13 β** and **TS13 α** . However, now, **TS13 α** is calculated to be more stable than **TS13 β** by 1.6 kcal/mol by B3LYP-D3, which predicts the correct stereoselectivity in the experiment. The stability difference between these two TSs is likely due to differences in O-O repulsions, which makes the more crowded and electrostatically disfavored **TS13 β** less stable than the less crowded **TS13 α** .

In order to determine the reason for the different conformational properties of different reactants, we performed a conformational analysis. For **3** and **9**, we were able to locate only one envelope conformation of the cyclopentene with C4 above the plane. The other envelope conformation of the cyclopentene ring for **3** and **9** was manually created by freezing C4 below the plane.⁴⁰ The rest skeleton of the molecules was then optimized and the optimized structures **R3a'**, **R9'** are calculated less stable than **R3a** and **R9** by 2.0, 1.8 kcal/mol, respectively. If no restrictions are given to the systems, **R3a'**, **R9'** will go back to **R3a**, **R9** after re-optimization. This result indicates that the availability of only one envelope conformation for **3a** and **9** is a result of the remarkable instabilities of the other envelope conformations. From the structures of **R3a** and **R3a'**, all the bond distances of the fused ring in the two conformations are similar; indicating there is little ring strain differences in between. The different stabilities between **R3a** and **R3a'** are due to torsional effects. Inspection of the Newman projections of C7-C3 (green bond in

Figure 4.8a) show that **R3a** is slightly more staggered than **R3a'**. This is also true for **R9** and **R9'** as shown in the Newman projections (green box insets) in Figure 4.8b.

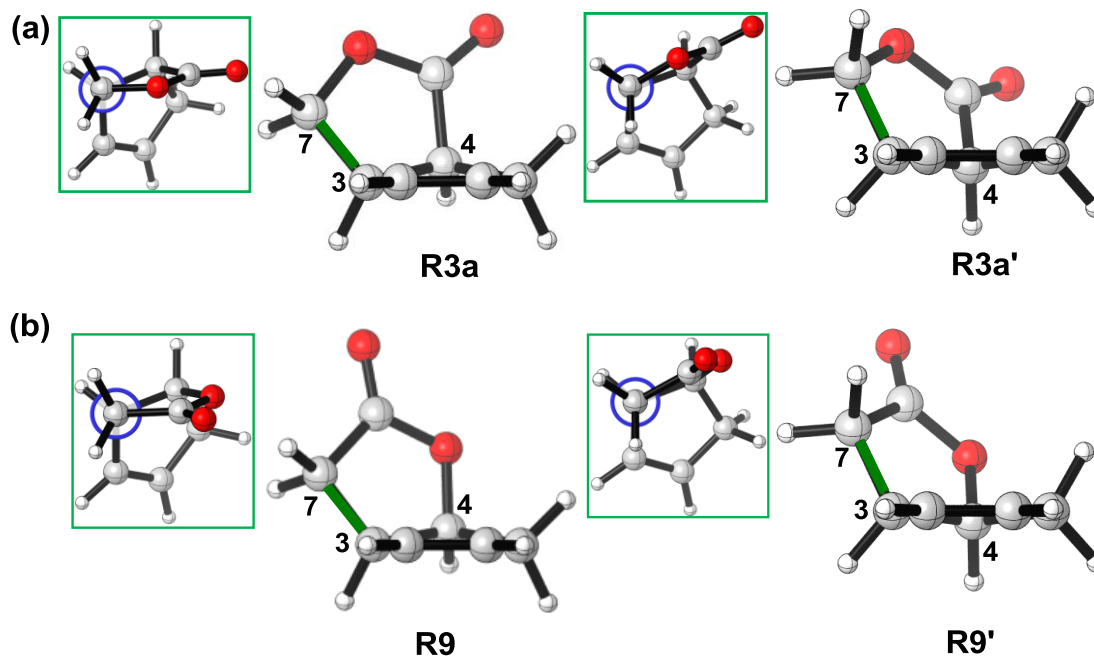


Figure 4.8. Optimized structures of (a) **R3a** and **R3a'** (b) **R9** and **R9'**.

However, for **11** and **13**, two envelope conformations with similar energies were located for the substrates. Now, the atom in position 7 is no longer a sp^3 carbon, and the torsional differences for bond C7 (or O)-C3 no longer exist according to the Newman projections shown in Figure 4.9. As a result, two envelope conformations of the reactants are both available and similar in energy.

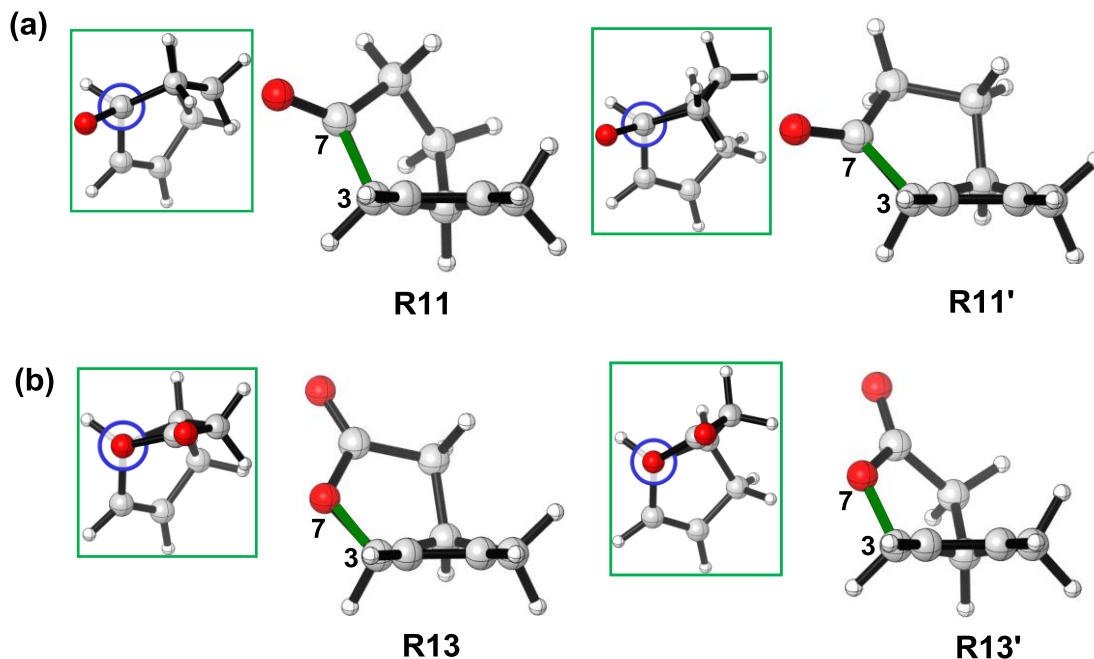


Figure 4.9. Optimized structures of (a) **R11** and **R11'** (b) **R13** and **R13'**.

4.4 Conclusion

In dihydroxylations of fused cyclopentene systems, and presumably other additions, when only one envelope conformational minimum is accessible in the reactant, torsional effects always steer attack to the concave face. In cases studied here, the torsional factors override other factors and determine stereoselectivity. However, when the cyclopentene ring is able to adopt two different low-energy conformations, both top and bottom attack can occur on a concave face of the cyclopentene envelope. As a result, torsional factors no longer dominate the stereoselectivity. The stereoselectivity in such cases is then determined by other factors such as steric and electrostatic interactions or both, as demonstrated in the dihydroxylations of compounds **11** and **13**.

4.5 References

1. (a) Dumdei, E. J.; de Silva, E. D.; Andersen, R. J.; Choudhary, M. I.; Clardy, J. *J. Am. Chem. Soc.* **1989**, *111*, 2712–2713. (b) Morris, S. A.; de Silva, E. D.; Andersen, R. J. *Can. J. Chem.* **1991**, *69*, 768–771.
2. Kolb, H. C.; VanNieuwenzhe, M. S.; Sharpless, K. B. *Chem. Rev.* **1994**, *94*, 2483-2547.
3. (a) Ruano, J. L.; Núñez, Jr., A.; Martín; Fraile, A. *J. Org. Chem.* **2008**, *73*, 9366-9371. (b) Lu, X.; Zhang, C.; Xu, Z. *Acc. Chem. Res.* **2001**, *34*, 535-544.
4. (a) De March, P.; Font, J.; Gracia, A.; Qingying, Z. *J. Org. Chem.* **1995**, *60*, 1814–1822. (b) Rout, L.; Harned, A. M. *Chem. Eur. J.* **2009**, *15*, 12926–12928.
5. Fariña, F.; Martín, M. R.; Martín, M. V. *An. Quim.* **1979**, *75*, 144–149.
6. VanRheenen, V.; Kelly, R. C.; Cha, R. C. *Tetrahedron Lett.* **1976**, *17*, 1973-1976.
7. Frisch, M. J. et al. *Gaussian 09*, revision B.01; Gaussian, Inc.: Wallingford, CT, 2010.
8. (a) Becke, A. D. *J. Chem. Phys.* **1993**, *98*, 5648-5652. (b) Lee, C.; Yang, W.; Parr, R. G. *Phys. Rev.* **1988**, *37*, 785-789.
9. Hay, P. J.; Wadt, W. R. *J. Chem. Phys.* **1985**, *82*, 299-310.
10. (a) For dispersion correction, see: (a) Grimme, S. *J. Comput. Chem.* **2006**, *27*, 1787-1799. (b) Grimme, S.; Antony, J.; Ehrlich, S.; Krieg, H. *J. Chem. Phys.* **2010**, *132*, 154104. For application of dispersion corrected DFT in computational chemistry, see: (c) McMullin, C. L.; Jover, J.; Harvey, J. N.; Fey, N. *Dalton Trans.* **2010**, *39*, 10833-10836. (d) Antoline, J. E.; Krenske, E. H.; Lohse, A. G.; Houk, K. N.; Hsung, R. P. *J. Am. Chem. Soc.* **2011**, *133*, 14443-14451.
11. (a) Caramella, P.; Rondan, N. G.; Paddon, M. N.; Houk, K. N. *J. Am. Chem. Soc.* **1981**, *103*, 2438–2440. (b) Rondan, N. G.; Paddon, M. N.; Caramella, P.; Mareda, J.; Mueller, P. H.; Houk, K. N. *J. Am. Chem. Soc.* **1982**, *104*, 4974–4976. (c) Paddon, M. N.; Rondan, N. G.; Houk, K. N. *J. Am. Chem. Soc.* **1982**, *104*, 7162–7166. (d) Lucero, M. J.; Houk, K. N. *J. Org. Chem.* **1998**, *63*, 6973–6977. (e) Cheong, P. H.; Yun, H.; Danishefsky, S. J.; Houk, K. N. *Org. Lett.* **2006**, *8*, 1513–1516. (f) Martinelli, M. J.; Peterson, B. C.; Khau, V. V.; Hutchison, D. R.; Leanna, M. R.; Audia, J. E.; Droste, J. J.; Wu, Y.-D.; Houk, K. N. *J. Org. Chem.* **1994**, *59*, 2204–2210. (g) Houk, K. N.; Paddon, M. N.; Rondan,

- N. G.; Wu, Y.-D.; Brown, F. K.; Spellmeyer, D. C.; Metz, J. T.; Li, Y.; Loncharich, R. J. *Science* **1986**, *231*, 1108–1117.
12. The single-crystal X-ray model of the benzyl analogue of **3** shows no significant differences from the computational model, with torsional angles about the C1–C5 bond being nearly identical.
 13. Clive, D. L. J.; Magnuson, S. R.; Manning, H. W.; Mayhew, D. L. *J. Org. Chem.* **1996**, *61*, 2095–2108.
 14. Leonard, J.; Hussain, N. *J. Chem. Soc. Perkin Trans. 1* **1994**, 49–60.
 15. Broom, N.; O'Hanlon, P. J.; Simpson, T. J.; Stephen, R.; Willis, C. L. *J. Chem. Soc. Perkin Trans. 1* **1995**, 3067–3072.
 16. Kon, J.; Isoe, S. *Tetrahedron Lett.* **1980**, *21*, 3399–3402.
 17. (a) Boschelli, D.; Smith, A. B., III *Tetrahedron Lett.* **1981**, *22*, 3733–3736. (b) Smith, A. B., III; Boschelli, D. *J. Org. Chem.* **1983**, *48*, 1217–1226.
 18. Freimanis, J.; Gerca, L.; Turovskis, I.; Liepinš, E.; Lola, D.; Mishnev, A.; Bundule, M.; Bleidelis, J. *J. Prakt. Chem.* **1987**, *329*, 39–48.
 19. Ritterskamp, P.; Demuth, M.; Schaffner, K. *J. Org. Chem.* **1984**, *49*, 1155–1158.
 20. Stolle, A.; Antonicek, H.-P.; Lensky, S.; Voerste, A.; Müller, T.; Baumgarten, J.; von dem Bruch, K.; Müller, G.; Stropp, U.; Horváth, E.; de Vry, J.-M.-V.; Schreiber, R. *PCT Int. Appl.* **1999**, WO 9936417.
 21. (a) Nelson, N. A.; Jackson, R. W. *Tetrahedron Lett.* **1976**, *37*, 3275–3278. (b) Nelson, N. A.; Scahill, T. A. *J. Org. Chem.* **1979**, *44*, 2790–2793. (c) Nelson, N. A.; Galesburg, M. *U. S. Patent* **1977**, US 4048194. (d) Kelly, R. C.; Nelson, N. A. *U. S. Patent* **1977**, US 4020173. (e) Schneider, W. P. *U. S. Patent* **1977**, US 4018804.
 22. Kan, T.; Kawamoto, Y.; Asakawa, T.; Furuta, T.; Fukuyama, T. *Org. Lett.* **2008**, *10*, 169–171.
 23. Johansen, S. K.; Lundt, I. *J. Chem. Soc. Perkin Trans. 1* **1999**, 3615–3622.
 24. (a) Whitesell, J. K.; Matthews, R. S. *J. Org. Chem.* **1977**, *42*, 3878–3882. (b) Whitesell, J. K.; Wang, P. K. S.; Aguilar, D. A. *J. Org. Chem.* **1983**, *48*, 2511–2515.
 25. Bøjstrup, M.; Fanefjord, M.; Lundt, I. *Org. Biomol. Chem.* **2007**, *5*, 3164–3171.
 26. Leonard, J.; Hewitt, J. D.; Ouali, D.; Bennett, L. R.; Mahmood, A.; Simpson, S. *J. Tetrahedron* **2002**, *58*, 4681–4691.

27. Parkes, K. E. B.; Pattenden, G. *J. Chem. Soc. Perkin Trans. 1* **1988**, 1119–1134.
28. Kojima, K.; Koyama, K.; Amemiya, S.; Saito, S. *Chem. Pharm. Bull.* **1987**, *35*, 948–956.
29. Kon, K.; Isoe, S. *Helv. Chim. Acta* **1983**, *66*, 755–756.
30. Furuichi, K., Miwa, T. *Tetrahedron Lett.* **1974**, *42*, 3689–3692.
31. (a) Brewster, D.; Myers, M.; Ormerod, J.; Spinner, M. E.; Turner, S.; Smith, A. C. B. *J. Chem. Soc. Chem. Commun.* **1972**, 1235–1236. (b) Brewster, D., Myers, M.; Ormerod, J.; Otter, P.; Smith, A. C. B.; Spinner, M. E.; Turner, S. *J. Chem. Soc. Perkin Trans. 1* **1973**, 2796–2804. (c) Turner, S. *Ger. Offen.* **1973**, DE 2246867. (d) Turner, S. *Ger. Offen.* **1974**, DE 2264367.
32. Ghera, E. *J. Org. Chem.* **1968**, *33*, 1042–1051.
33. Neufellner, E.; Kapeller, H.; Griengl, H. *Tetrahedron* **1998**, *54*, 11043–11062.
34. Ernst, M.; Helmchen, G. *Angew. Chem. Int. Ed.* **2002**, *41*, 4054–4056.
35. Marschner, C.; Baumgartner, J.; Griengl, H. *J. Org. Chem.* **1995**, *60*, 5224–5235.
36. Gruber, L.; Tömösközi, I., Major, E., Kovács, G. *Tetrahedron Lett.* **1974**, *42*, 3729–3730.
37. Hussain, N.; Leonard, J. *Tetrahedron Lett.* **1987**, *28*, 4871–4874.
38. Whitesell, J. K.; Matthews, R. S.; Minton, M. A.; Helbling, A. M. *J. Am. Chem. Soc.* **1981**, *103*, 3468–3472.
39. (a) Choudhary, A.; Gandla, D.; Krow, G. R.; Raines, R. T. *J. Am. Chem. Soc.* **2009**, *131*, 7244–7246. (b) Jakobsche, C. E.; Choudhary, A.; Miller, S. J.; Raines, R. T. *J. Am. Chem. Soc.* **2010**, *132*, 6651–6653.
40. In order to simplify the calculation, all the substituents on **3** were removed, and the truncated substrate is referred to as **3a**.

Chapter 5. Origins of Stereoselectivities in Chiral Phosphoric Acid-Catalyzed Allylborations and Propargylations of Aldehydes

5.1 Abstract

The chiral BINOL-phosphoric acid catalyzed allylboration and propargylation reactions are studied with density functional theory (B3LYP and B3LYP-D3). Two different models were recently proposed for these reactions by Goodman and our group, respectively. In Goodman's model for allylborations, the catalyst interacts with the boronate pseudo-axial oxygen. By contrast, our model for propargylations predicts that the catalyst interacts with the boronate pseudo-equatorial oxygen. In both models, the phosphoric acid stabilizes the transition state by forming a strong hydrogen bond with the oxygen of the boronate, and is oriented by a formyl hydrogen bond (Goodman model), and by other electrostatic attractions in our model. Both of these models have now been reinvestigated for both allylborations and propargylations. For the most effective catalyst for these reactions, the lowest energy transition state corresponds to Goodman's axial model, while the best transition state leading to minor enantiomer involves the equatorial model. The high enantioselectivity observed with only the bulkiest catalyst arises from the steric interactions between the substrates and the bulky groups on the catalyst, and the resulting necessity for distortion of the catalyst in the disfavored transition state.

5.2 Introduction

Asymmetric allylboration of carbonyls are valuable methods in organic synthesis, and occur with high enantioselectivity and diastereoselectivity.¹ The most common method for enantioselective allylboration involves chiral allylboron reagents.² However, the preparation of chiral allylboranes and allyl boronates often requires multiple steps and can be challenging. Enantioselective allylboration involving catalytic chiral Lewis acids³ or Brønsted acids⁴ have now been developed. In particular, chiral BINOL-phosphoric acids that have been employed in many other asymmetric reactions^{5,6} were recently demonstrated by Antilla to catalyze the enantioselective allylboration reaction between allylboronate **1** and benzaldehyde **2** (Figure 5.1).⁷ The homoallylic alcohol **3** was obtained in 99% yield and 93% ee with catalyst **PA1** bearing bulky 3,3'-substituents. For other aldehydes, including electron-donating aromatic aldehydes, electron-withdrawing aromatic aldehydes and aliphatic aldehydes, the enantioselectivities vary from 73% to 99% ee. The asymmetric propargylation involving allenyl boronic acid pinacol ester **1'** and benzaldehyde **2** was efficiently catalyzed by **PA1** as well, which gave homopropargylic alcohol **3'** in high yield and ee.⁸ Catalysts where the Ar groups are less bulky gave much lower ee values.

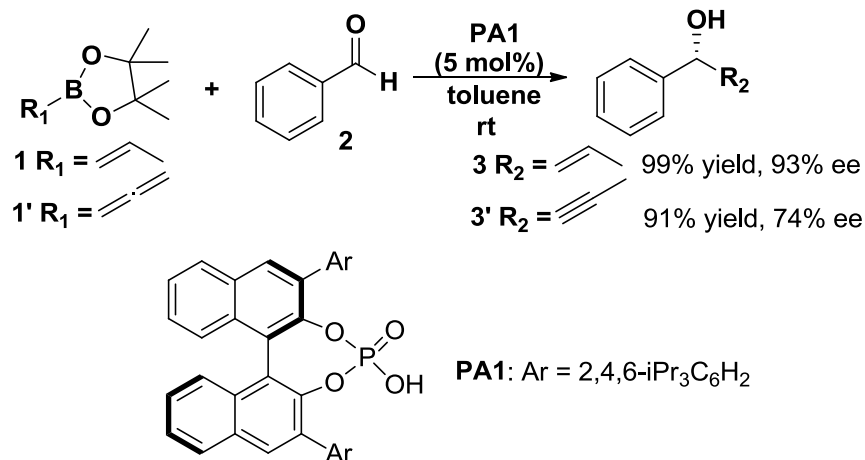


Figure 5.1. Chiral phosphoric acid-catalyzed allylboration and propargylation of benzaldehyde.

Using computational methods, we recently proposed a model to explain the enantioselectivities in propargylations.⁸ In our model (Figure 5.2), the phosphoric acid establishes a H-bond with the pseudo-equatorial oxygen of the boronate. The high enantioselectivities observed for **PA1** originate from the larger distortion of the catalyst in the disfavored TS, which is the result of avoiding steric interactions between the allenylboronate methyls and the bulky substituents in the catalyst. At almost the same time, Grayson, Pellegrinet, and Goodman published a computational study of allylboration reactions.⁹ In the Goodman et al. work, it was proposed that the hydroxyl group of BINOL phosphoric acid H-bonds to the pseudo-axial oxygen of the boronate, and the phosphoryl oxygen interacts with the aldehyde formyl hydrogen through electrostatic interactions (Figure 5.2). Due to the large size of the real catalyst, Goodman used ONIOM calculations on the full catalyst **PA1**. The high enantioselectivities were rationalized from the unfavorable steric clash between the pinacol methyl groups and the large alkyl-substituted aromatic group of the catalyst. Despite the differences in the

activation modes of two models, steric effects or the resulting distortions of the catalyst are believed to determine the origins of the stereoselectivities in these reactions.

We have reinvestigated the chiral BINOL-phosphoric acid catalyzed allylboration and propargylation reactions using several levels of DFT calculations. In order to study the enantioselectivity of the catalysis, the two different models were evaluated. In addition, we used B3LYP-D3, which includes dispersion energies,¹⁰ to calculate the transition state energies, which may also be important to such systems. Using biphenol (BIPOL)-derived phosphoric acid as the model catalyst, we found that the two competing models are comparable in energy. The diastereomeric TSs involved in allylborations and propargylations for **PA1** were located using fully DFT optimization, and the calculated energies by B3LYP and B3LYP-D3 indicated that both pathways were involved for these systems. Goodman's model with axial coordination has a lower energy for *re*-face attack TS, which leads to the major enantiomeric product. However, in our calculations, for *si*-face attack TS, our model is more stable than Goodman's model, which indicated that the minor enantiomeric TS comes from equatorial coordination of the catalyst.

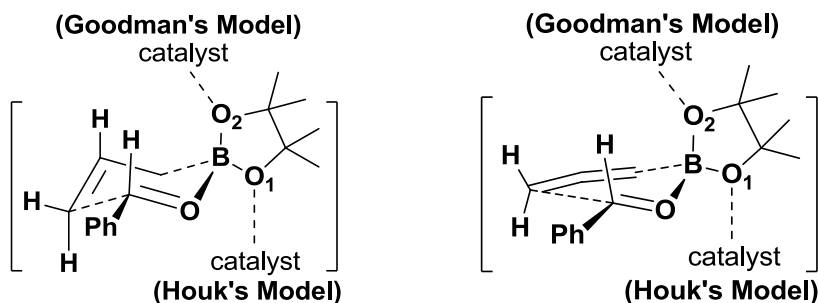


Figure 5.2. Two models for the chiral phosphoric acid-catalyzed allylboration and propargylation of benzaldehyde.

5.3 Results and Discussion

5.3.1 Investigation of the reaction mechanism

The allylboration reaction proceeds via a closed six-membered chairlike transition state.¹¹ There are three possible coordination positions for the catalyst hydroxyl group: the two boronate oxygens or the aldehyde oxygen. In Goodman's and our models, the phosphoric acid forms a hydrogen bond with the boronate oxygens: either the pseudo-equatorial oxygen (path i: eq), or the pseudo-axial oxygen (path ii: ax). The other plausible mechanistic pathway is the phosphoric acid forming a H-bond with the oxygen of the aldehyde (path iii).

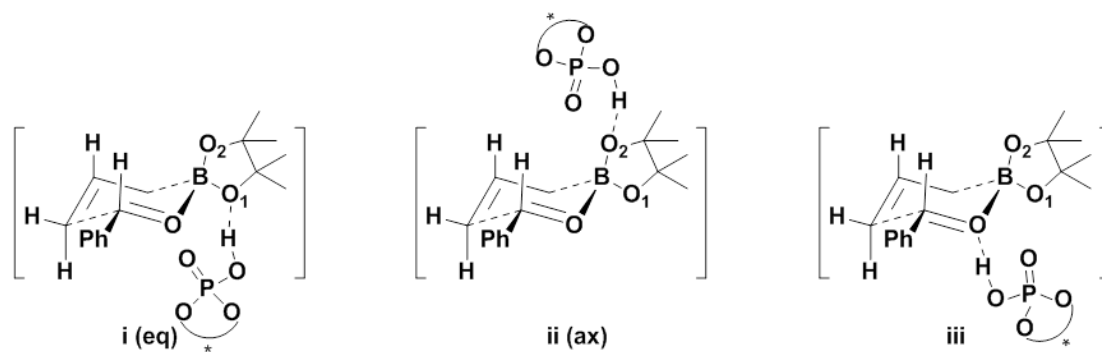
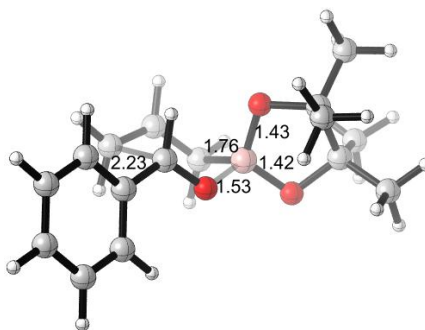


Figure 5.3. Three possible sites of coordination in the phosphoric acid-catalyzed allylboration reaction.

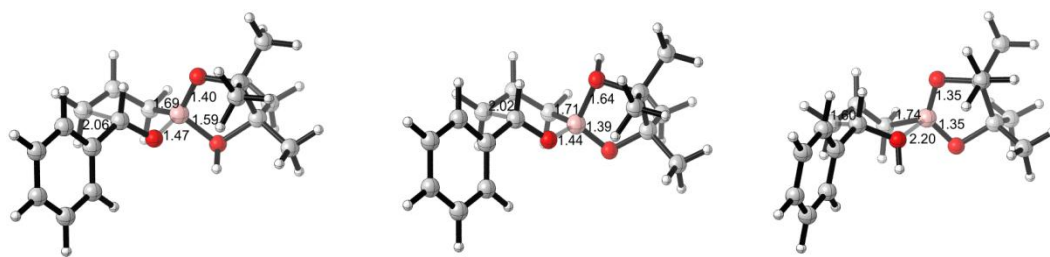
In order to evaluate these different pathways, we first explored transition states where each of the oxygens was protonated. All calculations were performed with the Gaussian 09 package.¹² Geometries were fully optimized in the gas phase and characterized by frequency calculations using B3LYP functional and 6-31G* basis set.

Free energies were calculated for each stationary point. The optimized chairlike transition state structure of the uncatalyzed reaction is shown in Figure 5.4, and the transition states for the three possible sites of protonation are shown in Figure 5.5 along with their relative Gibbs free energies.



TS

Figure 5.4. Optimized transition state of the uncatalyzed allylboration of benzaldehyde at the B3LYP/6-31G* level of theory.



TS1 (0.0)

TS2 (+3.6)

TS3 (+4.3)

Figure 5.5. Optimized transition states of different mechanisms at the B3LYP/6-31G* level of theory. Bond lengths are given in Å. Relative free energies (kcal/mol) are shown in parentheses.

As shown in Figure 5.5, the pathways involving protonation of boronate oxygens (**TS1**: 0.0 kcal/mol, **TS2**: +3.6 kcal/mol) are more favorable than **TS3** (+4.3 kcal/mol) which involves protonation of the aldehyde oxygen. Protonation of a B-O increases the electrophilicity of the boronate and lowers the activation energy.¹³ This finding is in agreement with Hall's experimental observations¹⁴ and Fujimoto's theoretical studies¹⁵ of similar Lewis acid catalyzed allylboration reactions. Similarly, for propargylations, protonation of boronate oxygens accelerates more than protonation of aldehyde.

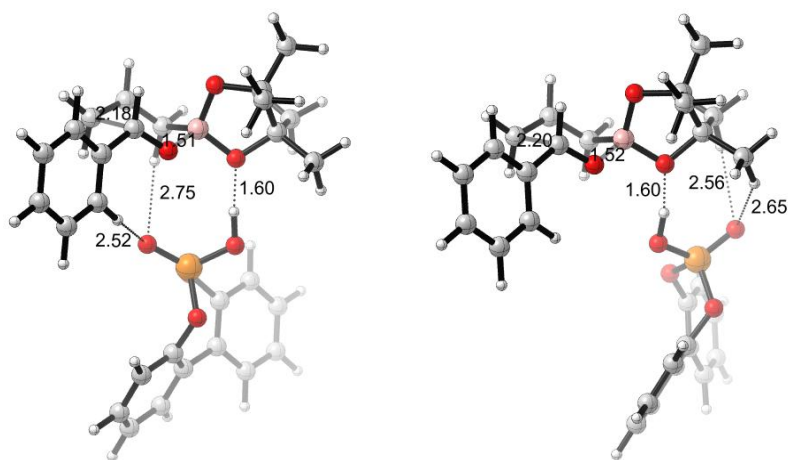
5.3.2 Model of the phosphoric acid-catalyzed allylboration reaction

The mechanistic studies reported above illustrate that activation of boronate oxygens are more favorable than activation of aldehyde oxygen. This phenomenon is also found in Goodman's model study calculations. In order to better understand the boronate activation pathways, catalyst **PA** without Ar substituents was then employed to study both paths i and ii in more detail. In order to reduce the computational cost, the biphenol (BIPOL)-derived phosphoric acid was initially used as the model instead of the BINOL-derived phosphoric acid. This kind of truncating has previously been justified by Yamanaka, Akiyama and Goodman in their studies.⁶ Replacement of the binaphthyl backbone with a smaller biaryl does not significantly alter the geometry around the reaction center.

In both pathways i (eq) and ii (ax), the catalyst interacts with the allylboronate by a single hydrogen bond, and the orientation of the phosphate with respect to the substrate is not fixed. As a result, the remaining parts of the catalyst are conformationally flexible, and there are many possible diastereomeric transition state structures with different orientations of the catalyst. To explore all accessible conformations of the transition states, a conformational search was performed.

For pathway i, two low energy transition state structures, **TS4** and **TS4'**, were located for the phosphoric acid-catalyzed allylboration reaction (Figure 5.6a). In **TS4**, the lowest energy minimum for i, the phosphoryl oxygen was near the six-membered transition state; in **TS4'**, the phosphoryl oxygen is away from the six-membered ring, but next to the boronate methyls. **TS4'** is 1.4 kcal/mol less stable than **TS4**. Since B3LYP may underestimate the aromatic and dispersion interactions in such systems, a method which is expected to treat such interactions more accurately was used to calculate the energy differences between different transition states as well. The energy difference between **TS4** and **TS4'** is calculated to be 2.0 kcal/mol with B3LYP-D3, which includes a dispersion energy correction. For pathway ii, involving H-bonds to the pseudo-axial boronate oxygen, two different diastereomeric transition state conformers, **TS5** and **TS5'** were also found (Figure 5.6b). **TS5**, in which the phosphoryl oxygen is situated over the six-membered ring TS, was more energetically favorable than **TS5'** by 3.0 kcal/mol. B3LYP-D3 calculation gave an energy difference of 3.5 kcal/mol between **TS5** and **TS5'**. This order of stability between **TS5** and **TS5'** was also observed by Goodman et al.⁹

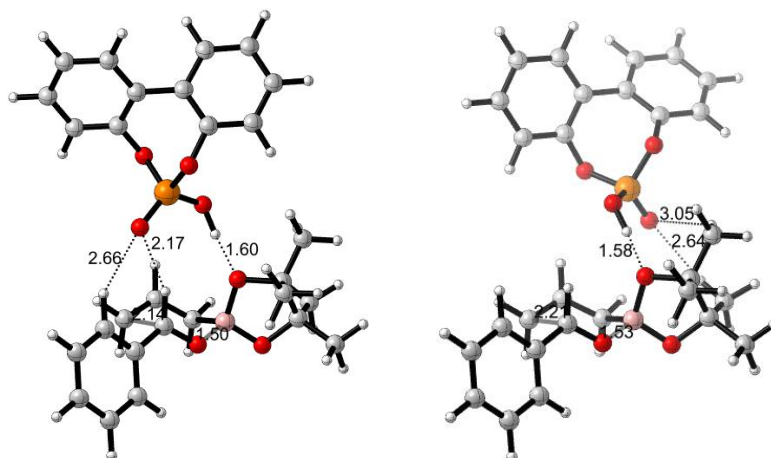
(a) Pathway i



TS4 0.0 (0.7)

TS4' 1.4 (2.7)

(b) Pathway ii



TS5 0.2 (0.0)

TS5' 3.2 (3.5)

Figure 5.6. Optimized transition state structures of (a) **TS4**, **TS4'** in pathway i (eq) and (b) **TS5**, **TS5'** in pathway ii (ax) at the B3LYP/6-31G* level of theory. Bond lengths are given in Å. Values next to each structure are energies relative to **TS4** in kcal/mol. Values in parentheses are energies relative to **TS5** calculated by B3LYP-D3.

In order to study the origin of the energy differences between the different transition state conformers, electrostatic potentials were computed. They are shown for the uncatalyzed reaction transition state **TS** in Figure 5.7. The formyl H, allyl Hs and phenyl Hs are more positive than the Hs on boronate methyls. This indicates that there can be stabilizing electrostatic attractions between the phosphoryl oxygen and those positive Hs. The stabilized interactions between electronegative parts of catalysts and the formyl H has been proposed by Corey before,¹⁶ as well as in Goodman's model. Here, **TS4** was more stable than **TS4'** and **TS5** was more stable than **TS5'**. The extra stabilization of **TS4** and **TS5** comparing to **TS4'** and **TS5'** came from the extra attractive P=O··H-C interactions, either with the aldehyde H in **TS5** or the phenyl and allyl Hs in **TS4**.

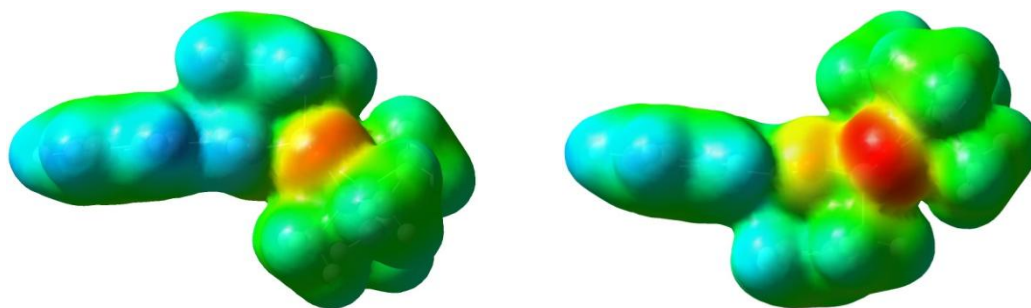


Figure 5.7. Top and bottom view of electrostatic potential of **TS** from Figure 5.4. Red: negative ESP; Blue: positive ESP; Green: neutral.

By comparing the most stable TSs in two pathways, **TS4** is calculated to be 0.2 kcal/mol more stable than **TS5** by B3LYP, but 0.7 kcal/mol less stable than **TS5** using B3LYP-D3. In the Goodman et al. work, when buta-1,3-diene-1,4- diol-phosphoric acid, which contains no aromatic rings was used as the model catalyst, the two competing pathways are differentiated by 2.2 kcal/mol. In our studies, the model catalyst (biphenol-derived phosphoric acid) resembles more the real catalysts in the experiment,

and the two different pathways are calculated to be similar in energy. This is likely due to the role of the additional aromatic rings in our model catalyst. The energy differences we calculate are quite small, suggesting that both of them may be involved in the reactions.

On the basis of these investigations, the “two-point binding models” of two different pathways shown in Figure 5.8 appear to operate for phosphoric acid catalyzed allylboration. The models consider two interactions between the catalyst and the substrates, which provide relative rigidity to the transition state. In what we will refer to as **A** (for axial), which is the same as Goodman’s model, the acidic H of the catalyst forms a hydrogen bond with the pseudo-axial oxygen of boronate. In **E** (for equatorial), the hydroxyl group of the catalyst H-bonds to the pseudo-equatorial oxygen of boronate. The second interaction comes from the electrostatic attractions between the phosphoryl oxygen and relatively positive Hs.

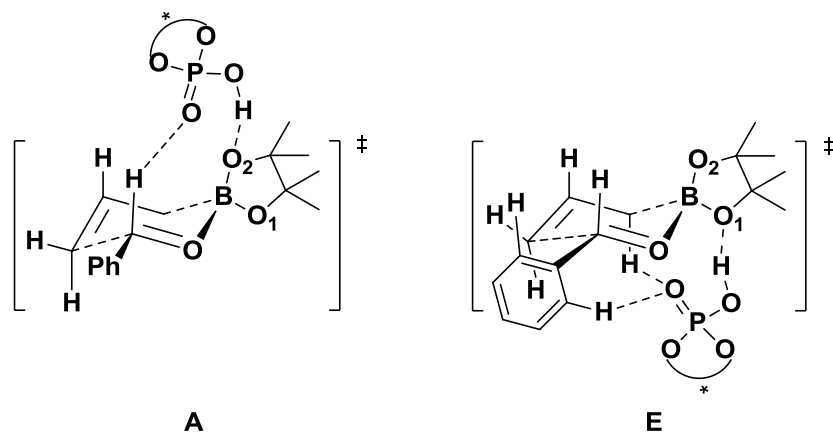


Figure 5.8. Models for the phosphoric acid-catalyzed allylboration reaction.

5.3.3 Activation barrier for uncatalyzed and catalyzed reactions

Having investigated the mechanism and the model for this chiral phosphoric acid catalyzed allylboration reaction, the issue of the reactivity in the present reaction was then addressed. The uncatalyzed allylboration reaction between allylboronate and benzaldehyde was studied first. The free energy profile is shown in Figure 5.9. A loose reactant complex **C1** is formed with 7.9 kcal/mol free energy higher than the separated reactants. The activation free energy of the uncatalyzed reaction relative to the separated reactants (**1+2**) was calculated to be high, 26.2 kcal/mol (Figure 5.9). This is consistent with the low reaction rates observed experimentally for the uncatalyzed allylboration reaction.¹⁷

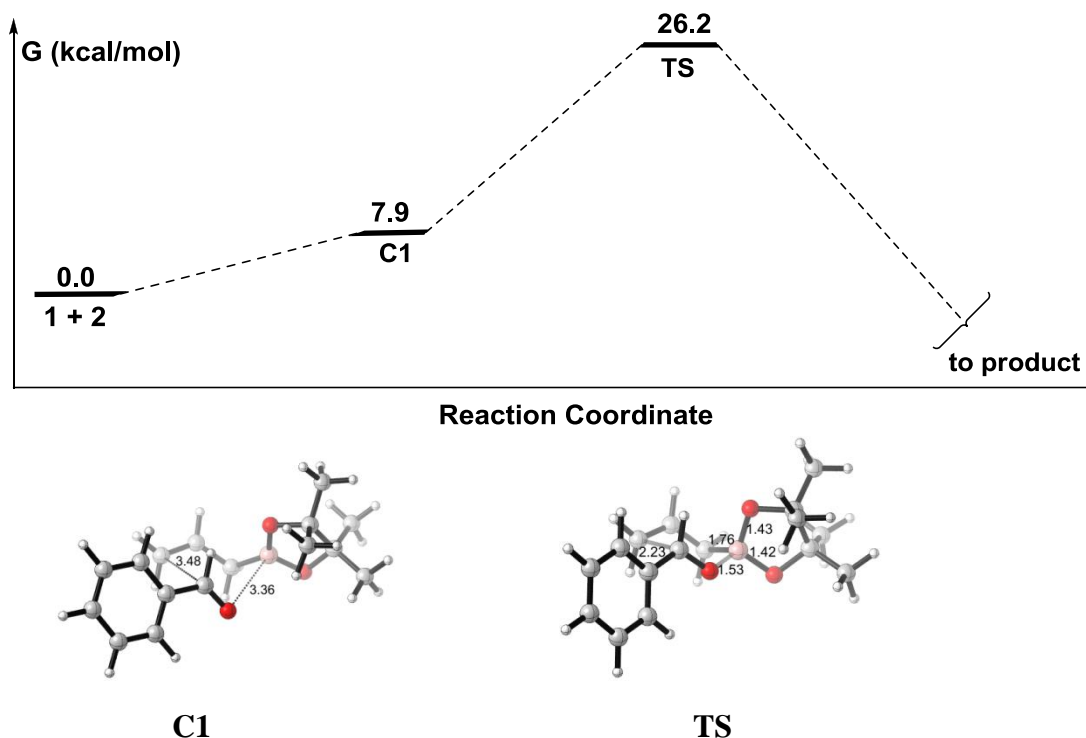


Figure 5.9. Reaction profile for the uncatalyzed allylboration reaction of **1** with **2** by B3LYP. Free energies relative the reactants in the gas phase. Optimized geometries of the complexes **C1** and transition state **TS** are shown below the reaction profile.

For the phosphoric acid-catalyzed reaction, in the **E** TS, the catalyst forms a hydrogen bond with the boronate pseudo-equatorial oxygen to afford complex **C2** with 0.6 kcal/mol free energy higher than the separated reactants, as shown in Figure 5.10. The binding of benzaldehyde on **C2** leads to the reactant complex **C3**. In transition state structure **TS4**, both the forming C-C and B-O bond distances (2.18 Å and 1.51 Å) are shorter than that in the uncatalyzed reaction **TS** (2.23 Å and 1.53 Å), which indicates the electrophilicity of boron is increased by catalyst activation. The calculated activation barrier of the catalyzed reaction relative to the separated reactants (**1+2+catalyst**) is 20.2 kcal/mol (Figure 5.10), 6 kcal/mol lower than the uncatalyzed reaction.

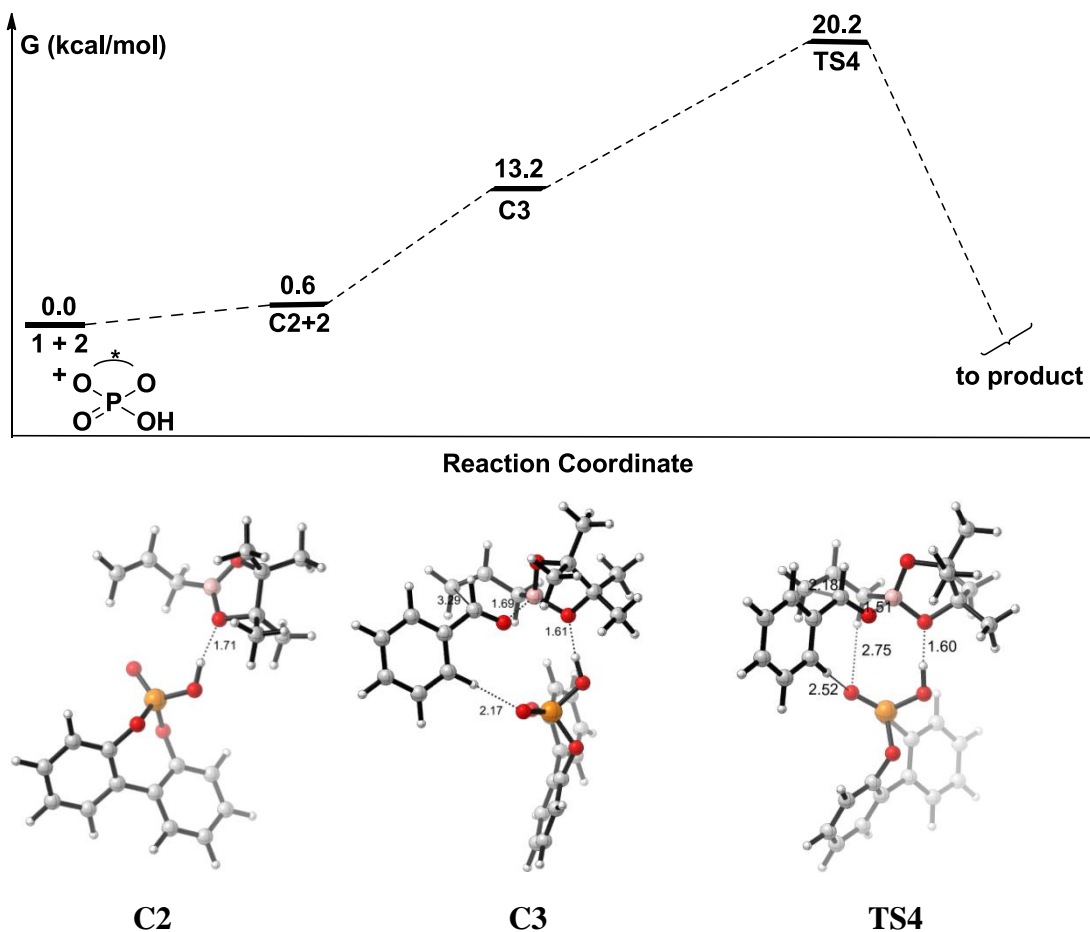


Figure 5.10. Reaction profiles for the allylboration reaction of **1** with **2** catalyzed by chiral phosphoric acid using **E** by B3LYP. Free energies relative the reactants in the gas phase. Optimized geometries of the complexes **C2**, **C3** and transition state **TS4** are shown below the reaction profile.

On the other hand, for the **A** TS, the catalyst forms a hydrogen bond with the boronate pseudo-axial oxygen to afford complex **C4**, as shown in Figure 5.11. The binding of benzaldehyde on **C4** leads to the reactant complex **C5** with 12.8 kcal/mol free energy higher than the separated reactants. In **TS5**, the electrophilicity of boron is also increased by catalyst activation represented by the shorter C-C and B-O bond distances (2.14 Å and 1.50 Å) than that in the uncatalyzed reaction **TS** (2.23 Å and 1.53 Å). And

the calculated activation barrier is 20.4 kcal/mol (Figure 5.11), 5.8 kcal/mol lower than the uncatalyzed reaction.

The two competing pathways give nearly identical energy profiles towards the catalyzed allylboration reactions, which again indicate the possibility that both two pathways are involved in the actual catalyzed reactions.

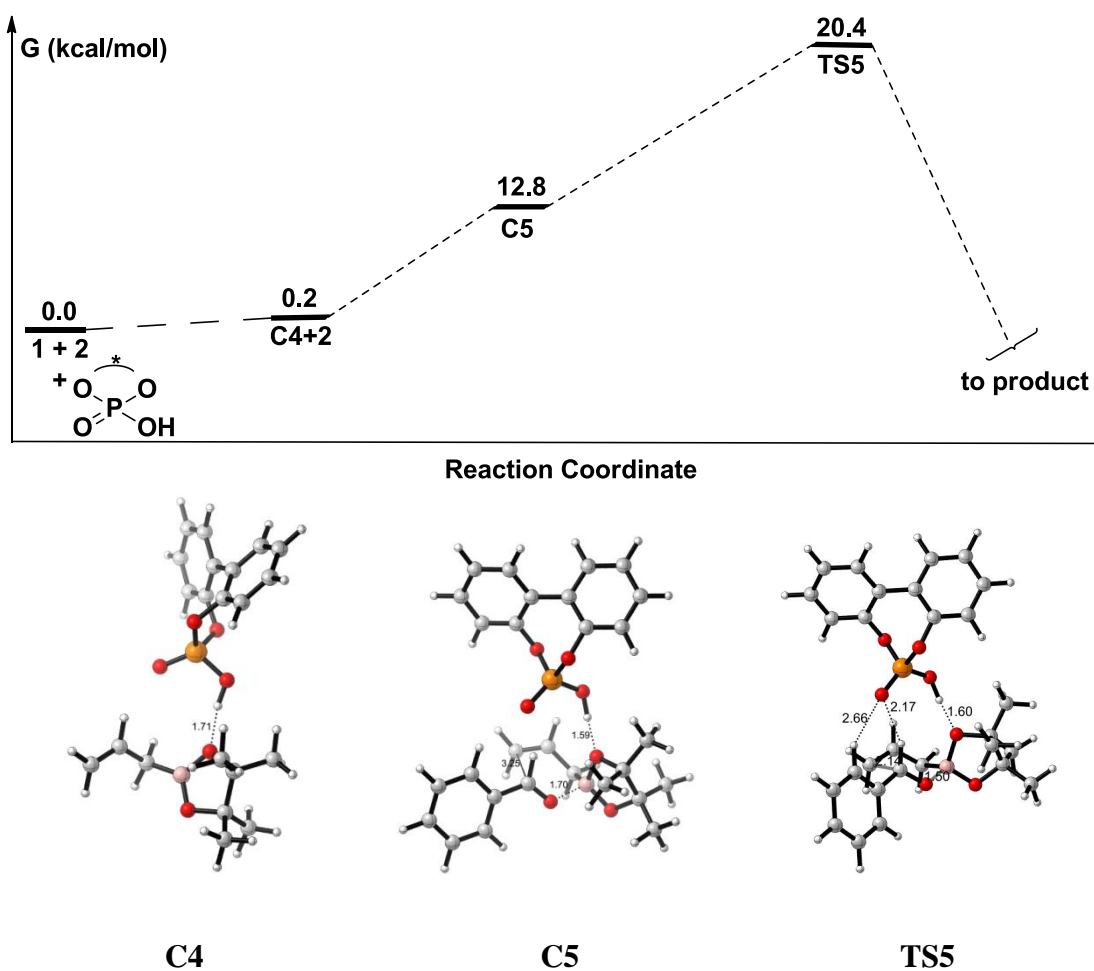


Figure 5.11. Reaction profiles for the allylboration reaction of **1** with **2** catalyzed by chiral phosphoric acid using **A** by B3LYP. Free energies relative the reactants in the gas phase. Optimized geometries of the complexes **C4**, **C5** and transition state **TS5** are shown below the reaction profile.

5.3.4 Origins of Enantioselectivity

The model studies described above indicated that both of the transition states in the two models, **A** and **E**, are likely to be involved in the reactions. To explore the origins of the enantioselectivity of the catalysis, the 3,3'-substituted BIPOL model for the binaphthol catalyst **PA1** was employed, and both transition states, **A** and **E**, were computed. Catalyst **PA1** bearing the 2,4,6-triisopropylphenyl group on the 3,3'-positions gave high enantioselectivity experimentally. The diastereomeric transition states for *re*-face (**r**) and *si*-face attack (**s**) involving BIPOL model of **PA1** were explored. The transition states involved were fully optimized, in contrast to Goodman's ONIOM calculations for these systems, **TSr1-E**, **TSs1-E** are located for **E** and **TSr1-A**, **TSs1-A** are located for **A**. These are shown in Figure 5.12.

In the equatorial coordination model **E**, the *re*-face attack **TSr1-E** is predicted to be more favored than the *si*-face attack **TSs1-E** by 2.0 kcal/mol. In the axial coordination model **A**, **TSr1-A** is more stable than **TSs1-A** by 6.1 kcal/mol using B3LYP calculations, which is consistent with Goodman's ONIOM calculations on these two TSs, which gives an energy difference of 6.7 kcal/mol.

In contrast to Goodman's ONIOM calculations that both *re* and *si* TSs are substantially energetically preferable in **A** over **E**, our fully optimized structure energies show that transition states resembling both models contribute to selectivity. That is, using the B3LYP-D3 energetics, the relative rates of reaction via **TSr1-A**, **TSr1-E**, and **TSs1-E** will be 1:0.05:0.001. Use of **A** only predicts far too high selectivity. The energy

difference between the most stable *re*-face (**r**) attack transition state **TSr1-A** and the most stable *si*-face (**s**) attack transition state **TSs1-E** is 2.6 kcal/mol by B3LYP, which is in close agreement with the 93% ee observed experimentally. Solvation energy calculations using PCM model with toluene as the solvent does not change the energy difference very much, which gives a number of 3.1 kcal/mol.

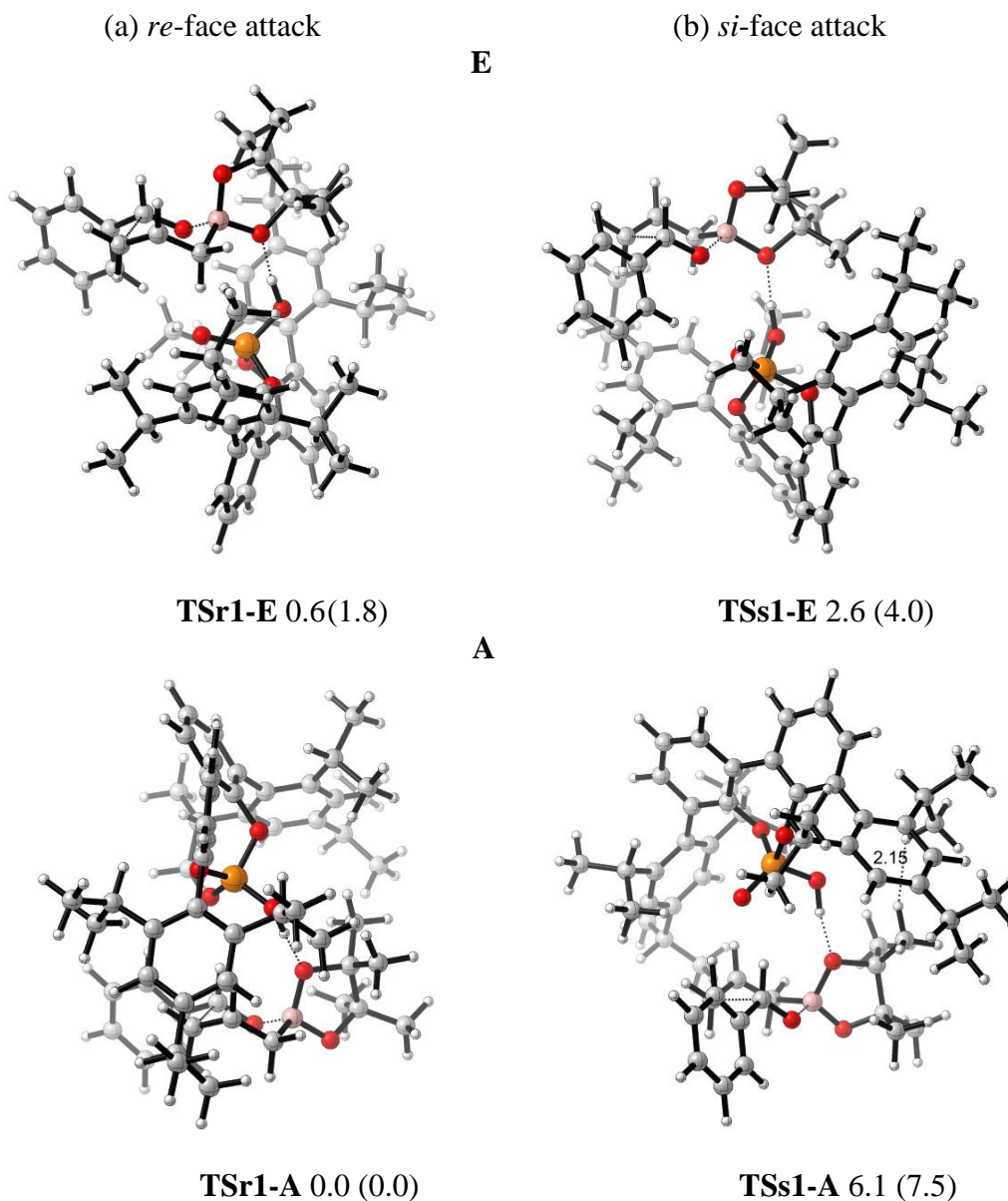


Figure 5.12. Optimized structures of **TSr1-E** and **TSs1-E** for **E**, **TSr1-A** and **TSs1-A** for **A**. Values next to each structure are energies relative to **TSr1-A** in kcal/mol. Values enclosed in parentheses are energies relative to **TSr1-A** calculated by B3LYP-D3.

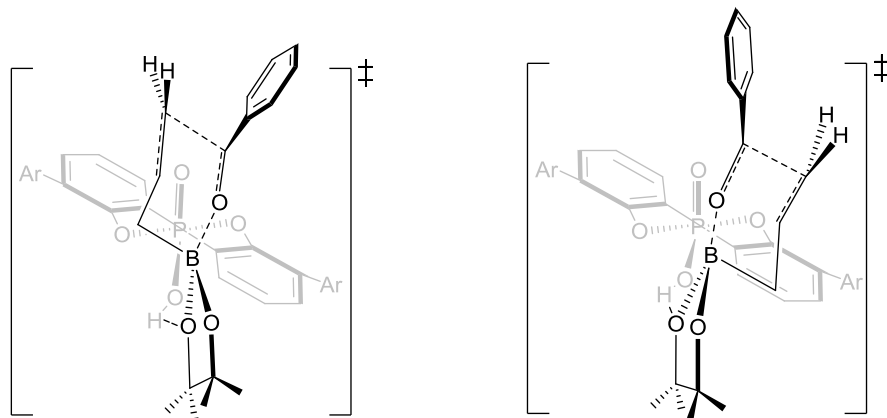
Based on these calculations, we compare the two competing models for each enantiomeric TS (*re* or *si*), respectively. In Goodman's paper, the large preference for **A** comes from both steric and electronic factors. In the case of *re*-TSs, our calculations, in agreement with Goodman's results, show **A (TSr1-A)** is more stable than **E (TSr1-E)**. Inspection of the two diastereomeric TSs show they are both free of steric problems by inspecting all the H-H distances; all H-H distances are 2.4 Å or more. The stabilities between two TSs is then perhaps because formyl H-bond strength inside **A (TSr1-A)** is stronger than the electrostatic interactions between phosphoryl oxygen and relative positive Hs in **E (TSr1-E)**.

Our calculations show that **A (TSs1-A)** is much less favorable than **E (TSs1-E)** for *si*-TSs. In our fully optimized TS structures **TSs1-A** and **TSs1-E**, both of them have an almost linear H-bond arrangement. However, **A (TSs1-A)** has a longer H-bond distance (1.65 Å) and corresponding weaker H-bond strength than that in **E (TSs1-E)** (1.59 Å); this is opposite from Goodman's ONIOM calculated structures. We find a steric difference between the two models. Inspection of **A (TSs1-A)** shows that the pinacol group is orientated toward the bulky pocket of the catalyst, and there is one significant steric repulsion between an isopropyl H on the catalyst and a methyl H on the boronate; separated by only 2.15 Å; such steric repulsions are not found in **E (TSs1-E)**. As a result, both electronic and steric factors make **A (TSs1-A)** less favorable than **E (TSs1-E)** in our calculated structures for *si*-TSs.

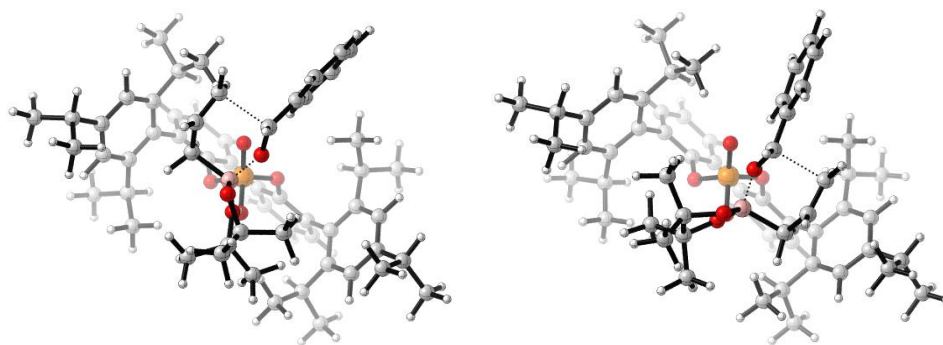
After comparing the two competing models, it is then necessary to investigate the origins of different stabilities between *re* and *si* TSs in each model, respectively. In **A**, the stabilities between **TSr1-A** and **TSs1-A** are due to steric factors. One significant steric repulsion between isopropyl H on the catalyst and methyl H on the boronate, separated by only 2.15 Å, was found for **TSs1-A**; by contrast **TSr1-A** is free of steric congestion. These steric factors are believed to control the stabilities of two diastereomeric TSs in **A** in Goodman's studies as well.

In **E**, however, as mentioned above, there are no obvious steric differences in the two transition states **TSr1-E** and **TSs1-E**. To gain insights into the origins of the energy difference between **TSr1-E** and **TSs1-E**, the distortion energy (ΔE_d) and interaction energy (ΔE_i) of the transition states were performed. This method has been used previously to understand 1,3-dipolar and Diels-Alder cycloadditions.¹⁸ **TSr1-E** and **TSs1-E** are divided into two parts: catalyst-boronate complex **1A** and the benzaldehyde **1B** (Figure 5.13b) with the geometries fixed at the transition state geometries. The calculated distortion energy ΔE_d of **1B** in **TSr1-E** (+12.2 kcal/mol) is almost the same as that in **TSs1-E** (+12.3 kcal/mol). There is also no interaction energy ΔE_i difference between **TSr1-E** (-41.3 kcal/mol) and **TSs1-E** (-41.2 kcal/mol) which means all of the stabilizing and destabilizing interactions between **1A** and **1B** in the two TSs are similar. The preference for *re*-facial selectivity is therefore the result of the larger distortion of catalyst-boronate complex **1A** in **TSs1-E**. **1A** is more heavily distorted in **TSs1-E** (+33.9 kcal/mol) than in **TSr1-E** (+32.1 kcal/mol) by 1.8 kcal/mol.

The origins of the differences in distortion energies of **1A** in the two TSs can be visualized from the **1A** geometries, as shown in Figure 5.13. In Figure 5.13d, which shows the **1A** structure in **TSs1-E**, the dioxaborolane ring is on the left, and the methyl groups on the dioxaborolane ring and isopropyl groups of catalysts are close to each other (green atoms in Figure 5.13d). In order to minimize such steric repulsions, the 2,4,6-triisopropylphenyl substituent is rotated around the bond to the BIPOL phenyl core with a dihedral angle of 80° . This is an 8° rotation away from the dihedral angle in the optimized catalyst (72°). Due to the distortion of the catalyst, the green atoms (Figure 5.13d) are all far away, resulting in no steric repulsions. In other words, the catalyst undergoes conformational changes to avoid unfavorable steric interactions in **TSs1-E**. Figure 5.13c shows the **1A** structure in **TSr1-E**. Here, the dioxaborolane ring is far from the catalyst, and the dihedral angle between 2,4,6-triisopropylphenyl substituent and the BIPOL core is 72° , the same as the dihedral angle of 72° in the optimized catalyst. The asymmetric induction can be rationalized by differences in distortion energies originating from avoiding the steric interactions between the substrates and the bulky 3,3'-substituents on the catalysts.



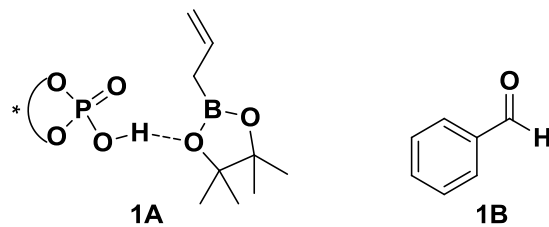
(a)



TSr1-E

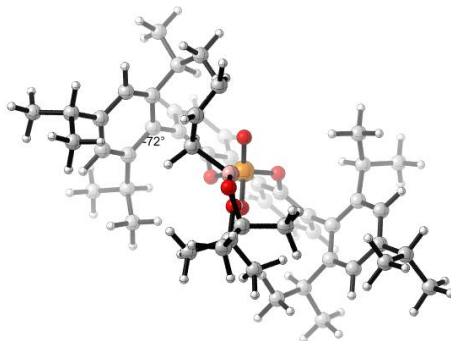
TSs1-E

(b)

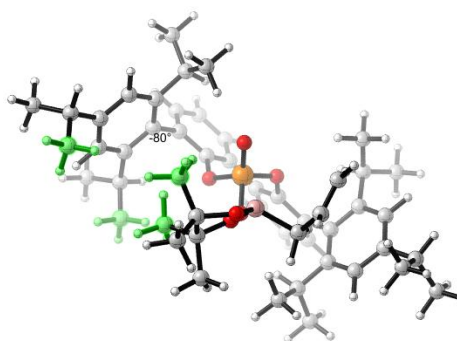


1A

1B



(c)



(d)

Figure 5.13. (a) Side view of **TSr1-E** and **TSs1-E**. (b) Structures of **1A** and **1B**. (c) 3D structures of **1A** in **TSr1-E**. (d) 3D structures of **1A** in **TSs1-E**.

After investigating the allylboration reaction, we then reinvestigated the propargylations. The propargylation proceeds via a six-membered cyclic transition state similar to that for allylborations. Once again, the catalyst could activate the reaction by forming a hydrogen bond with either of the boronate oxygens. The transition state structures of propargylation involving the phosphoric acid catalyst **PA1** using both **E** and **A** were studied. As before, diastereomeric transition states **TSr1'-E** and **TSS1'-E** were located for **E**, and **TSr1'-A** and **TSS1'-A** were located for **A** (Figure 5.14).

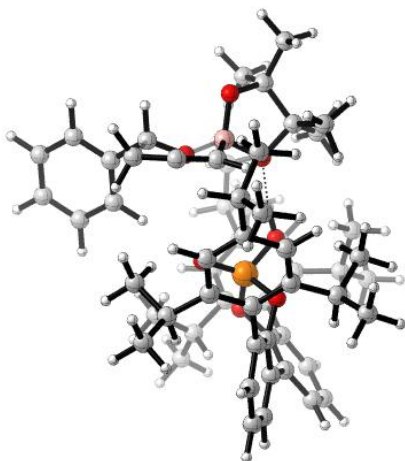
As in the allylboration analysis, for *re*-face (**r**) attack, **A** (**TSr1'-A**) is more stable than **E** (**TSr1'-E**) by 2.7 (or 3.5) kcal/mol. For *si*-face (**s**) attack, **A** (**TSS1'-A**) is less stable than **E** (**TSS1'-E**) by 1.3 (or 1.2) kcal/mol. The energy difference between the most stable *re*-face (**r**) attack transition state **TSr1'-A** and the most stable *si*-face (**s**) attack transition state **TSS1'-E** is 4.0 (or 5.1) kcal/mol, overestimating the stereoselectivities as compared to the 74% ee observed experimentally.

Our studies on propargylations still showed that for *re*-TSs, **A** is more favorable; while **E** is more favorable for *si*-TSs. The **A** and **E** transition states leading to *re* attack are both lower in energy than **E** transition state that leads to *si* attack.

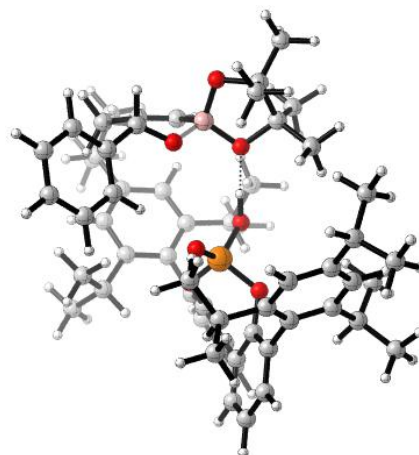
(a) *re*-face attack

(b) *si*-face attack

E

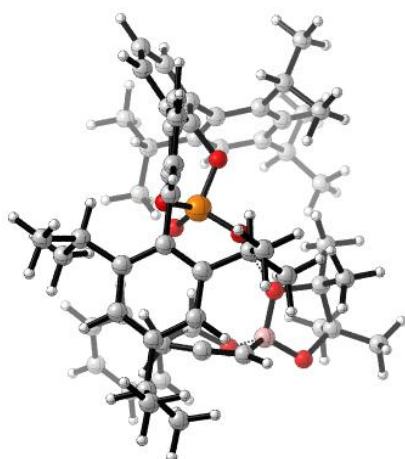


TSr1'-E 2.7 (3.5)

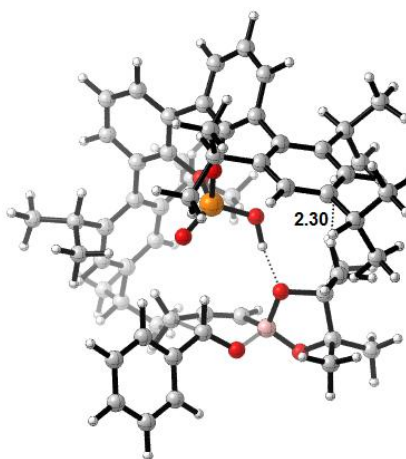


TSs1'-E 4.0 (5.1)

A



TSr1'-A 0.0 (0.0)



TSs1'-A 5.3 (6.3)

Figure 5.14. Optimized structures of **TSr1'-E** and **TSs1'-E** for **E**, **TSr1'-A** and **TSs1'-A** for **A**. Values next to each structure are energies relative to **TSr1'-A** in kcal/mol. Values enclosed in parentheses are energies relative to **TSr1'-A** calculated by B3LYP-D3.

In **E**, the calculated distortion energy ΔE_d of benzaldehyde in **TSr1'-E** (+17.4 kcal/mol) is almost the same as that in **TSs1'-E** (+17.5 kcal/mol), so is the interaction energy ΔE_i for the two transition states. The preference for *re*-facial selectivity still comes from the larger distortion of catalyst-boronate complex in **TSs1'-E**. The catalyst-boronate complex is calculated to be more heavily distorted in **TSs1'-E** (+45.9 kcal/mol) than in **TSr1'-E** (+44.7 kcal/mol) by 1.2 kcal/mol.

The origin of the differences in distortion energies of catalyst-boronate complex in the two TSs is similar to that in the allylboration reaction. In Figure 5.15b which shows the complex structures in **TSs1'-E**, in order to minimize the steric repulsions between the methyl groups on the dioxaborolane ring and isopropyl groups of catalysts (green atoms in Figure 5.15b), the 2,4,6-triisopropylphenyl substituent is rotated around the bond to the BIPOL phenyl core with a dihedral angle of 78° . In Figure 5.15a which shows the catalyst-boronate complex structure in **TSr1'-E**, the dihedral angle between 2,4,6-triisopropylphenyl substituent and the BIPOL core is 74° . The 4° dihedral angle differences of the two complexes accounts for their different distortion energies.

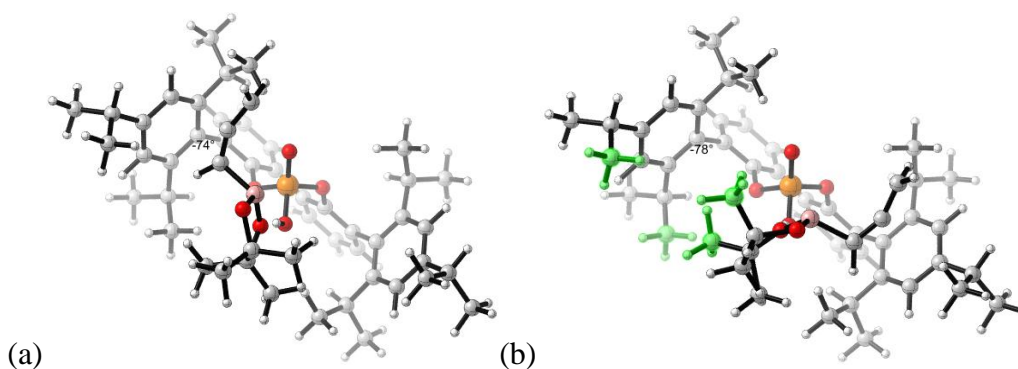


Figure 5.15. (a) 3D structure of **TSr1'-E** without the benzaldehyde. (b) 3D structure of **TSs1'-E** without the benzaldehyde.

5.4 Conclusion

Theoretical calculations have been carried out for the chiral phosphoric acid-catalyzed enantioselective allylboration and propargylation reactions. Transition states with either boronate oxygen hydrogen-bonded to the phosphoric acid were studied. The catalyst is able to activate the boronate by forming a hydrogen bond either with the pseudo-equatorial oxygen (**E**) or the pseudo-axial oxygen (**A**) of the boronate; the phosphoryl oxygen interacts with relatively positive Hs of the substrate through electrostatic attractions, which provides further stabilization of the TS, and a two-point orientation of the catalyst. Pathway **A** is investigated in detail in Goodman's model⁹, and our studies focus more on pathway **E** in this paper.

For *re*-face attack, both equatorial and axial coordination gives TSs that are free of steric repulsions, with **A** more favorable than **E**. The relative stability of **A** is due to the formyl H-bond strength in **A**. For *si*-face attack, to give the minor enantiomer, our calculations showed that **A** is less favorable than **E**. Steric factors make the more crowded **A** less stable than the less crowded **E**.

Calculations show that the enantioselectivity observed experimentally originates from larger distortions of the catalyst in the minor enantiomeric TS, which is the result of the avoidance of the repulsive interactions between the bulky 3,3'-substituents in the catalyst and the substrates. The pinacol boronate methyls have an important role, and these groups could be altered to influence stereoselectivities. These investigations might help direct future enantioselective catalysis development for allylboration and propargylation reactions.

5.5 References

1. For reviews, see: (a) Denmark, S. E.; Almstead, N. G. In *Modern Carbonyl Chemistry*; Otera, J., Ed.; Wiley-VCH: Weinheim, 2000; Chapter 10, pp 299-402. (b) Chemler, S. R.; Roush, W. R. In *Modern Carbonyl Chemistry*; Otera, J., Ed.; Wiley-VCH: Weinheim, 2000; Chapter 11, 403-490. (c) Yamamoto, Y.; Asao, N. *Chem. Rev.* **1993**, *93*, 2207–2293. (d) Denmark, S. E.; Fu, J. *Chem. Rev.* **2003**, *103*, 2763–2793. (e) Lachance, H.; Hall, D. G. *Org. React.* **2008**, *73*, 1. (f) Roush, W. R. In *Comprehensive Organic Synthesis*; Trost, B. M., Ed.; Pergamon Press: Oxford, U.K., 1991; Vol. 2, p 1. (g) Yus, M.; González-Gómez, J. C.; Foubelo, F. *Chem. Rev.* **2011**, *111*, 7774-7854.
2. (a) Roush, W. R.; Walts, A. E.; Hoong, L. K. *J. Am. Chem. Soc.* **1985**, *107*, 8186–8190. (b) Roush, W. R.; Palkowitz, A. D.; Ando, K. *J. Am. Chem. Soc.* **1990**, *112*, 6348-6359. (c) Brown, H. C.; Bhat, K. S.; Randad, R. S. *J. Org. Chem.* **1989**, *54*, 1570-1576. (d) Brown, H. C.; Randad, R. S.; Bhat, K. S.; Zaidlewicz, M.; Racherla, U. S. *J. Am. Chem. Soc.* **1990**, *112*, 2389-2392. (e) Corey, E. J.; Yu, C.-M.; Lee, D.-H. *J. Am. Chem. Soc.* **1990**, *112*, 878–879. (f) Gonzalez, A. Z.; Roman, I. G.; Alicea, E.; Canales, E.; Soderquist, J. A. *J. Am. Chem. Soc.* **2009**, *131*, 1269-1273. (g) Burgos, C. H.; Canales, E.; Matos, K.; Soderquist, J. A. *J. Am. Chem. Soc.* **2005**, *127*, 8044–8049. (h) Wu, T. R.; Shen, L.; Chong, J. M. *Org. Lett.* **2004**, *6*, 2701–2704. (i) Lachance, H.; Lu, X.; Gravel, M.; Hall, D. G. *J. Am. Chem. Soc.* **2003**, *125*, 10160–10161. (j) Chen, M.; Handa, M.; Roush, W. R. *J. Am. Chem. Soc.* **2009**, *131*, 14602-14603. (k) Althaus, M.; Mahmood, A.; Suarez, J. R.; Thomas, S. P.; Aggarwal, V. K. *J. Am. Chem. Soc.* **2010**, *132*, 4025-4028.
3. (a) Kennedy, J. W. J.; Hall, D. G. *J. Am. Chem. Soc.* **2002**, *124*, 11586-11587. (b) Lachance, H.; Xu, M.; Gravel, M.; Hall, D. G. *J. Am. Chem. Soc.* **2003**, *125*, 10160-10161. (c) Hall, D. G. *Synlett* **2007**, 1644–1655. (d) Kennedy, J. W. J.; Hall, D. G. *J. Org. Chem.* **2004**, *69*, 4412–4428. (e) Rauniyar, V.; Hall, D. G. *J. Am. Chem. Soc.* **2004**, *126*, 4518–4519. (f) Carosi, L.; Lachance, H.; Hall, D. G. *Tetrahedron* **2005**, *46*, 8981–8985. (g) Rauniyar, V.; Zhai, H.; Hall, D. G. *J. Am. Chem. Soc.* **2008**, *130*, 8481-8490. (h) Rauniyar, V.; Hall, D. G. *J. Org. Chem.* **2009**, *74*, 4236-4241. (i) Ishiyama, T.; Ahiko, T.-a.; Miyaura, N. *J. Am. Chem. Soc.* **2002**, *124*, 12414-12415. (j) Wada, R.; Oisaki, K.; Kanai, M.; Shibasaki, M. *J. Am. Chem. Soc.* **2004**, *126*, 8910 – 8911.
4. (a) Yu, S. H.; Ferguson, M. J.; McDonald, R.; Hall, D. G. *J. Am. Chem. Soc.* **2005**, *127*, 12808–12809. (b) Rauniyar, V.; Hall, D. G. *Angew. Chem., Int. Ed.* **2006**, *45*, 2426–2428. (c) Elford, T. G.; Arimura, Y.; Yu, S. H.; Hall, D. G. *J. Org. Chem.* **2007**, *72*, 1276–1284. (d) Rauniyar, V.; Zhai, H.; Hall, D. G. *J. Am. Chem. Soc.* **2008**, *130*, 8481–8490.
5. For reviews, see: (a) Akiyama, T. *Chem. Rev.* **2007**, *107*, 5744-5758. (b) Terada, M. *Chem. Commun.* **2008**, 4097-4112. (c) Brunel, J. M. *Chem. Rev.* **2005**, *105*,

- 857-897. (d) Chen, Y.; Yekta, S.; Yudin, A. K. *Chem. Rev.* **2003**, *103*, 3155-3211. (e) Akiyama, T.; Itoh, J.; Fuchibe, K. *Adv. Synth. Catal.* **2006**, *348*, 999-1010. (f) Connon, S. J. *Angew. Chem., Int. Ed.* **2006**, *45*, 3909-3912. (g) Rueping, M.; Kuenkel A.; Atodiresei, I. *Chem. Soc. Rev.* **2011**, *40*, 4539-4549. (h) Zamfir, A.; Schenker, S.; Freund, M.; Tsogoeva, S. B. *Org. Biomol. Chem.* **2010**, *8*, 5262-5276.
6. For theoretical studies on the chiral phosphoric acid catalysis, see: (a) Yamanaka, M.; Itoh, J.; Fuchibe, K.; Akiyama, T. *J. Am. Chem. Soc.* **2007**, *129*, 6756-6764. (b) Simoń, L.; Goodman, J. M. *J. Am. Chem. Soc.* **2008**, *130*, 8741-8747. (c) Simoń, L.; Goodman, J. M. *J. Am. Chem. Soc.* **2009**, *131*, 4070-4077. (d) Simoń, L.; Goodman, J. M. *J. Org. Chem.* **2010**, *75*, 589-597. (e) Simoń, L.; Goodman, J. M. *J. Org. Chem.*, **2011**, *76*, 1775-1788. (f) Marcelli, T.; Hammar, P.; Himo, F. *Chem. Eur. J.* **2008**, *14*, 8562-8571. (g) Akiyama, T.; Morita, H.; Bachu, P.; Mori, K.; Yamanaka, M.; Hirata, T. *Tetrahedron.* **2009**, *65*, 4950-4956. (h) Shi, F.-Q.; Song, B.-A. *Org. Biomol. Chem.* **2009**, *7*, 1292-1298. (i) Yamanaka, M.; Hirata, T. *J. Org. Chem.* **2009**, *74*, 3266-3271. (j) Gridnev, I. D.; Kouchi, M.; Sorimachi, K.; Terada, M. *Tetrahedron Lett.* **2007**, *48*, 497-500.
7. Jain, P.; Antilla, J. C. *J. Am. Chem. Soc.* **2010**, *132*, 11884-11886.
8. Jain, P.; Wang, H.; Houk, K. N.; Antilla, J. C. *Angew. Chem., Int. Ed.* **2012**, *124*, 1420-1423.
9. Grayson, M. N.; Pellegrinet, S. C.; Goodman, J. M. *J. Am. Chem. Soc.* **2012**, *134*, 2716-2722.
10. (a) For dispersion correction, see: (a) Grimme, S. *J. Comput. Chem.* **2006**, *27*, 1787-1799. (b) Grimme, S.; Antony, J.; Ehrlich, S.; Krieg, H. *J. Chem. Phys.* **2010**, *132*, 154104. For application of dispersion corrected DFT in computational chemistry, see: (c) McMullin, C. L.; Jover, J.; Harvey, J. N.; Fey, N. *Dalton Trans.* **2010**, *39*, 10833-10836. (d) Antoline, J. E.; Krenske, E. H.; Lohse, A. G.; Houk, K. N.; Hsung, R. P. *J. Am. Chem. Soc.* **2011**, *133*, 14443-14451.
11. (a) Li, Y.; Houk, K. N. *J. Am. Chem. Soc.* **1989**, *111*, 1236-1240. (b) Gung, B. W.; Xue, X.; Roush, W. R. *J. Am. Chem. Soc.* **2002**, *124*, 10692-10697.
12. Frisch, M. J. et al. *Gaussian 09*, revision B.01; Gaussian, Inc.: Wallingford, CT, 2010.
13. (a) Omoto, K.; Fujimoto, H. *J. Org. Chem.* **1998**, *63*, 8331-8336. (b) Brown, H. C.; Racherla, U. S.; Pellechia, P. J. *J. Org. Chem.* **1990**, *55*, 1868-1874.
14. Rauniyar, V.; Hall, D. G. *J. Am. Chem. Soc.* **2004**, *126*, 4518-4519.
15. Sakata, K.; Fujimoto, H. *J. Am. Chem. Soc.* **2008**, *130*, 12519-12526.

16. (a) Corey, E. J.; Rohde, J. J.; Fischer, A.; Azimioara, M. D. *Tetrahedron Lett.* **1997**, *38*, 33-36. (b) Corey, E. J.; Rohde, J. J. *Tetrahedron Lett.* **1997**, *38*, 37-40. (c) Corey, E. J.; David B. S.; Thomas, W. L. *Tetrahedron Lett.* **1997**, *38*, 1699-1702.
17. Ishiyama, T.; Ahiko, T.; Miyaura, N. *J. Am. Chem. Soc.* **2002**, *124*, 12414–12415.
18. (a) Ess, D. H.; Houk, K. N. *J. Am. Chem. Soc.* **2008**, *130*, 10187-10198. (b) Ess, D. H.; Houk, K. N. *J. Am. Chem. Soc.* **2007**, *129*, 10646-10647. (c) Ess, D. H.; Jones, G. O.; Houk, K. N. *Org. Lett.* **2008**, *10*, 1633-1636. (d) Garcí'a, J. I.; Martí'nez-Merino, V.; Mayoral, J. A.; Salvatella, L. *J. Am. Chem. Soc.* **1998**, *120*, 2415-2420. (e) Sbai, A.; Branchadell, V.; Ortuño, R. M.; Oliva, A. *J. Org. Chem.* **1997**, *62*, 3049-3054.